---

Multi-species gas detection based on an external-cavity quantum cascade laser spectrometer in the mid-infrared fingerprint region

---

Dissertation zur Erlangung des
naturwissenschaftlichen Doktorgrades
der Julius-Maximilians-Universität Würzburg

vorgelegt von

Robert Heinrich
aus Leipzig

Würzburg 2022

Eingereicht am: 07.06.2021
bei der Fakultät für Physik und Astronomie

1. Gutachter: Prof. Dr. Sven Höfling

2. Gutachter: Prof. Dr. Bert Hecht

der Dissertation

Vorsitzende: Prof. Dr. Johanna Erdmenger

1. Prüfer: Prof. Dr. Sven Höfling

2. Prüfer: Prof. Dr. Bert Hecht

3. Prüfer: Prof. Dr. Volker Engel

im Promotionskolloquium

Tag des Promotionskolloquiums: 11.03.2022

Doktorurkunde ausgehändigt am: ....

Abstract

Laser spectroscopic gas sensing has been applied for decades for several applications as atmospheric monitoring, industrial combustion gas analysis or fundamental research. The availability of new laser sources in the mid-infrared opens the spectral fingerprint range to the technology where multiple molecules possess their fundamental ro-vibrational absorption features that allow very sensitive detection and accurate discrimination of the species. The increasing maturity of quantum cascade lasers that cover this highly interesting spectral range motivated this research to gain fundamental knowledge about the spectra of hydrocarbon gases in pure composition and in complex mixtures as they occur in the petro-chemical industry. The long-term target of developing accurate and fast hydrocarbon gas analyzers, capable of real-time operation while enabling feedback-loops, would lead to a paradigm change in this industry.

This thesis aims to contribute to a higher accuracy and more comprehensive understanding of the sensing of hydrocarbon gas mixtures. This includes the acquisition of yet unavailable high resolution and high accuracy reference spectra of the respective gases, the investigation of their spectral behavior in mixtures due to collisional broadening of their transitions and the verification of the feasibility to quantitatively discriminate the spectra when several overlapping species are simultaneously measured in gas mixtures. To achieve this knowledge a new laboratory environment was planned and built up to allow for the supply of the individual gases and their arbitrary mixing. The main element was the development of a broadly tunable external-cavity quantum cascade laser based spectrometer to record the required spectra. This also included the development of a new measurement method to obtain highly resolved and nearly gap-less spectral coverage as well as a sophisticated signal post-processing that was crucial to achieve the high accuracy of the measurements. The spectroscopic setup was used for a thorough investigation of the spectra of the first seven alkanes as of their mixtures. Measurements were realized that achieved a spectral resolution of 0.001 cm^{-1} in the range of 6-11 μm while ensuring an accuracy of $\pm$0.001 cm^{-1} of the spectra and attaining a transmission sensitivity of $2.5 \cdot 10^{-4}$ for long-time averaging of the acquired spectra.

These spectral measurements accomplish a quality that compares to state-of-the art spectral databases and revealed so far undocumented details of several of the investigated gases that have not been measured with this high resolution before at the chosen measurement conditions. The results demonstrate the first laser spectroscopic discrimination of a seven component gas mixture with absolute accuracies below 0.5 vol.% in the mid-infrared provided that a sufficiently broad spectral range is covered in the measurements. Remaining challenges for obtaining improved spectral models of the gases and limitations of the measurement accuracy and technology are discussed.

Zusammenfassung

Laserspektroskopie ist eine seit Jahrezehnten verbreitete Methodik zur Gasmessung. Zu den Anwendungen zählen Atmosphärenuntersuchungen, die Analyse von industriellen Verbrennungsgasen oder Grundlagenforschung der Gasspektren. Die Verfügbarkeit neuer Laserquellen im mittleren Infrarotbereich eröffnet den sogenannten spektralen "Fingerprint-Bereich", in welchem eine Vielzahl von Molekülen ihre spezifischen Rotations-Vibrations-Grundschwingungen haben, und damit sehr genaue Konzentrationsbestimmung und exakte Unterscheidung der Gase ermöglicht. Die zunehmende Reife von Quantenkaskadenlasern motivierte diese Forschungsarbeit, um Grundlagenwissen über pure Kohlenwasserstoffspektren und deren Mischungen, wie sie beispielsweise in der petrochemischen Industrie auftreten, zu erlangen. Das langfristige Ziel der Entwicklung eines hochgenauen und schnellen Analysators für Kohlenwasserstoffgemische, welcher Echtzeit-Messungen und damit direkte Rückkopplungsschleifen ermöglicht, würde zu einem Paradigmenwechsel in der Prozesskontrolle vieler Industriebereiche führen.

Diese Doktorarbeit leistet einen Beitrag für ein umfassenderes Verständnis und höhere Genauigkeit der Messung von Kohlenwasserstoffgemischen. Dies beinhaltet die Aufnahme bisher nicht verfügbarer hochaufgelöster und hochgenauer Referenzspektren der untersuchten Gase, die Untersuchung ihres spektralen Verhaltens bei Stoßverbreiterung in Mischungen und der quantitativen Unterscheidbarkeit, wenn Moleküle mit überlappenden Spektren gleichzeitig gemessen werden. Um dieses Wissen zu erlangen, wurde ein neuer Laboraufbau zur Untersuchung einzelner Gase sowie deren Gemische geplant und aufgebaut. Die Hauptkomponente bildet eine weit abstimmbares Externe-Kavität-Quantenkaskadenlaser-Spektrometer. Weitere Teile der Entwicklung waren zudem eine neue Messmethodik, um hochaufgelöste und im untersuchten Spektralbereich nahezu lückenlose Spektren zu erhalten, sowie eine umfangreiche Nachverarbeitung der Messdaten, welche essentiell war, um die hohe Genauigkeit der Messungen zu ermöglichen.

Der Spektrometeraufbau wurde zur Untersuchung der Spektren der ersten sieben Alkane und ihrer Mischungen verwendet. Die Messungen erreichen eine spektrale Auflösung von $0.001\ \mathrm{cm}^{-1}$ im Spektralbereich von 6-11 μm und garantieren gleichzeitig eine Genauigkeit von $\pm 0.001\ \mathrm{cm}^{-1}$. Eine Sensitivität von $2.5 \cdot 10^{-4}$ konnte durch das Mitteln mehrerer Messungen erreicht werden.

Die Qualität der Spektren ist damit vergleichbar zu aktuellen Spektren-Datenbanken und zeigt zudem bisher undokumentierte Details in mehreren Spektren der gemessenen Gase auf, welche unter den gewählten Messbedingungen bisher nicht so hochaufgelöst gemessen wurden. Die Ergebnisse demonstrieren die erste laserspektrokopische Unterscheidung eines Siebenkomponentengemisches von Kohlenwasserstoffen im mittleren Infrarotbereich mit einer absoluten Konzentrationsgenauigkeit von unter 0.5 vol.% je Komponenten. Weitere Herausforderungen zur Verbesserung spektraler Modelle der Gase sowie die Grenzen der Messgenauigkeit und der verwendeten Technologie werden diskutiert.

Acknowledgements

I want to thank the numerous people that contributed to this work. Without their help and support this thesis would not have been completed as presented here. Specifically I would like to express my gratitude to,

Contents

List of Figures

List of Tables

List of Abbreviations

AR	Anti-reflection
AWG	Arrayed Waveguide Grating
BNC	Bayonet Neil-Concelman
CB	Conduction band
DAQ	Data acquisition
DFB	Distributed feedback
EC	External-cavity
EC-QCL	External-cavity quantum cascade laser
EOS	Equation of state
FC-PC	Fiber optic-physical contact
FFT	Fast Fourier Transform
FP	Fabry Pérot
FSR	Free spectral range
FTIR	Fourier transform infrared
FWHM	Full width half maximum
GC	Gas Chromatograph
GEISA	Gestion et Étude des Information Spectroscopiques Atmosphériques
GUI	Graphical user interface
HITEMP	High temperature molecular spectroscopic database
HITRAN	High-resolution transmission molecular absorption database
HR	High-reflection
HWHM	Half width half maximum
ICL	Interband Cascade Laser

IR	Infrared
LO	Longitudinal-optical
MCT	Mercury cadmium telluride
MDA	Minimum detectable absorption
MFC	Mass flow controller
MIR	Mid-infrared
MOEMS	Micro-Opto-Electro-Mechanical System
MUMAS	Multi-mode absorption spectroscopy
ND	Neutral density
NEAS	Nois equivalent absorption sensitivity
NI	National Instruments
OAP	Off-axis parabolic
PCI	Peripheral-component interconnect
PNNL	Pacific Northwest National Laboratory
QCL	Quantum Cascade Laser
RMSE	Root mean square error
SDK	Software Development Kid
TEC	Thermo-electric cooling
TLAS	Tunable Laser Absorption Spectroscopy
USB	Universal Serial Bus
VB	Valence band
WMS	Wavelength Modulation Spectroscopy

Chapter 1

Introduction and motivation

This thesis covers the topic of direct laser spectroscopy in the mid-infrared (MIR) for the quantitative sensing of multi-species hydrocarbon gas mixtures. The involved research includes the acquisition of unknown transmission spectra of the investigated gas species. In addition, mutual spectral broadening parameters of the gases in binary mixtures were investigated and for the first-time quantitative laser spectroscopic measurements of seven component mixtures in the chosen MIR fingerprint range were demonstrated. These achievements comprise the developments of a laboratory-based gas sample preparation system and a broadly tunable laser spectrometer. Also, the measurement conditions were investigated and a new measurement procedure as a sophisticated signal processing were developed which allow to obtain high resolution and high accuracy spectra of the gases from the recorded measurement data. The spectra either compare to state-of-the-art available database spectra or reveal so far undocumented and therefor unavailable gas transmission measurements.

Optical gas sensing [1] is a vivid field of research and has various applications. The measurement of so far undocumented gas spectra as the development of new measurement techniques and especially new laser sources for spectroscopy have strongly stimulated the investigations in the preceding decades. The multiple applications include environmental fields as atmospheric research and monitoring, exhaled breath analysis for medical diagnosis, security applications as gas leak detection and the monitoring of industrial combustion gases or gases in process streams [2, 3]. In this context multi-component gas sensing is particularly challenging raising scientific questions as the spectral behavior of the gases in mixtures and the development of appropriate spectral models. This includes also research regarding the realization of measurement techniques, procedures and the respective signal evaluation.

The specific application that motivated this research work is the measurement of gas mixtures of the first seven alkanes which occur as components in process streams of the petro-chemical industries. An optimum refinery plant operation and thus the control of the streams requires the measurement of multiple parameters as e.g. pressure, temperature, flow velocities and especially the accurate determination of composition and concentration of the components. The development of multi-component gas analyzers which enable accurate, reliable and ideally real-time measurements are a longtime demand of the

respective industries.

Real-time spectroscopic measurement systems for this application are currently unavailable. Gas chromatographs (GCs) [4], which decompose the process stream to measure the concentration of each constituent, are a matured and the most widely employed technology. But their use implies drawbacks as the necessity of sophisticated and cost-intensive measurement and calibration systems and a delayed response which prevents closed feedback-loop operation of the process. As optical measurement technique for the spectral acquisition of the targeted hydrocarbons Fourier transform infrared (FTIR) spectroscopy is widely used. FTIR spectrometers allow for an extremely broad spectral coverage in the infrared and are often used as systems for acquiring the reference database spectra of the investigated alkanes [5]. But FTIR spectrometers suffer from trade-offs between sensitivity, path length and spectral resolution due to the employment of incoherent light sources. The spectral resolution of 0.001 cm^{-1} that has been achieved in the thesis approach would imply the application of an FTIR spectrometer with 10 m optical delay path. Despite the delicate handling of such large equipment path length enhancement also results in lower sensitivity and requires sophisticated periodic re-calibration. This limits the industrial applicability of FTIR spectrometers [6].

A spectroscopic multi-species gas analyzer would have to combine fast, robust and maintenance-free sensing which would allow to reduce measurement costs and an operation of the process closer to its optimum due to the faster measurement results. Laser absorption spectroscopy demonstrated already for several decades to be an ideal technology for gas sensing in the near infrared and could be employed for multiple industrial applications [7, 8]. The narrow bandwidth, high intensity and tunability of laser emission allow for selective, highly sensitive and dependent on the target gases for single to multi-species gas detection and therefore promise to enable the development of universal and cost-effective spectrometers. Despite these advantages multi-species gas detection remains challenging due to the requirement of broad spectral coverage for sensing multiple gases. Potentially higher detection sensitivities and selectivity can be achieved in the MIR fingerprint region, due to the stronger absorbance of the gases. In the first decades of laser development lead salt lasers that are emitting in this wavelength range were cumbersome in their handling and could only be realized at cryogenic temperatures [9, 10] which made them unsuitable for field applications.

In the last two decades the invention and rapid development of Interband Cascade Lasers (ICLs) [11, 12] and Quantum Cascade Laser (QCLs) [13–15] provided laser emission in the MIR at room-temperature and opened the important fingerprint region to laser spectroscopy.

The thesis was executed in connection with an European Union (EU) funded project for the development of "Inline-Cascade-Laser Spectrometers for Process Control" (iCspec). The iCspec-project intended to investigate the feasibility of sensing hydrocarbon multi-species gas mixtures with both laser technologies (ICLs and QCLs) in two different wavelengths ranges. The final target of the project was to develop gas analyzers for field use.

The research focus of the thesis was to acquire fundamental knowledge about the sensing of the gases by developing a QCL-based laboratory setup. Beside choosing an appropriate spectral range and coverage, sensing of multiple gas species requires high resolution and high accuracy reference spectra of the pure gases to discriminate the different components of a gas mixture. In addition, the spectral transmission is influenced by the mutual interaction of the gases that depends on the mole fractions of the respective species in the mixture [16]. Both, high resolution spectra of alkanes and the so-called broadening coefficients that describe collisional effects on the gas spectra are only partly covered in current databases. Hence, the development of a laser spectroscopic measurement system, the acquisition of the respective transmission spectra and an investigation of the gas interaction parameters are conditions for realizing quantitative multi-component measurements of hydrocarbon gas mixtures and has not been investigated in such detail before.

To summarize, the central research questions and development objectives have been:

- the planning and development of a laboratory environment that allows for versatile direct absorption measurements of the gases,

- realizing a measurement method and signal processing that yields high resolution and highly accurate transmission spectra,

- the investigation of the spectral quality and the sensitivity limitations of the measurement setup,

- obtaining reference spectra of the targeted alkanes that are unavailable in databases,

- examining and quantifying the effects of collisional broadening on the spectra of mixtures of the gases,

- the quantitative evaluation of spectral measurements of multi-component mixtures containing all seven alkanes and delineating remaining limitations and challenges.

In the following chapters, first an overview of the fundamentals of ro-vibrational transitions in gas molecules, tunable laser absorption spectroscopy and the principles of QCLs will be given, cf. Chapter 2. Subsequently, the developed laboratory system including the developed gas sampling system and the automation of the setup will be introduced, cf. Chapter 3. Chapter 4 explains the main aspects of the heart of the measurement system: the spectroscopic setup, and the relevant properties of its components. After the explanation of the measurement technology, the developed method for obtaining high resolution spectra and the processing of the signals for improving quality and accuracy of the spectra are presented. By analyzing the obtained spectra the limits of the measurement sensitivity of the setup are verified and discussed in Chapter 5, aswell. The acquired pure gas reference spectra and their application to quantitative gas mixture analysis are described in Chapter 6. This comprises the investigation of collisional broadening for binary mixtures and the testing of a method that compensates broadening effects in the evaluation of the spectra. Finally, the achieved results are summarized and an outlook for

improvements of the measurement technique and prospects of further investigations are discussed in Chapter 7.

Chapter 2

Fundamentals of laser based mid-infrared gas spectroscopy

For explaining the approach that was chosen for the multi-species detection of hydrocarbon gases in the mid-infrared by laser-based spectroscopy fundamental aspects of three topics should be addressed:

- a brief overview of the basics of ro-vibrational gas absorption spectra with an illustration of their properties in the spectra of the measured hydrocarbon gases and the description of line profiles in infrared spectra (Section 2.1),

- the general measurement method of tunable laser absorption spectroscopy (TLAS) and how it was realized for the hydrocarbon measurements (Section 2.2),

- the principles of quantum cascade lasers and the specifics of external-cavity quantum cascade lasers which were employed as widely tunable and narrow band light source for the absorption measurements of the gases (Section 2.3).

This overview is intended to give sufficiently profound insights into the respective fundamentals to comprehend the chosen approach for the later investigations without excessively deepen into the enormous extent of the underlying fields of research. The investigations were motivated by the discrimination of multi-component gas spectra. Thus, the following sections should allow to understand the properties of the later presented spectral measurements, the employed measurement method of laser spectroscopy and the reasons for choosing quantum cascade lasers as radiation source for multi-species gas detection.

2.1   Emission and absorption

Emission and absorption of light in gas molecules results from transitions between discrete energetic levels of the respective molecule. While the transitions can occur due to a multitude of processes as coupling of the molecule to an electro-magnetic wave, radiative or non-radiative disexcitation or collision-induced absorption [16], generally the difference
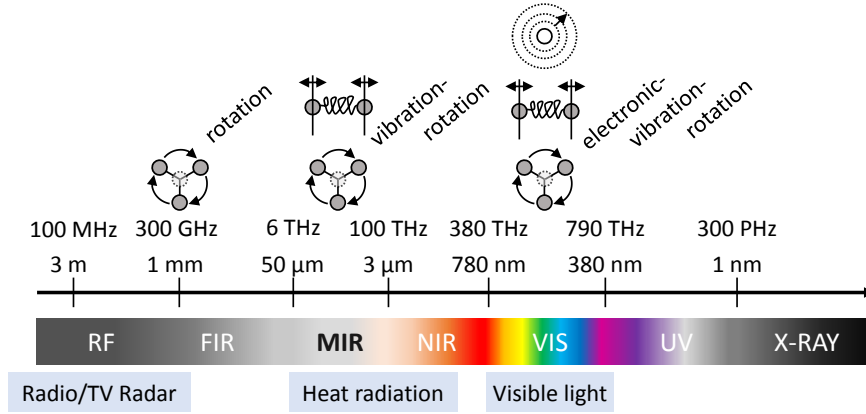
Figure 2.1: Illustration of the different types of energetic transitions in molecules and their correlation to frequencies and the respective wavelengths in the electro-magnetic spectrum (adapted from [17]).

of two energetic levels E_j and E_i is connected to the frequency f or wavelength λ of the coupling light by

$$E_j - E_i = hf = \frac{hc}{\lambda} = hc\nu \tag{2.1}$$

where h is the Planck constant, c the speed of light in the medium and ν the inverse wavelength or wavenumber. For spectroscopy of gas species in the infrared the three magnitudes wavelength λ, wavenumber ν and frequency f are interchangeably used. Their relation and the units that are usually used for the measured spectra in the infrared are given in Eq. 2.2 and will be employed in this thesis.

$$
\begin{aligned}
&\text{wavelength}: \lambda \text{ in } \mu\text{m} \\
&\text{wavenumber}: \nu = \frac{1}{\lambda} \text{ in cm}^{-1} \\
&\text{frequency}: f = \frac{c}{\lambda} \text{ in GHz or MHz}
\end{aligned}
\tag{2.2}
$$

While wavelength is usually used for the central emission of a laser, wavenumber is commonly used for the range of the infrared spectra and frequency often applies to the width of a spectral absorption feature or the laser line width.

The energetic transitions of gas molecules are connected with different phenomena as the excitation of rotational or vibrational motion of the molecule or the excitation of electronic levels. The transitions may occur simultaneously but their fundamental excitations originate from strongly different levels of energy, thus at separate frequencies as illustrated in Figure 2.1.

This picture is supported by the Born-Oppenheimer approximation being a fundamental finding of the early quantum mechanics [18]. It simplifies the Schrödinger equation of a molecule by first solving the electronic wave function with fixed position of the nuclei and

then solving the equation for the nuclear wave function with electronic potential energy curves of the first solutions with non-moving nuclei. The approximation originates from the assumption of different timescales of electronic and nuclei motion due to their large difference in mass. Therefore, the equation can be split to treat the effects separately. The energy parts of the equation are expressed as an expansion of κ being the square root of fourth order of the ratio of the electron mass m and the mass of the nuclei M (see Equation 2.4). The zeroth order of the expansion corresponds to electronic energies E_{el}, the second order to the vibrational levels E_{vib} and the fourth order to the rotational energies E_{rot} leading to the following relations for the scale of the energies

$$\Delta E_{nucl} \approx \Delta E_{el}\kappa^2 \qquad\qquad \Delta E_{rot} \approx \Delta E_{vib}\kappa^2 \qquad\qquad (2.3)$$

with

$$\kappa = \sqrt[4]{m/M} \qquad\qquad \text{(in the order of 0.1).} \qquad\qquad (2.4)$$

The approximation yields good quantitative results for diatomic molecules in the ground state. The quantitative treatment of polyatomic molecules would require to extend the expansion to higher order terms that take coupling effects of the different transition into account that affect the energy levels and wave functions. But the approximation completely defines the quantum numbers of the molecule and thus reveals a correct qualitative picture of the transitions.

In consequence absorption spectra in the mid-infrared originate from ro-vibrational transitions of the molecules. Their general properties and the resulting characteristics for the spectra of the targeted hydrocarbons will be delineated in the following.

2.1.1 Ro-vibrational transitions of gas molecules

The transitions of gas molecules due to absorption of mid-infrared radiation occur by exciting rotational and vibrational movements of the molecule. In accordance with the Born-Oppenheimer approximation for simple diatomic molecules these effects can be treated separately. Thus, the principles of rotational and vibrational transitions for diatomic molecules will be briefly explained before the characteristics of the superimposed spectra of polyatomic molecules will be illustrated.

Rotational transitions The basic model for rotational transitions is the rigid rotator of a diatomic molecule [19]. The molecule is considered according to the dumbbell model of two atoms with a constant bond length that can rotate around a two-fold degenerated axis perpendicular to the bond (see Figure 2.2). The frequencies of the quantized rotational energies are in the microwave range as illustrated in Figure 2.1.

The treatment of the rigid rotor with the Schrödinger equation reveals a quantized angular momentum L:

$$L = \sqrt{J(J+1)}\hbar \qquad\qquad (2.5)$$
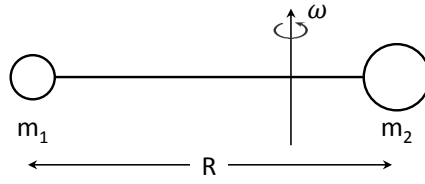
Figure 2.2: Rigid rotator model of diatomic molecule as dumbbell with atomic masses m_1 and m_2, atomic distance R and rotation around an axis with angular frequency ω.

The rotational quantum numbers J apply for the $2J + 1$ degenerated energy eigen-values E_{rot} of the rotational levels

$$E_{rot} = BhcJ(J + 1) \tag{2.6}$$

with

$$B = \frac{h}{8\pi^2 c\Theta} \qquad \left[\text{cm}^{-1}\right] . \tag{2.7}$$

The rotational constant B is inversely proportional to the moment of inertia Θ of the molecule and specifies the spacing of the rotational energies. Its dependence on the moment of inertia obviously shows that larger molecules with a higher moment of inertia possess rotational levels at lower energies and with smaller spacing of the transitions.

The frequency of transition f between two neighboring rotational levels E_{J+1} and E_J with

$$hf = E_{J+1} - E_J \tag{2.8}$$

is thus directly given by B and the level number. For the wavenumber of a rotational transition $\nu_{J \to J+1}$ from a lower J to a higher level $J + 1$ by absorption generally applies:

$$\nu_{J \to J+1} = 2B(J + 1) . \tag{2.9}$$

This yields a spectrum of with $2B$ equidistantly spaced rotational lines for the rigid rotator model. Precondition for the observation of a rotational spectrum is a permanent dipole moment of the molecule that can couple to the electro-magnetic wave exciting a transition. In addition only transitions with the quantum number difference $\Delta J = \pm 1$ are allowed as they change the angular moment of the molecule by $\hbar$ which equals to the angular momentum of the absorbed photon and complies with the conservation of angular momentum.

The magnitude of the rational constant and therefore the rotational line spacing is in the one to two digit wavenumber range for small molecules and thus much smaller than the thermal energy at room temperature which is approx. 200 cm^{-1}. Hence, in thermal equilibrium at room temperature several rotational levels are occupied. The transition intensities are dependent on the degeneracy of the level and the Boltzmann distribution for the thermal occupation yielding a maximum at medium rotational levels J at room temperature, cf. Fig. 2.3b.

This simple model of the rigid rotator illustrates the major properties of rotational

spectra. More refined models describe the rotational motion with non-rigid rotators that allow for changing bond length due to centrifugal distortions. A changing bond distance affects the moment of inertia and therefore B and the energy levels and level spacing. Also polyatomic molecules may have up to three non-degenerated rotational axes leading to three rotational constants to describe the rotational movement of the molecule and introducing further quantum numbers for the rotational level splitting.

The quantum mechanical description of these rotational transitions is highly complex and far exceeds the purpose of this brief overview. But a qualitative understanding of the spectra of the hydrocarbon molecules bases on theses properties.

Vibrational transition Molecules have further inner degrees of freedom by vibrational movements of its atoms around their equilibrium position. The frequencies of the vibrational transitions occur in the infrared region of the electromagnetic spectrum. As basic model for a vibrational excitation again a two-atomic molecule can be analyzed that shows only one stretching vibration along the bond axis of the molecule. Hence, the bond length changes in contrast to the rigid rotator.

In the harmonic oscillator model the potential of the restoring force for a deviation of the atom positions R from equilibrium position R_e is assumed by a parabola potential $\sim (R - R_e)^2$ and a classical spring constant k. The quantum mechanical treatment reveals the vibrational energy levels E_{vib} of the harmonic oscillator

$$E_{vib} = \hbar\omega(\nu + 1), \qquad \nu = 0,\ 1,\ 2... \tag{2.10}$$

with ω the classical oscillator frequency

$$\omega = \sqrt{\frac{k_s}{m_r}} \tag{2.11}$$

that is defined by the square root of reduced mass m_r of the molecule and spring constant k_s of the bond. The quantum number ν counts the transition levels of the quantized vibration. The vibrational transition must be associated with a change of the electric dipole moment of the molecule to be infrared active. For the harmonic oscillator also the selection rule $\Delta\nu = \pm 1$ applies which leads due to the equidistant energy level spacing to the prediction of a single line position in the spectrum as all transitions overlap.

But the spectroscopic analysis of molecules shows further transitions revealing that the harmonic oscillator is only a good approximation for low vibrational states of the molecule. The adoption of a molecule specific anharmonic empiric Morse potential represents a more correct model for the binding potential of the molecule by including the repulsion of nuclei for smaller distance R and the occurrence of dissociation for larger R. The calculation with the adapted potential and the parametrization of the eigen-values in terms of a power series

in the vibrational number yields better approximations of the vibrational levels ν [20]. In Equation 2.12 only the quadratic term of the expansion is kept

$$E_\nu = \hbar\omega_e(\nu + \frac{1}{2}) - x_e\hbar\omega_e(\nu + \frac{1}{2})^2 \tag{2.12}$$

including the correction by the anharmonicity constant x_e which is molecule specific and in the order of 0.01 and employing ω_e the angular frequency of the fundamental oscillation. It reveals a decreasing spacing of for increasing vibrational levels as x_e is generally positive. For the anharmonic oscillator also overtone transitions $\Delta\nu = \pm 1, \pm 2, \pm 3, ...$ are allowed but show decreasing relative intensities in the order of $1 : x_e : x_e^2 : x_e^3$.

As the vibrational transitions occur at higher energies than the rotational, the most relevant transitions at room temperature originate from the ground state to higher levels. These transitions typically lie in the MIR, which is why it is studied here as there are the most intense transitions. Respectively, higher levels are scarcely occupied and higher order transitions have much lower intensities.

Ro-vibrational spectra In the infrared spectra of gas molecules rotational and vibrational excitations are superimposed and coupled corresponding to a rotating oscillator. Thus, energetic levels of excitation cannot be considered fully separated anymore. The resulting energy of the combination of both transitions is given in Equation 2.13 with the first order corrections of the coupling effects.

$$\begin{aligned} E(\nu, J) &= E_{vib}(\nu) + E_{rot}(J) \\ &= \hbar\omega(\nu + \frac{1}{2}) - x_e\hbar\omega(\nu + \frac{1}{2})^2 + hcB_\nu J(J+1) - hcD_\nu J^2(J+1)^2 \end{aligned} \tag{2.13}$$

The rotational vibrational correction B_ν takes the higher average atomic distance $\langle R \rangle$ for vibrational excitation into account that increases the moment of inertia of the molecule and D_ν corresponds to the centrifugal correction for higher rotational levels. The resulting spectra reveal the vibrational transitions with a superimposed rotational fine structure.

Equation 2.13 still applies to the simple two-atomic molecule with a single vibrational normal mode and twofold degenerated rotational mode. For polyatomic molecules the general degrees of freedom correspond to the number of atoms N to in total $3N$. Hence, a non-linear molecule with no degeneration of the rotational axis has three rotational degrees of freedom and three translational degrees of freedom yielding $3N$-6 normal vibrations of the atoms that can be excited. Usually not all of these modes are infrared active as the selection rules for a transition still involve the change of the molecular dipole moment. For methane as smallest alkane with $N = 5$ atoms this results in $3N - 6 = 9$ normal vibrational modes. Due to degeneracy 4 fundamental frequencies ν_i are observed [21].

The quantum mechanical treatment of the transitions of polyatomic molecules increases in complexity with the number of atoms and requires symmetry considerations to keep the description manageable. But the general properties base on the same characteristics as the diatomic model allowing a qualitative understanding of the spectral shapes. In Figure 2.3b
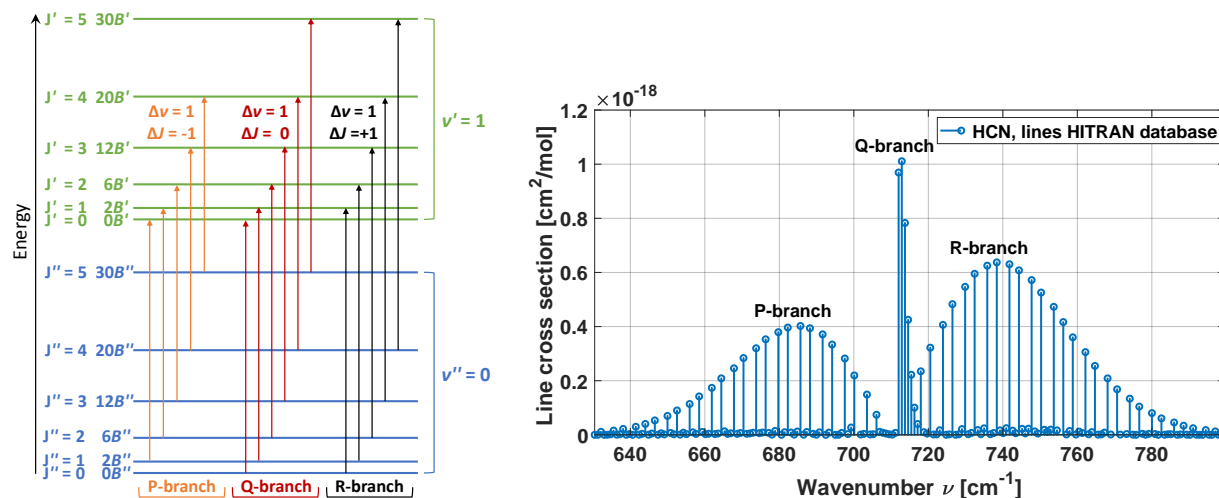
(a) Generic diagram of the rotational branches (P,Q,R) of a fundamental vibrational transition $\nu'' \to \nu'$.

(b) Simulation of the line cross sections of the rotational fine structure of the fundamental bending vibration ν_2 of the HCN molecule based on HITRAN [22] parameters and Matlab routines.

Figure 2.3: Illustration of a rotational-vibrational band of molecular transitions.

the line cross sections for a ro-vibrational transition of the HCN molecule are simulated and in 2.3a the exemplary selection rules for the transition branches are illustrated.

A vibrational transition from a lower level ν'' to a higher level ν' is related with rotational transitions with the general selection rule $\Delta J = \pm 1$. For certain vibrations also $\Delta J = 0$ may apply. This results in branches or bands of transition lines in the spectrum called P-branch for $\Delta J = -1$, Q-branch for $\Delta J = 0$ and R-branch for $\Delta J = +1$. The energetic spacing of the transitions leads to the characteristic signature of the ro-vibrational spectrum and can be used to calculate molecular properties as bond lengths or bond angles.

Mid-infrared spectra of alkanes ($C_1 - C_5$) Vibrations of specific molecular groups have their fundamental transition at a certain energy thus wavenumber of the spectrum. They are called characteristic vibrations and can be used to identify functional groups or structural moieties of a molecule by the measurement of infrared transmission spectra. The characteristic stretching vibration of the C-H bond is centered at 3 μm or ~ 3000 cm^{-1} and can be also found in the absorption spectra of alkanes. The overall structure of the molecule has a weak influence on the energetic position of these vibrational modes leading to very congested and strongly overlapped ro-vibrational spectra for the $C_1 - C_5$ alkanes in this spectral region.

The range below 1500 cm^{-1} of the absorption bands is called molecular fingerprint and results from strongly coupled vibrational modes. The transition line positions are determined by the molecular structure and are thus specific for a molecular species. Spectra in this range are well suited to identify or discriminate molecular species. For alkanes the bending vibrations of the C-H bonds occur around 6.8 μm or 1470 cm^{-1}.
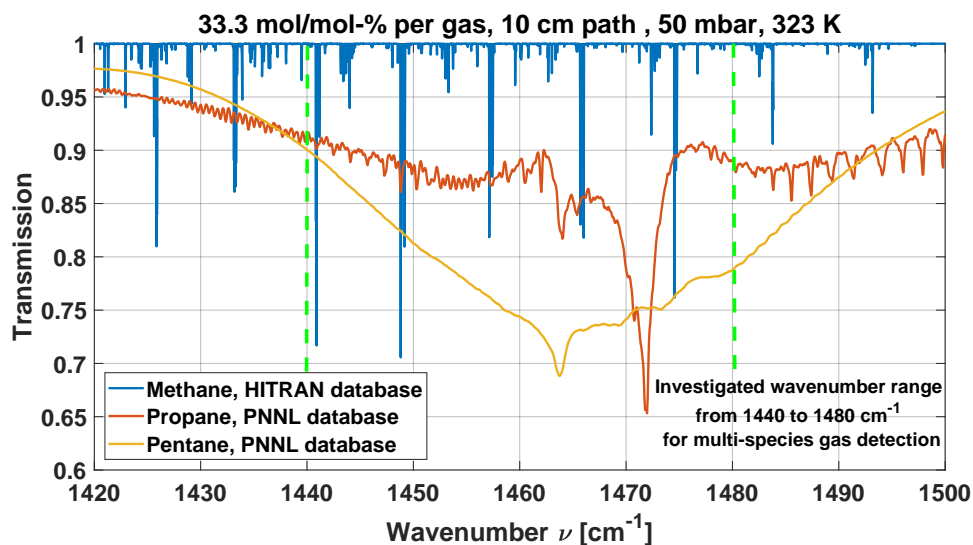
Figure 2.4: Simulated transmission spectra of methane, propane and pentane at the later measurement conditions for path length, pressure and temperature. The investigated wavenumber range for the later quantitative sensing of gas mixtures is indicated by the vertical dashed green lines.

Therefore, the alkane spectra in this range are well applicable for quantitative multi-species gas detection as they can be better discriminated than in the 3 µm region. In Figure 2.4 the simulation of transmission spectra for methane, propane and pentane at the later measurement conditions are depicted. The simulation is based on tabulated spectra from databases. The accuracies and limitations of the database spectra will be discussed in the Results chapter, cf. Section 6.1.2. The here given depiction is just an illustration that neglects effects on the spectral shape due to gas pressure or different components in a mixture.

But the general properties of ro-vibrational spectra that were discussed before can be directly applied to these spectra. For methane a multitude of resolved rotational lines can be identified while the center of the vibrational transition cannot be found in the depicted range. The propane transition shows a Q-branch structure close to 1470 cm^{-1} and partially resolved P- and R-branches on the respective sides of the spectrum. The pentane spectrum is centered closer to 1460 cm^{-1} while the transitions are so densely packed that no resolved rotational transition lines can be identified.

The spectra illustrate the increasing number of vibrational modes and the extensive coupling with increasing size of the molecules. Also the decreasing spacing of the rotational lines for larger molecules due to the larger moment of intertia and therefore smaller rotational constants can qualitatively explain the unresolved pentane spectrum.

For the quantitative analysis of transmission spectra, especially when measured in superposition in a gas mixture, the discrimination of resolved lines from unresolved bands gains in interest. Hence, the knowledge of accurate spectral models relying on measured

absorption cross sections and calculated line parameters is required. The latter is realized by different line shape models that describe the profile of isolated transition lines. An overview of the underlying physics and their properties will be given in the following.

2.1.2 Line strength and line profile

As outlined before the position of ro-vibrational transitions and their spacing is related to the respective molecular parameters as internuclear spacing or bond angles. These energetic transitions are not purely monochromatic but broadened due to different physical influences. A measured transmission of a gas and the respective transition line widths are governed by the influence of environmental parameters as composition, temperature and pressure [23]. The dominating effects for the appearance of the measured transmission spectra will be introduced in the following.

The strength of a transition line is directly proportional to the quantity of absorbed light at the respective wavenumber ν of the line position. For a transition of the states $1 \rightarrow 2$ the line strength S_{12} is a function of the density of the absorbing species n_1, the Einstein coefficient of the transition B_{12} and the temperature of the gas T. The temperature dependence of the transition strength corresponds to the Boltzmann distribution that determines the occupation of the transition states. Then one has for S_{12}

$$S_{12} = \frac{h\nu}{c} n_1 B_{12}(1 - \exp(-h\nu/kT)) \qquad \left[\text{cm}^{-2}\right] \tag{2.14}$$

with

$$n_1 = \frac{p_1}{kT} \tag{2.15}$$

where p_1 is the partial pressure of the absorbing species and k the Boltzmann constant. The width or broadening of a transition is described by a respective profile function $\phi(\nu)$ over the absorbing wavenumber range. The integral over the wavenumber range of a transition profile is by convention unity:

$$\int_{-\infty}^{+\infty} \phi(\nu)d\nu = 1 \ . \tag{2.16}$$

The profile generally has a maximum at a center frequency ν_0 and decreasing wings on both sides of the center whose relative variation is caused by the respective broadening mechanisms. An understanding of these mechanisms allows a prediction of the line shape function for the gas transition.

For the relative variation in the spectral absorption with wavenumber an absorption coefficient k_ν can be defined that is the product of the strength of the transition S_{12} and the line profile $\phi(\nu)$:

$$k_\nu = S_{12}\phi(\nu) \ . \tag{2.17}$$

This general absorption coefficient is the basis for one of the most important equations in gas transmission spectroscopy: the Lambert-Beer law (Eq. 2.18). It determines the

transmitted intensity $I(\nu)$ dependent on the incident intensity I_0, the absorption coefficient k_ν of the absorbing species and the path L through the absorbing medium:

$$
\begin{aligned}
I(\nu) &= I_0 \exp(-k_\nu L) = I_0 \exp(-A(\nu)) \\
&= I_0 \exp(-n\sigma_\nu L) \\
&= I_0 \exp(-S\phi_\nu pL)
\end{aligned}
\tag{2.18}
$$

The product of absorption coefficient and path length yields the absorbance A of a gas that can be set as the exponent in the equation for the decreased transmitted intensity $I(\nu)$. With a normed absorption coefficient $\alpha(\nu)$ the absorbance can be also written as $A = \alpha_i(\nu)c_i L$ which relates the decrease of transmitted intensity directly to the concentration c_i of the absorbing species. Equivalent to that definition of the absorbance an absorption cross section σ_ν in a normed volume over a normed transmission length per molecule can be determined as indicated in the equations above. The relation to the absorbance is obtained by the species density n and the path L. Eventually, the absorbance can be ascribed again to line strength S, line profile ϕ_ν, pressure p and the absorption path length L.

As illustrated in the previous section for gases commonly a band of transitions is measured over a larger wavelength range which means that several transitions contribute to the absorbing line strengths yielding an absorbance A_{band} that is formed of the superposition of multiple lines S_i:

$$
A_{\mathrm{band}} = pL \sum_i S_i \phi_i
\tag{2.19}
$$

For multiple gas species the respective transitions are documented in databases. Generally, the tabulated line parameters are calculated by theoretical models and verified by measurements. For the alkanes tabulated line parameters of methane and ethane are available in databases while for the larger alkanes from propane to pentane only absorption cross sections at fixed measurement conditions have been determined experimentally and made accessible in the literature.

In the measurements presented later, cf. Chapter 6, both instances are of interest for the quantitative determination of gas mixtures: calculated and measured cross sections. The calculation implies the determination of the line parameters from measured spectra. Therefore, the general profile functions for the transition lines and their important parameters will be elucidated in the following.

Natural line width The most fundamental reason for a broadened transition is given by the finite lifetime τ of the involved states and the resulting energy uncertainty $\Delta E \Delta \tau \geq \hbar$ that imposes a broadening. It is indirect proportional to the lifetime of the upper state τ_2 and the lifetime of the lower τ_1 by $\tau^{-1} = (\tau_1^{-1} + \tau_2^{-1})$.

$$
\Delta f_N = \frac{1}{2\pi}\left(\frac{1}{\tau_1} + \frac{1}{\tau_2}\right)
\tag{2.20}
$$

This natural line width Δf_N occurs for a transition in absence of other molecules, thus without external perturbation of the molecule. The natural broadening results in a Lorentzian profile function with Δf_L as full width half maximum (FWHM).

$$\phi_L(f) = \frac{\Delta f_L/\pi}{\Delta f_L^2 + (f - f_0)^2} \tag{2.21}$$

The ro-vibrational states in the MIR have relative long liftimes of $\tau \sim 10^{-4} - 10^{-3}$ s leading to line width in the order of $\Delta f_N \sim 100$ Hz [24]. Normally, other broadening mechanisms dominate the measured spectrum. Thus, the small contribution of the natural line width can be often ignored.

Doppler broadening - Gaussian profile Another broadening mechanism that dominates the transition line width of a gas at low pressures is the Doppler effect. It is caused by the thermal motion of the molecules. For an observer the absorbed or emitted frequency of a molecule is shifted by Δf due to its relative velocity v_r in the line of sight of the observation:

$$\Delta f = f_0 \frac{v_r}{c} . \tag{2.22}$$

The Doppler shifted frequency depends on the velocity distribution of the gas which is Maxwellian distributed. The transition profile induced by the Doppler broadening reveals a Gaussian function, cf. Eq. 2.23.

$$\phi_G(f) = \frac{2}{\Delta f_G}\sqrt{\frac{\ln 2}{\pi}}\exp\left(-4\ln 2 \frac{(f - f_0)^2}{\Delta f_G^2}\right) \tag{2.23}$$

The FWHM maximum of the Gaussian profile is linear dependent on the central frequency f_0 of the transition as well as on the temperature T of the gas and the mass m of the molecule:

$$\Delta f_G = \sqrt{\frac{8kT \ln 2}{mc^2}} f_0 . \tag{2.24}$$

Thus, the thermal broadening has a larger magnitude for small molecules with a lower mass at fixed temperature. In the fingerprint region of the investigated alkanes the Doppler broadening of methane equals to a FWHM of approx. 140 MHz at room temperature.

Collisional broadening - Lorentzian profile Line broadening also occurs due to mutual interaction of the molecules. Collisions of molecules reduce the effective lifetime of level occupation or change the phase of a ro-vibrational excitation which leads to a broadening of the line widths of the transitions. The broadening increases with higher frequency of molecular collisions. Therefore, the collisional broadening is also termed as pressure broadening as the density of the gas increases with pressure.

The collisional broadening leads to a Lorentzian profile of the transition, cf. Eq. 2.21. The magnitude of the broadening of a transition is dependent on the structure of the molecule,

on the energetic level of the transition and the collisional partner. The absorbing molecule can be interacting with a molecule of the same gas species which refers to self-broadening or with another perturbing gas species.

The broadening is linearly dependent on the gas pressure. Hence, a broadening coefficient γ for a specific transition and a specific perturber gas can be determined. The broadening coefficient corresponds to the half width half maximum of the pressure broadened Lorentzian profile at a gas pressure of one atmosphere. In the databases it is typically tabulated in units of wavenumber per atmosphere (cm^{-1}/atm) at an ambient temperature of 296 K. Therefore, the collisional width ν_C or Lorentz width ν_L is given here as well in this unit. In the case that the absorbing gas is interacting with several gas species in a mixture an average line width $\Delta\nu_L$ of the Lorentzian profile can be calculated when the broadening coefficient γ_i of each species and all gas mole fractions χ_i are known:

$$\Delta\nu_L = \Delta\nu_C = 2p \sum_i \chi_i\gamma_i \; . \tag{2.25}$$

The FWHM $\Delta\nu_C$ of the collision broadened line is then the sum of the products of the broadening coefficient of the gas species γ_i and its mole fraction χ_i multiplied by the overall gas pressure p. The broadening coefficient has an exponential temperature dependence which generally leads to a decreasing Lorentz width for increasing temperatures T.

$$\gamma_i(T) = \gamma_i(T_0)(T_0/T)^{n_\gamma} \tag{2.26}$$

Usually, the coefficient is defined at a standard temperature T_0 and a collisional broadening temperature exponent n_γ is determined from several measurements to describe the temperature dependence. As the collisions cause a perturbation of the energetic levels of the interacting molecules also a shift of the central wavenumber of the transition may occur. These shifts also increase with the gas pressure. However, for the transitions of alkanes in the MIR pressure shifts are very small, e.g. in the order of 100 MHz for methane [25] at ambient conditions. But the later presented measurements have been acquired at a reduced pressure of 50 mbar. Line shifts are therefore ignored in the following.

For methane lines an average self-broadening FWHM for transitions in the fingerprint region of approx. 4.2 MHz/mbar can be determined [25]. Hence, at a pressure of 30 mbar the broadening is in the range of the Doppler broadening while the Lorentzian profile dominates for ambient gas pressure.

Voigt line profile   At ambient measurement conditions transmission spectra are always broadened due to the overlapping effects of thermal motion and gas pressure. At moderate and reduced pressures neither the Gaussian profile of the Doppler broadening nor the Lorentzian profile from the collisional broadening dominate. Thus, another profile function has to be applied to better describe the transition line shape.
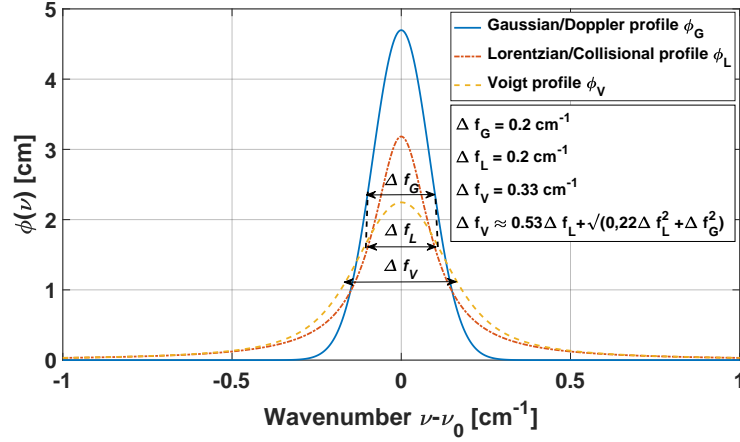
Figure 2.5: Comparison of line profile function for identical line width of Gaussian Δf_G and Lorentzian Δf_L profile and resulting Voigt profile width Δf_V according to equation 2.28.

The Voigt profile ϕ_V considers both broadening effects by a convolution of the Gaussian and the Lorentzian profile:

$$\phi_V(f, \Delta f_G, \Delta f_L) = (\phi_G * \phi_L)(f) . \tag{2.27}$$

An analytic closed form expression for the Voigt profile does not exist. But empirical solutions or approximations as the pseudo Voigt profile are commonly used that employ the linear combination of a Gaussian curve and a Lorentzian curve instead of their convolution [26]. An accurate evaluation of the integral can be defined with the Faddeeva function [27]. This is used for the analysis of the measurement results and therefore discussed in the respective result Section 6.2.1.2.

The FWHM of the Voigt curve consists of a portion from the Gaussian and from the Lorentzian part of the profile. An empirical approximation with a maximum error of 0.02 % was found by Olivero and Longbothum [28] and is often used to determine the Voigt FWHM Δf_V from tabulated Gaussian Δf_G and Lorentzian Δf_L width:

$$\Delta f_V \approx 0,5346\Delta f_L + \sqrt{0,2166\Delta f_L^2 + \Delta f_G^2} . \tag{2.28}$$

The gas line parameters in databases are also usually determined for the application of the Voigt profile function [29]. For illustration a comparison of the three introduced profiles and their FWHM is shown in Figure 2.5.

The calculation of line parameters from measured transmission profiles requires high resolution measurements. Transition line widths in the fingerprint region of methane are in the range of a few hundred MHz as exemplified before. A measurement method that allows for high resolution and thus discrimination of narrow spectral features is the tunable laser absorption spectroscopy. General principles of the method and the specific context for the sensing of the alkane mixtures will be delineated in the following.

2.2   Tunable laser absorption spectroscopy

The application of lasers for absorption spectroscopy is a long time used and versatile applied technology [8, 30]. The properties of laser light with high intensities, collimation, coherence, spectrally narrow emission and wavelength tunability allow for obtaining spectral measurements with much higher resolution and sensitivity than could be realized with incoherent broadband light sources. Thus, narrow transition lines can be resolved leading to the possibility of selective and quantitative gas sensing.

The objective of sensing a gas species by laser absorption spectroscopy requires to chose a transition of the gas, a laser that emits in this wavelength range and the suitable detector [1, 31]. As outlined before the fundamental ro-vibrational transitions of gas molecules can be found in the mid-infrared spectrum. Figure 2.6 illustrates a multitude of technically relevant gases, the wavelength position where they exhibit strong transitions and available laser technologies that emit in the respective wavelength range.

In order to cover the molecular fingerprint region quantum cascade lasers are the predestined laser technology. For the hydrocarbon sensing a wide tuning range is required to measure broad band absorbers, cf. Fig. 2.4, as the heavier alkanes while
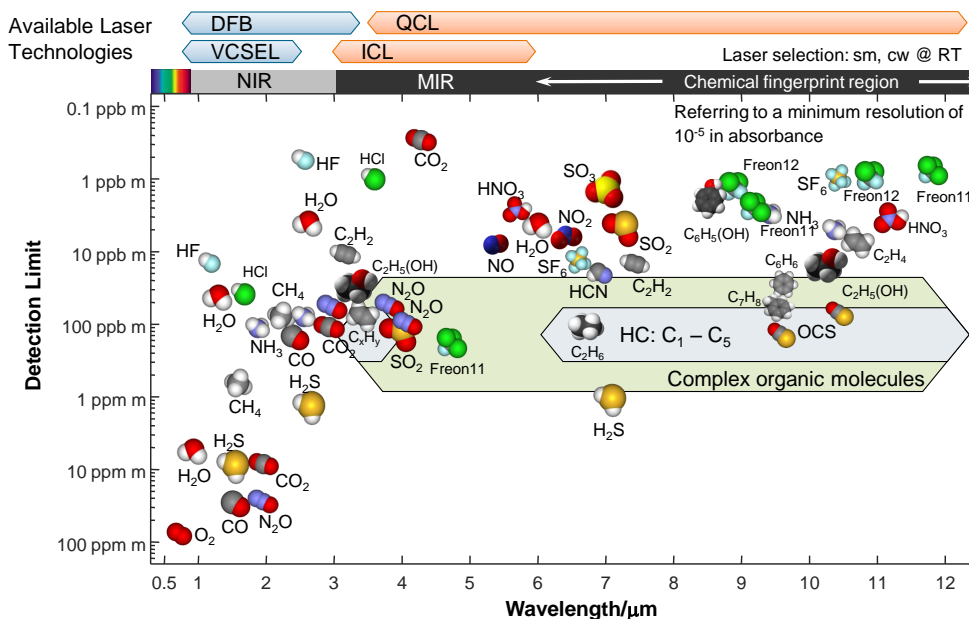
Figure 2.6: Technically relevant gases and preferred sensing wavelength for minimum detection limits. The detection limit corresponds to a concentration in ppm (parts per million) or ppb (parts per billion) per meter absorption path assuming that the noise equivalent absorption is 10^{-5}. The available laser technologies compare typical emission wavelengths of diode lasers emitting single-mode continuous-wave at room temperature to ICL and QCL emission ranges (diagram adapted according to Ref. [32]).
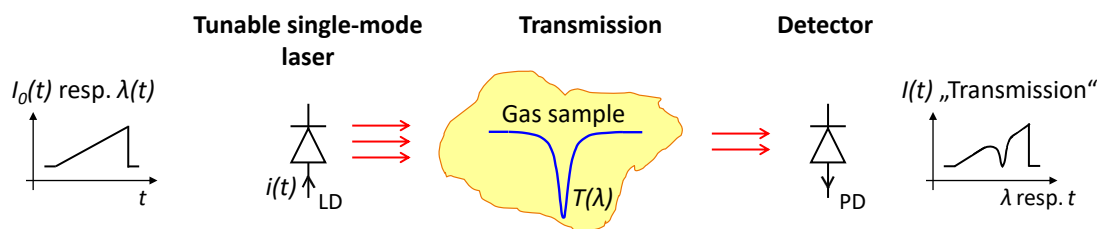
Figure 2.7: For direct absorption spectroscopy the emission ($\lambda(t)$, $I_0(t)$) of a tunable single-mode laser, e.g. form a laser diode (LD), is sent through a gas sample. The transmitted intensity $I(t)$ is recorded with a detector, e.g. a photo diode (PD).

guaranteeing high resolution to discriminate narrow spectral features of the smaller molecules. The principles of the employed laser source for this purpose will be introduced later, cf. Section 2.3. Before, a brief introduction to direct absorption spectroscopy will be given, cf. Section 2.2.1, and subsequently the aspiration for the spectral measurements are explained, cf. Section 2.2.2.

2.2.1   Direct absorption spectroscopy

Direct absorption spectroscopy is the most straightforward implementation of laser-based absorption techniques. In Figure 2.7 a schematic diagram is given in order to illustrate the technique. The beam of a tunable single-mode laser is sent through a gas sample and the transmitted intensity is measured with a detector. In the depiction the common symbol of a diode laser is used to generally illustrate an emitting laser source as it applies to the general principle independent of the wavelength range or an applied laser technology. However, the tunable single-mode laser sources for the later presented gas sensing results are QCLs (cf. Section 2.3).

The transmitted intensity $I(t)$ is generally described by the previously introduced Lambert-Beer law in Eq. 2.18 and thus dependent on the incident intensity $I_0(t)$ and the wavelength dependent absorption of the measured gas species. The transmitted power as function of the emitted wavelength $\lambda(t)$ of the laser yields the transmission spectrum of the gas sample.

The explanations on the line strength and line profile, cf. Section 2.1.2, illustrated the dependence of the spectral shape on properties of the sample as gas mole fractions, pressure, temperature and path length. If one figure is unknown it can be determined by the measured transmission spectrum and the spectral model of the gas absorption. For the measurements of the targeted hydrocarbons especially the determination of the mole fraction of the different components of the gas sample were of interest. Hence, the measurement procedure was designed to realize measurements at constant path length, pressure and temperature.

2.2.2   Absolute gas spectroscopy

The laser spectroscopic measurements of gases most frequently targets the determination of one of the following properties of the gas species: concentration c, pressure p or temperature T. A multitude of techniques [1, 24] have been developed that find application [6, 33] in various fields. For the measurement of the respective gas property commonly an isolated line is chosen. From the single line transmission spectrum the absorption strength and the line width are determined. This applies especially for small molecules with well separated rotational fine structure.

Relying on database values of the measured transition and the line shape model the gas parameters (c, p, T) can be determined. These measurements frequently do not require the exact determination of the line position as for example line locking techniques fix the laser emission by the transmission through a reference gas cell with the targeted gas species. In the case of trace gas concentration measurements also the line shape is not always of interest but only the peak value of the isolated absorption line. As well, the detection of isolated lines has the advantage that peaks can be compared against a flat background and are not overlapped by other transitions.

The illustration in Figure 2.4 shows that this cannot be assumed for the sensing of several alkanes in a gas mixture. The simultaneous sensing of small molecules with resolved rotational transition lines and large molecules that possess broad band unresolved absorption spectra demands an exact determination of the spectral position and the measurement of undistorted line shapes to discriminate overlapping species in a mixture and enable quantitative measurements.

In the literature applications of laser-based mid-infrared spectroscopy were reported that referenced the mid-infrared radiation of a sensing laser to the highly exact teeth positions of a near infrared laser frequency comb. The measurements allowed determination of transition line positions with uncertainties in the range of a few hundred kHz [34, 35]. The authors termed their techniques as absolute spectroscopy that are suitable to verify theoretically determined line positions and improve the accuracy of database parameters or spectral models.

Although, a different measurement approach was chosen for the measurements of the alkanes, the obtained spectra in this thesis also aim to realize high accuracy of their position in the frequency axis, minimum deviations of the spectral shape and high spectral resolution. The purpose of the measurements is to realize reference spectra of the pure gases that can be either compared to the existing database spectra or provide spectra that are not documented in databases at the required resolution or the targeted environmental conditions of the measurements, respectively. Thus, absolute spectra serve as basis for the discrimination of gas species in mixtures and the quantitative evaluation of the mole fractions of the mixture components.

The developed laboratory system, the measurement procedure and the evaluation of the signals to obtain absolute referenced spectra are the topic of the following chapters. However, the key component to measure the gas transmission in the mid-infrared is the appropriate laser. Figure 2.6 indicated different laser technologies and their respective

range of emission. Hence, quantum cascade lasers (QCLs) allow for obtaining mid-infrared radiation to measure the fingerprint of the alkanes. In the following the basic principles of QCLs will be highlighted. The function principle and the advantages compared to their diode laser counterparts for mid-infrared emission as well as to interband cascade lasers are outlined. Finally, the properties of external-cavity quantum cascade lasers (EC-QCL) are described which allow to realize broadband and high resolution spectral measurements.

2.3 Quantum Cascade Lasers

Interband diode lasers were the first semiconductor laser sources that were applied for tunable laser spectroscopy in the near infrared [36]. The wavelength that is emitted by diode lasers is determined by the band gap of the semiconductor material. An interband transition or recombination of electrons from the conduction band with holes in the valence band emits a photon of the energy $h\nu$. Obtaining emission in the MIR range requires very small band gaps. Lead salt material systems satisfy this small band gap condition but the lasers entail certain disadvantages as they suffer from poor mechanical properties, low efficiencies and can only be operated at cryogenic temperatures [37].

A different concept for laser emission in semiconductor structures instead of the bipolar diode principle was theoretically investigated by Kazarinov and Suris in 1971 [38]. They described a light amplification process in a periodic superlattice under application of a strong electric field. Photons can be generated from transitions of electrons or holes in confined subband states in the conduction or valence band of this semiconductor heterostructures. The photon energy $h\nu$ of this laser process is not dependent on the material band gap. The difference of interband and intersubband transitions is illustrated in Figure 2.8.

In the 90's of the last century two laser concepts were developed that overcame the limitations of conventional interband diode lasers for the emission in the mid-infrared. The lasing intersubband transition was demonstrated first and opens till today the widest infrared range for laser devices. These so called quantum cascade lasers are the focus of this section as well as the employed laser technology for the research of this thesis. But in 1994 Rui Q. Yang proposed a concept of an "interband coupling in leaky quantum wells" [39] between an adjacent quantum well structure. The concept could be demonstrated till today in multiple devices and can be described as a "hybrid of conventional diode lasers and quantum cascade lasers" [12] and was called Interband Cascade Laser (ICL). The function principles will not be explained here. But it should be mentioned that devices could be demonstrated at room temperature in the 2.7 µm to 6.3 µm range [40] and till 11 µm at cryogenic temperatures in pulsed operation [41]. Thus ICLs are also an ideal laser source for MIR gas sensing due to their potential of wide spectral coverage. Generally, ICL possess several advantages compared to quantum cascade lasers as a higher radiative efficiency and lower threshold currents which leads to a much lower power consumption and heat dissipation. ICLs at 7 µm in continuous wave operation at room temperature have not yet been demonstrated, but are prospect of ongoing research. Therefore, ICLs
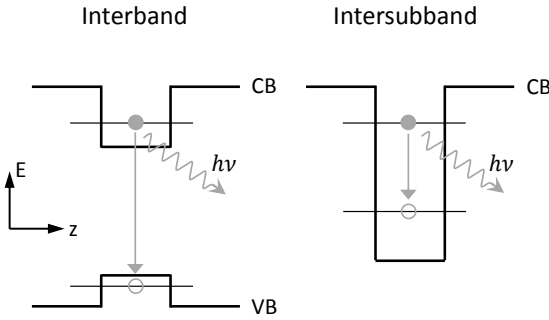
Figure 2.8: Simplified sketch of interband (*left*) and intersubband (*right*) transition in a quantum well of a semiconductor heterostructure. The coordinates indicate the energy axis E and the direction of growth z of the semiconductor layers. The heterojunction of materials with different band gaps leads to a discontinuity of the conduction band (CB) and the valence band (VB) forming a quantum well with confined states. In a diode laser the interband transition of the electron occurs between the confined states of the CB and VB. The intersubband transition in the CB of the quantum well generates the emission in a quantum cascade laser.

are an emerging laser source for gas sensing in the fingerprint wavelengths range.

However, the first experimental demonstration of laser emission by intersubband transitions was realized by J. Faist *et al.* in 1994 [42] in the group of Federico Capasso at Bell Laboratories. Its peculiarity is the unipolar operation that is realized by a pure electron transport through a complex structure of thin semiconductor layers with thicknesses in the order of nanometers called quantum films. In the active region of the laser confined subband levels are formed were the electron transitions occur. The confinement is caused by so called quantum wells and quantum barriers that result from layers of semiconductor material with different band gaps. The Fermi levels at the interfaces align such that both conduction band and valence band form abrupt band edge discontinuities. A quantum well is formed by the smaller band gap material and the quantum barrier results from a larger band gap, cf. Fig. 2.8. The application of an external electric field results in a staircase like regime of the energetic levels of the quantum barriers and quantum wells. This causes a cascading transport of the charge carriers through the device and is the reason for the name Quantum Cascade Laser (QCL).

The intersubband transition level spacing is much closer than the interband level distance leading to the emission of photons with much lower frequencies. The spacing of the radiative transitions are strongly dependent on the thickness of the semiconductor layers while the band offset of the conduction bands between quantum well and barrier determines the accessible energy range for the transitions. Transition energies over a wide range from the mid-infrared until the far-infrared can be attained with the same material system. The III-V semiconductors are predominantly used for QCLs while the heterojunctions of the alloys of indium gallium arsenide/aluminum indium arsenide with indium phosphide as substrate material (InGaAs/AlInAs/InP) yield the best performance for QCL emission in

the MIR fingerprint region [13].

Since their invention the research and development of QCLs passed a strong evolution leading to an enormous variety of concepts of QCL systems with increasingly better performance regarding continuous emission, room temperature operation, output power, beam quality and wavelength tunability [15, 43]. Today, QCLs are a key component of various MIR gas spectroscopy applications. The working principle and most relevant properties of QCLs are explained in the following section.

2.3.1 Principles of Quantum Cascade Lasers

The structure of quantum films in the gain medium of a QCL form periods of two regions that are essential to realize the laser emission: the active region and the injector region. The laser transition occurs in the active region that can be described in its simplest configuration with a 3-level-system of confined subbands. Figure 2.9 displays the plane wave-like energy dispersion of the levels in the reciprocal space with the wave vector $\mathbf{k}_{||}$ parallel to the quantum films. In contrast to the opposite curvature of dispersion for a transition from a conduction band to a valence band in interband transitions of a diode laser, the intersubband transitions of the QCL occur between states with same in-plane curvature of dispersion. This leads to a delta-like joint density of states for the intersubband transitions which results in a narrow transition line width. The emission from such a transition behaves optically like an atomic system having a peak at the transition energy of the subband level difference and revealing an essentially symmetric line that is broadened by different scattering processes. Thus the intersubband system is transparent on the high and low energy side of the transition, which enables to design these lasers to emit very broad band.

The optical transition of the three level system in Figure 2.9 takes place from the highest level E_3 to the next lower level E_2. During laser operation electrons are injected into the upper level E_3 from the adjoining injector region. After transition the lower level E_2 is emptied by fast scattering of the electrons leading to a transition to level E_1 and tunneling of the electrons into the next injector region. But realizing laser operation especially requires an inversion of the state population. In consequence a longer state lifetime of electrons in the upper level than in the lower level is a mandatory condition.

The population inversion is not an intrinsic property of the material but can be realized by application of an electric field and the subsequent charge carrier transport. This requires a precise manipulation of the scattering and relaxation processes of the electrons between the subband levels. The succession of quantum wells and barriers, their respective thicknesses and specific doping levels of the layers allow to tailor the level spacing, the band structure and thereby the different scattering processes in the QCL. Non-radiative scattering processes are the interaction of electrons with longitudinal-optical phonons, acoustic phonons and electrons. The dominating scattering process is the interaction of the electrons with the longitudinal-optical (LO) phonons of the semiconductor crystal reducing the subband state lifetimes to the order of picoseconds. This is much shorter than the lifetime of the electrons for recombination into the valence band which are in the
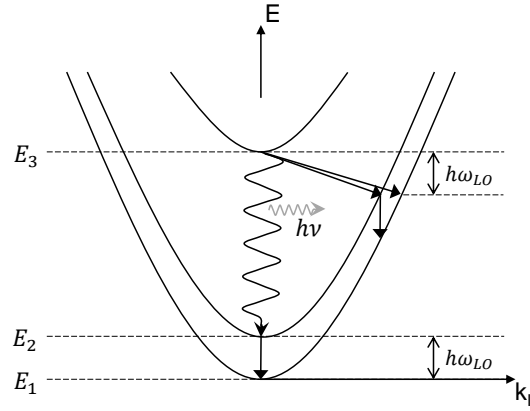
Figure 2.9: Schematic depiction of the dispersion of subband energies in active region as function of the wave vector $\mathbf{k}_{||}$. The radiative laser transition 3-2 is indicated by the curled arrow and an emitted photon $h\nu$. Non-radiating transitions 3-2, 3-1 and 2-1 due to LO phonon scattering/emission ($\hbar\omega_{LO}$) are depicted by straight arrows [44].

nanosecond range. A LO phonon with the energy $\hbar\omega_{LO}$ is emitted by the transition. The dispersion relation of the LO phonons in the semiconductor crystal is relatively flat and non-zero for a phonon wave vector $\mathbf{q}$ near 0. The lifetime τ of an intersubband state is proportional to the wave vector of the emitted phonon $\mathbf{q}$ in a scattering process. Thus with decreasing subband level spacing the state lifetime decreases, becoming minimum for an energy difference $E_i - E_f = \hbar\omega_{LO}$ of the transition and a near-zero momentum transfer at the bottom of the dispersion curve, cf. $E_2 \to E_1$ Fig. 2.9.

In the case of the three level system illustrated in Figure 2.9, the transition energy between the upper and the subjacent state is $E_{32} \gg \hbar\omega_{LO}$ while the transition between the two lower states is in "resonance" with the LO phonon energy $E_{21} \approx \hbar\omega_{LO}$. Thus, a non-radiative transfer by LO phonon scattering between the states 3-2 and 3-1 can only occur with an accompanying relatively large momentum transfer where the state lifetime τ is proportional to the transferred momentum. The dispersions of the two lower subbands 2 and 1 are parallel (neglecting non-parabolicity effects). This assumption leads to strict phonon resonance resulting in fast scattering of the electrons due to the vanishing momentum transfer and therefore facilitating arbitrarily small state lifetimes. This yields a much higher lifetime τ_{32} of the electrons for the 3-2 transition than the lifetime τ_{21} for the transition between the lower levels 2-1 and effectively causes inversion of the population. Several concepts have been developed to further increase the upper state lifetime. Details on the respective active region design can be found in the literature [42, 45].

Beside the fast LO phonon scattering effective tunneling of the electrons from the lowest level of the active region through the injector region and into the excited level of the subsequent active region has to be realized. The applied electric field aligns the levels of the injector region with the adjacent levels of the active regions to facilitate this process.
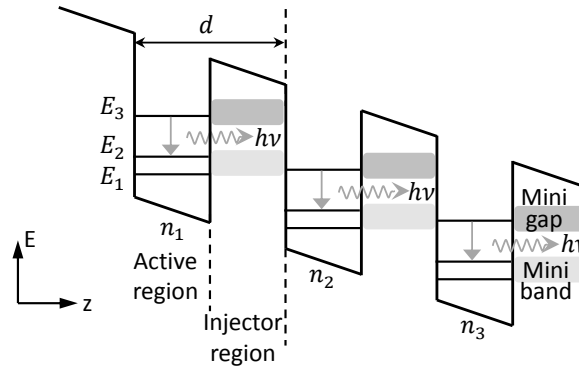
Figure 2.10: Simplified schematic band structure that neglects the multiple layers in the active and injector region but illustrates the basic principle of operation of a QCL. The junction of active region and injector region build a period d of the structure. In each active region n_i a laser transition occurs by generating a photon with the energy $h\nu$. The applied external voltage leads to the staircase of the region subband levels that enables the cascading transport of the electrons through the quantum film structure.

In addition layer thicknesses and doping in the injector can be adjusted to form so called 'minibands' and 'minigaps'. The minibands are aligned with the lower states of the previous active region to realize effective tunneling and injection into the excited level of the subsequent active region. The minigaps hamper electrons in the upper level of the active region to tunnel into the injector region. Figure 2.10 illustrates the staircase of conduction band level energies that are formed when an external field is applied.

The non-radiative scattering processes are very effective to depopulate the subband levels which means stacking periods of active and injector region is essential to realize lasing of the structure. However, this stacking is also a big advantage as theoretically an arbitrary number of active and injector regions are stackable into an active region which highly increases the photon gain of a single electron and increases the laser's output power. But a higher number of stacks requires to apply a stronger electric fields to obtain a cascading electron transport. The aim of realizing low power consuming devices often leads to a compromise between applied current and voltage and therewith the number of periods in the QCL.

The emitted laser radiation is generally linearly TM-polarized with an electric field vector parallel to the growth direction z of the quantum layers [45].

The first QCLs have been so called Fabry-Pérot lasers that emitted laser radiation in multiple equidistant modes that were determined by the width of the material gain, the device temperature, the gain losses in the waveguide and especially by the reflectivity of the laser facets. Single mode selection was realized with the development of distributed feedback (DFB) QCLs [46, 47]. By incorporating a grating structure into the QCL cavity a periodic modulation of the waveguide effective index is created that modifies the internal

losses and yields a single mode emitting device. DFB QCLs reached maturity over the years and are nowadays commercially available and broadly used. However, the wavelength tuning range of DFB QCLs is typically in the range of 1-5 cm^{-1} depending on the central wavelength and therefore rather suitable for single gas species measurements. Among other approaches, less prevalent techniques as coupled cavity QCLs can realize broader tuning ranges but these approaches may also imply other requirements as for example wide range temperature tuning for broad tunability [48].

In general, realizing broad wavelength tunability requires two properties: a broad and ideally flat gain width of the device and a wavelength selective element that allows for a wide tuning range. Broad gain width QCLs have been accomplished with essentially two different concepts. Either active regions are created with multiple radiating transitions from an upper level and a band of multiple lower levels called bound-to-continuum design [49] or heterogeneous active regions were built with two or even more substacks on top of each other in one device emitting at different wavelength ranges [50–52]. The wavelength tuning can be performed with the application of an external-cavity (EC). Quantum cascade lasers with an EC configuration were demonstrated in various arrangements taking advantage of the full gain spectrum of the QCL. As wavelength selective element usually a reflective diffraction grating is employed which allows for controlled narrow band feedback into the QCL chip to enable a spectrally single mode laser.

Comprehensive reports have been published covering designs for broad gain QCLs [53–55], also with various other concepts that should not be listed here. Also the investigated configurations for external-cavity arrangements include a large number of approaches. However, some major concepts have prevailed and found their way into the market of commercial MIR laser sources.

For the measurement system that was developed for multi-species gas sensing a commercial external-cavity quantum cascade laser (EC-QCL) system was employed to acquire the spectra of the targeted gas mixtures. The basic principles of operation are important to understand the device behavior and manipulate the laser emission to obtain high spectral resolution. Hence, the main principles of EC-QCLs and the consequences for the emission wavelength will be briefly summarized in the following.

2.3.2   External-Cavity Quantum Cascade Lasers

The first demonstration of external-cavity quantum cascade lasers (EC-QCL) was accomplished nearly two decades ago by Luo *et al.* with cryogenically cooled and in pulse mode operated QCL chips [56, 57]. Since then EC-QCLs have continuously been improved regarding their wavelength tuning range, continuous wave operation at room temperatures and tuning speed, in order to mention some major development aspects. Directly after their first demonstration they attracted high interest for gas sensing applications due to their broad wavelength tuning range and the general possibility to achieve high resolution measurements [58]. Although EC-QCLs combine several advantages for MIR gas sensing, their technical realization remains challenging due to shock sensitive opto-mechanical components preventing their application in harsh environments. Furthermore, taking
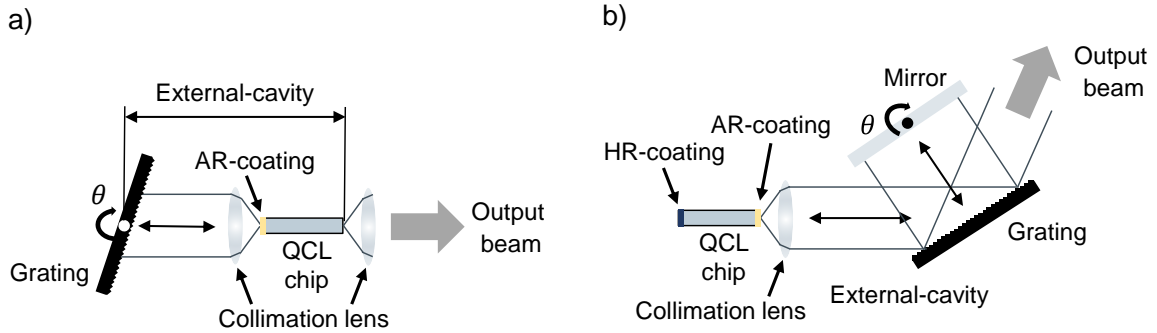
Figure 2.11: a) Littrow external-cavity (EC) configuration with two collimation lenses to guide the divergent emission from the QCL facet as collimated beam either to the wavelength selecting reflective diffraction grating of the external cavity or as output beam from the QCL. The anti-reflection (AR) coating is mandatory to realize tuning between the external cavity modes which are set by the distance between the grating and the output facet of the QCL chip. b) Littman-Metcalf EC configuration with an extra mirror that is rotated for wavelength selection. The cavity is formed by the mirror and a high-reflection (HR) coating at the back facet of the QCL chip. The double pass through the grating results in stronger wavelength selectivity but also lower feedback power into the QCL chip.

advantage of the full gain width by a gapless tuning of the emission cannot be realized with the basic external-cavity configurations, cf. Fig. 2.11, but requires more sophisticated systems that in turn increase complexity, susceptibility to mechanical disturbances and cost. This section is intended to illustrate the general setup of EC-QCLs and some major principles of mode selection and wavelength tuning. The outlined tuning behavior of EC-QCLs could be exploited in the developed measurement system and turned out to be crucial for realizing high resolution gas absorption spectroscopy.

The main elements of an EC laser system are the gain element, which is the QCL chip, the collimating lens and the grating which acts as a wavelength selective filter within the system. In Figure 2.11 sketches of the two most commonly employed EC designs are depicted. The external-cavity is formed by a reflective diffraction grating (Littrow) or a grating in combination with a reflecting mirror (Littman-Metcalf). Rotation of the grating (mirror) induces a strongly wavelength dependent loss to the resonator resulting in low loss in a narrow freely positionable band and very high loss everywhere else. In the Littrow configuration the first diffraction order of the grating is reflected back into the QCL chip while the beam is coupled out of the opposite facet of the QCL chip. For the Littman-Metcalf configuration the first order diffraction is dispersed from a static grating to an angle-tunable mirror that reverses the beam path and couples the laser emission into the QCL after a second grating diffraction. The zeroth order is employed as output beam in this second configuration, cf. Fig. 2.11 b) [59].

The wavelength selection λ_G by the grating is given by the Bragg reflection condition

that dependends on the grating's groove spacing d and the rotation angle θ_G that is the angle between the incoming beam and the grating normal:

$$\lambda_G = 2d \sin\theta_G \ . \tag{2.29}$$

In commercially available EC-QCLs the Littrow design dominates due to its lower complexity and the stronger feedback into the laser allowing to access a broader gain range for tuning. The employed laser system for the gas measurements is also based on EC-QCLs with a Littrow design, cf. Section 4.2. Accordingly, tuning properties and mode selection for this EC-QCL configuration will be described in the following.

The basic configuration of a cleaved QCL chip is a Fabry Pérot (FP) cavity where the reflectivity of the facets determines the feedback into the active medium of the chip. The wavelength with highest net-gain and lowest gain-losses in combination with the respective reflectivities of the cavity facets determines the amplified mode, cf. Eq. 2.32. In the case of a broad flat gain and a wavelength independent constant reflectivity several equidistant modes are amplified. The mode spacing is given by

$$f_{FP} = \frac{c}{2n_{eff}l} \tag{2.30}$$

with c the vacuum speed of light, an effective index n_{eff} that describes the modal phase propagation in the waveguide of the QCL and l the chip length. A FP cavity of typically 1-3 mm length leads to a frequency spacing f_{FP} of the modes in the range of 1 cm^{-1}. The amplified modes can be altered by changing the laser current or temperature of the device as the current affects the lasing threshold and the temperature the effective index of the gain material.

The combination of a FP QCL chip with an EC causes a wavelength dependent feedback that alters the wavelength losses in the gain medium. The rotation angle θ_G of the grating determines the reflected grating mode f_G. Due to the superposition of the facet reflections and the grating reflection the FP mode f_{FP} that is closest to the grating mode f_G receives the strongest feedback and will therefore be selected as the dominant mode in the lasing process while the other FP modes are suppressed. Hence, single mode emission is received and tuning of the emission wavelength can be obtained by selecting the FP modes of the QCL chip by rotation of the external grating. But the chip facet reflections limit the wavelength selection to tuning between the relatively widely spaced FP modes. The rotation of the grating causes an abrupt change of the emitted mode and wavelength known as "mode-hopping".

The EC, that is formed by the grating and the opposite QCL facet, cf. Fig. 2.11 a), sets its own mode spacing f_{EC} depending on the EC length L.

$$f_{EC} = \frac{c}{2(n_{eff}l + L)} \tag{2.31}$$
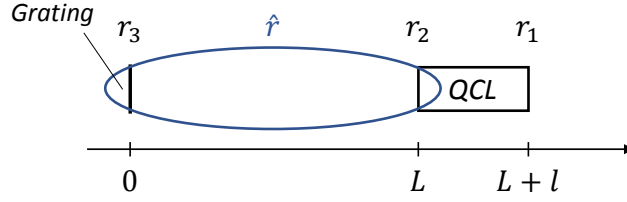
Figure 2.12: Schematic representation of a coupled cavity to illustrate the variables of the overall loss calculation, cf. Eq. 2.32.

Due to an EC length L that is typically $L \gg l$, much smaller mode spacing f_{EC} can be obtained. Thus by adding an anti-reflection (AR) coating to the QCL facet that faces the EC suppression of the FP reflection can be realized yielding a feedback into the cavity that is dominated by the grating reflection. A perfect AR coating that entirely removes the facet reflection would allow tuning between the narrowly spaced EC modes by rotation of the grating.

Wide range AR coatings are difficult to fabricate in the MIR. Therefore, it is hardly achievable to receive an entire suppression of the FP reflections which means that in most cases an EC-QCL has to be considered as coupled-cavity of the chip cavity and the EC. Figure 2.12 shows a simple sketch of this coupled cavity with the respective reflecting faces r_i and the lengths L and l that determine the mode spacing [45].

As already mentioned before lasing will first occur in the mode with the highest net-gain, lowest gain-losses and favorable reflectivity, especially dependent on the EC grating angle. In the case of a broad and constant gain the mode selection dependence is reduced to the loss function. Their different components are given by the losses in the QCL waveguide α_ω and the feedback losses from the different surfaces that are determined by the reflection coefficients r_i. Equation 2.32 describes the overall losses $\bar{\alpha}(f, f_G)$ over the frequency range f and for the grating angle dependent mode f_G:

$$\bar{\alpha}(f, f_G) = \frac{\alpha(f, f_G)}{\Gamma} = \frac{1}{\Gamma} \left(\alpha_\omega + \frac{1}{l} \ln \left| \frac{1}{r_1 \hat{r}(f, f_G)} \right| \right) \ . \tag{2.32}$$

In the equation Γ represents the confinement factor that is the ratio of the light intensity within the active layer and the overall intensity [59]. The course of the function is dependent on the product of the wavelength dependent amplitude reflection coefficients r_i. In the equation r_1 is the reflection from the QCL output facet and the factor $\hat{r}(f, f_G)$ depends on the residual reflection r_2 of the AR coated facet and the grating reflection r_3. Hence, the mode f_i, either given by the EC modes or the FP modes, that is closest to the minimum value of the overall losses $\bar{\alpha}$ will receive the highest amplification while the other modes are suppressed. Whether the tuning by the grating rotation is realized between the densely spaced EC modes or the FP modes depends on whether r_2 or r_3 dominates $\hat{r}$ at the respective grating angle and wavelength position.

But even when the reflection r_2 can be neglected and therefore all EC modes are

accessible, a continuous tuning over the gain region cannot be attained when the EC length L is fixed. EC-QCL configurations were presented that allowed for adapting the EC length during rotation of the grating by choosing a displaced center of rotation (pivot point) which results in an EC length $L(\theta)$ and allows mode-hop free (MHF) tuning over specific gain ranges [60]. Alternatively, a further fine tuning of the grating position with a piezo-actuated stage can be realized that allows for a larger freedom of adapting EC length and grating angle simultaneously and also leading to MHF tuning for small wavenumber ranges [61, 62].

However, these setup configurations are sophisticated and imply delicate handling during operation. Also the laser system, that was employed for the development of the measurement system that will be covered in the following chapters, is built of EC-QCLs with fixed EC length. Thus it shows a mode hopping behavior as described before. Nonetheless, high resolution spectra could be measured with the employed EC-QCL and the developed measurement system.

In an early publication Peng *et al.* [63] proposed fine tuning of a pulsed EC-QCL with imperfect AR coating by shifting the Fabry-Pérot longitudinal mode to coincide with the desired grating-selected wavelength. As phase tuning mechanism the QCL chip temperature was used. The effective index n_{eff} of the QCL chip changes due to temperature variation which leads to a phase shift of the FP modes. By rotation of the grating coarse wide tuning was demonstrated while changing the chip temperature served for intra-cavity phase control to fine-tune over narrow ranges between adjacent longitudinal modes. The laser was operated at 230 K and a temperature change of approx. 21 K was required to shift one full FP mode spacing. Therefore, also for an EC-QCL having a fixed cavity length fine tuning can be accomplished but implies to deal with long measurement times as temperature tuning is inherently slow.

Chapter 3

Laboratory system for multi-species hydrocarbon gas sensing

For the realization of multi-component measurements of alkanes (C_1 - C_5) a new laboratory environment was planned and built up from scratch. The preliminary considerations aimed at allowing for a maximum of freedom for the supply and composition of the gases to measure (not limited to the investigated hydrocarbons). Also a wide range of measurement conditions for the spectroscopic sensing should be ensured. The latter will be examined in detail in Chapter 4 as it refers to the realization of the spectroscopic measurements. The accurate supply of the gases is an indispensable precondition to ensure the correct assignment of the acquired spectral data to quantitative values of the mole fraction of a gas species in a multi-species mixture.

In this chapter the assumptions that were taken to plan the laboratory measurement system will be highlighted in Section 3.1. Subsequently, the developed system for the supply of the hydrocarbon gases, cf. Section 3.2, will be illustrated and a brief overview of the necessary setup automation, cf. Section 3.3, for the later measurements will be given.

3.1 Requirements of the laboratory concept

The presented system was planned to enable spectroscopic measurements of the first seven alkanes (C_1 - C_5) as of their arbitrary mixtures[1].

In Figure 3.1 a schematic depiction of the laboratory environment is given. One aspect of the system design has been safety requirements. The investigated hydrocarbons are flammable gases which can form explosive mixtures when they exceed a respective concentration limit in air, e.g. lower flammability limit of propane: 2.1 % [65]. Hence, potential gas leaks have to be avoided or the possible gas flow constrained to omit the formation of explosive concentrations.

The gases are stored in a separate gas cabinet with a venting system to ensure that no

---

[1]The International Union of Pure and Applied Chemistry (IUPAC) recommends the following names for the individual gases [64]: methane, ethane, propane, butane, 2-methylpropane (isobutane), pentane, 2-methylbutane (isopentane). Even though the use of the names isbutane and isopentane for the C_4 and C_5 isomers is no longer recommended they will be used within this thesis as they simplify the relation of the gas species name to the unbranched isomer.
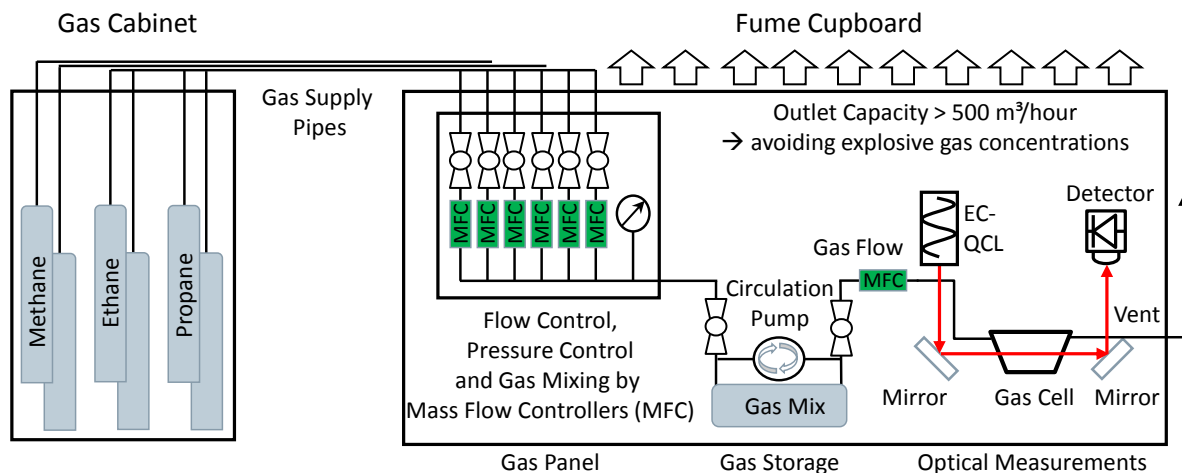
Figure 3.1: Scheme of the Laboratory Environment. Components: gas cabinet with stored pure gas bottles, fume cupboard with gas panel for gas supply and mixing, intermediate storage for self-prepared gas mixtures and optical setup for spectroscopic measurements. The system was designed to ensure safe operating conditions when using potentially hazardous gases like the hydrocarbons.

explosive concentration occurs in the bottle storage. Through a metal pipe each gas is transported to a fume cupboard. A flow limiting valve and a ball valve control the supply and keep the transport rate below the outlet capacity of the fume cupboard. Thus, in case of a gas leak no explosive concentration can occur. A self-developed gas panel with a mass flow controller for each gas, cf. Section 3.2, serves for sampling and mixing of the gases. The gases can be either directly transported to the optical setup or to a storage volume for mixture preparation. All gas-carrying components were helium leak tested to ensure safety and avoid impurity due to leakage. Therefore, safe measurement conditions are guaranteed.

The spectroscopic measurement system with its components for the signal acquisition and setup control are also set inside of the fume cupboard, cf. Fig. 3.1. Main focus of the measurement system development was to realize a maximum of accuracy and precision of the measurements. This concerns the accuracy of the supplied gas sample mole fractions as well as of the spectroscopic measurements.

In order to ensure an accurate gas-mixture preparation of the hydrocarbons the real gas behavior of the gases must be considered. In the following section the relevant physical properties of the seven alkanes, the developed gas mixing unit and the realization of multi-component mixtures for the spectroscopic measurements will be described. The spectroscopic setup is subject of the following Chapter 4.

3.2 Hydrocarbon gas sampling and mixing

The quantitative determination of the molar fractions in a mixture of several gases with tunable laser absorption spectroscopy assumes that:

- the species' molar fractions in the gas sample are accurately determined,

- the spectral data of each pure component at the measurement conditions are available,

- the physical parameters during the measurements (temperature, pressure, path length) are known and stable

- the influence of gas species interaction on the shape of the spectra can be predicted and ideally corrected in the measurement data analysis.

The latter points relate to the spectroscopic measurements which will be discussed in the other Chapters 4-6. But the first point is the prerequisite that accurate spectral data can be acquired. For the investigations three different gas sample configurations were required:

- high-purity single species gas samples,

- self-prepared gas mixtures (binary, ternary, multi-species) with low uncertainties and

- highly accurate gravimetrically prepared gas mixtures.

In the following a brief explanation will be given how the real gas properties influence the preparation of gas mixtures. The technical system that was planed and built to ensure a proper gas supply to the spectral measurements will be explained. Finally, the preparation method and accuracies that can be expected for the preparation of a binary mixture are outlined.

3.2.1 Real gas properties

The correlation of the physical properties of a gas, meaning the gas pressure p, the gas temperature T and the volume V, is given by a so called equation of state (EOS):

$$f(p, V, T) = 0 \tag{3.1}$$

The theoretical model of an ideal gas assumes that the gas molecules are point particles which only interact with each other by elastic collisions. The ideal gas law thus defines the product of the gas pressure and volume to be linearly dependent on the gas temperature:

$$pV = nRT \implies f(p, V, T) = pV - nRT = 0 \tag{3.2}$$

with n the number of moles of the gas and R the molar ideal gas constant. This model fails for wide ranges of temperature and pressure due to non-consideration of phase changes

Table 3.1: Compressibility factor Z of C_1 - C_4 alkanes at one atmosphere and 298 K.

Gas species	Compressibility factor Z
Methane	0.9983
Ethane	0.9924
Propane	0.9785
Butane	0.9699
Isobutane	0.9735

as well as the properties of extended molecules that deviates from point particles. These deviations reveal the real gas properties of the respective species which can be described by a compressibility factor Z.

$$Z = \frac{p}{RT\rho} = A + B\rho + C\rho^2 + D\rho^3 + ... \tag{3.3}$$

In the case of an ideal gas $Z = 1$. But as real gases differ from this model, the compressibility factor Z of a gas or fluid is normally unequal one and can be expressed in the virial expansion of the temperature dependent virial coefficients of the respective substance A, B, C, D ... as stated in Equation 3.3 with ρ being the molar density.

While the behavior of methane is comparable to an ideal gas, the deviations increase for the larger alkanes [66, 67] and thus have to be considered in the mixture preparation. First the molar fraction does not scale linearly with the partial pressure of the gas and second phase change at elevated pressure by liquefaction of the heavier hydrocarbons has to be avoided. Also the mutual interaction parameters of the gas components should be considered when an accurate gas mixture has to be prepared. For illustrating the deviations of Z from ideal gas behavior Table 3.1 shows the compressibility factors for the C_1 - C_4 alkanes at 1 atmosphere pressure and 298 K. It has to be mentioned that the pentanes are liquid at ambient conditions [68].

Obviously, the compressibility increases with the size of the gas molecules. For the pentanes at ambient temperatures reduced pressure is required to obtain the gas phase. Consequently, the deviation of their Z values is the largest of the considered gases.

For the calculation of the properties of hydrocarbon gases an adapted semi-empirical Equation 3.4 of state was developed by Peng and Robinson [69] which constitutes a further development of the van der Waals equation of state.

$$p = \frac{RT}{V_m - b} - \frac{a\alpha}{V_m^2 + 2bV_m - b^2} \tag{3.4}$$

Table 3.2: Exemplary mixture illustrating the mole fraction of each component and the partial pressure of the respective species in an ideal gas mixture compared to the pressure values in a real gas mixture at 295 K and 4 bar total pressure of the mixture. The mole fractions of the gases correspond to actual process stream values in a refinery gas sample.

Gas species	Mole fraction [%]	Ideal gas [mbar]	Real gas [mbar]	Pressure difference [mbar]
Methane	0.3	12.0	12.4	0.4
Ethane	4.0	160.0	156.2	-3.8
Propane	49.7	1988.0	1921.2	-66.8
Butane	22.0	880.0	887.7	7.7
Isobutane	22.0	880.0	934.9	54.9
Pentane	0.6	24.0	26.3	2.3
Isopentane	1.4	56.0	61.2	5.2

Common for these types of EOS are the parameters molar volume V_m and the substance-specific constants a and b as attraction and repulsion parameter, respectively, that depend on the critical properties of the substance. The parameters α is of empirical nature but relies on the acentric factor of the species and scales with the reduced temperature of the substance which is the actual temperature of the gas divided by its critical temperature.

The calculation of accurate gas mixtures therefore requires the availability of multiple species-specific parameters. Hence, for the preparation of gas mixtures the pressure value of each species was calculated with the Peng-Robinson EOS. For the respective simulations and hydrocarbon-specific parameters the commercial simulation software AspenPlus [70, 71] from AspenTech was employed[2].

Table 3.2 shows an example mixture with a total pressure of 4 bar which was the target pressure for mixture preparation. The partial pressure of the gases in the mixture are given when calculated with the ideal gas law and compared to the values that are obtained with the Peng-Robinson EOS and the real gas parameters.

3.2.2 The gas mixing unit

In order to allow for a maximum flexibility for the supply of the measured gases a gas mixing system was developed to measure either pure gases, self-prepared gas mixtures or manufacturer pre-mixed test gas mixtures. A sketch of the built system with the main components of the gas mixing panel is shown in Figure 3.2.

First the gases from the gas storage are led over individual mass flow controllers (MFCs)

---

[2] The calculations of the real gas mixtures were performed by Dr. Frank Olschewski.
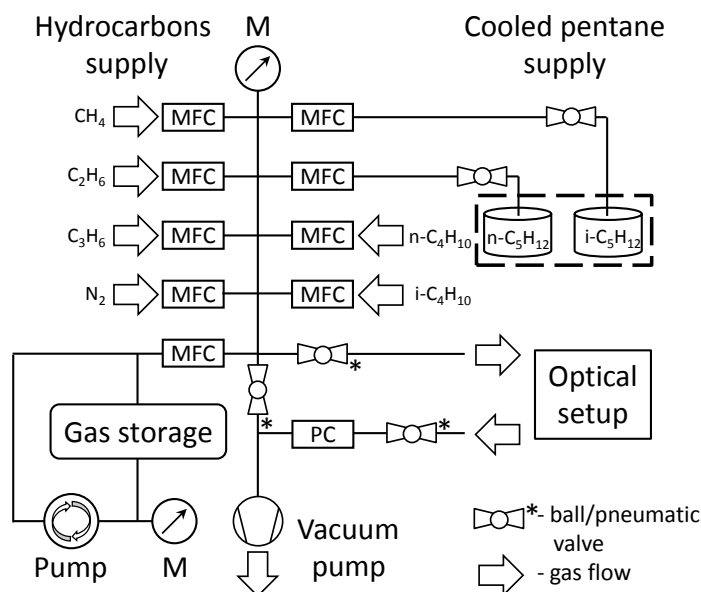
Figure 3.2: Sketch of gas mixing unit: *MFC*: mass flow controller, *M*: manometer, *PC*: pressure controller. Each gas is supplied through an individual MFC while the pentanes are evaporated from separate cooled glass vessels.

into a compact tubing system that was designed to have a minimum dead volume. The mass flow controller either allows to shut the gas flow or open the gas path entirely. In standard operation the gas flow is adjusted to a fixed setpoint which is measured and controlled with an implemented calorimetric sensor. Pneumatic valves can be switched to select the gas path either to the optical measurement setup or to the venting vacuum pump. Additionally, a MFC controls the gas tubing to an intermediate gas storage of 1 l volume. By setting the MFC valve to open position the gases can flow in reverse direction through the MFC into the storage cylinder. The cylinder is connected with a circulatory tubing system and a diaphragm pump that is used to homogenize the content of the storage cylinder. Then the inlet MFC is closed. The homogenization or mixing is necessary when several gases were fed subsequently into the storage before. Without mixing a layering of the components occurs. The procedure to realize self-prepared gas mixtures is explained in the following in Section 3.2.3. Beside the hydrocarbons another MFC supplies dried nitrogen to the system for either purging or allowing to dilute a mixture with a non-absorbing gas. Two highly precise digital manometers[3], one in the tubing system for the gas supply and one in the gas storage cylinder, measure the gas pressure in a range from 0 to 10 bar. Accurate and precise pressure measurements are required at multiple points to ensure minimum uncertainties for the gas mixture preparation and to guarantee constant pressure during the spectroscopic measurements.

---

[3] Keller LEX 1, Precision: ≤ 0.01 % full scale, Accuracy: ≤ 0.05 % full scale

Further attention had to be put on the supply of the pure pentanes. Normal- and isopentane are liquid under ambient conditions with a respective vapour pressure of 685.3 mbar and 918.5 mbar [72]. Thus, feeding the optical setup or the gas storage with pentane gas requires an extra supply. Therefore, each pentane was filled in a separate laboratory glass pressure vessel that was put in a water bath for cooling the pentanes to 17° C. By evacuation of the tubing system the pentane can be effectively evaporated. The cooling of the pentane source ensures that no saturation and thus phase change occurs somewhere in the system as it would either lead to an undefined concentration in a gas mixture or potentially damage the MFCs. A high precision pressure controller behind the optical setup controls the gas pressure for the spectroscopic measurements. An oil-free scroll vacuum pump is used for evacuating the whole system until a theoretically ultimate pressure of 0.01 mbar.

3.2.3 Realization and accuracy of single gas supply to multi-component mixtures

The purity of the single gases that were supplied was either ≥ 99.95 % for the C_1 - C_4 or ≥ 99.5 % for the C_5 alkanes. Pure gases were measured by first evacuating the gas system to a pressure below 0.5 mbar. The respective MFC was set to a constant flow of on average 20 ml/min and the gas was transported through the tubing system to the optical setup. The pressure controller was set to 50 mbar for the majority of the measurements while the vacuum pump maintained a constant low pressure at the outlet of the setup. After passing the spectroscopic measurement the constantly flowing gases are diluted into the vent of the fume cupboard.

The simultaneous measurement of the mole fractions of several gases in a gas flow was the final target of the investigations. Consequently, gas mixtures have to be prepared or supplied directly from test gas bottles. In the first case the gas mixing unit was employed. In the following the mixing procedure and the expectable accuracies will be delineated.

For the preparation of a gas mixture the gas sample cylinder and the tubing system was evacuated first. The sequence of constituents to be injected is determined by the respective vapor pressure of the gases. The gas with the lowest vapor pressure will be injected first and the other components with increasing vapor pressure are added subsequently. The filling pressure or partial pressure, respectively, of each constituent was calculated by solving the Peng-Robinson equation of state with the AspenPlus software as outlined in Section 3.2.1. The target pressure in the sample volume must be built up reasonably slow to maintain nearly isothermal conditions. The pressure in the sample volume is monitored with the manometer connected to the gas storage cylinder. As soon as the required pressure has been reached the MFC valve is closed. Due to thermalization the pressure in the sample volume can still vary after the MFC valve was closed. When a stable pressure is reached after 10 to 40 seconds further gas is either injected if the pressure was to low or the tubing system outside the gas storage is evacuated when the target pressure is reached within a margin of 0.5 mbar. The pressure in the sample cylinder is noted before the next constituent

is added. Before adding the next component the tubing system is filled with it slightly above the sample cylinder pressure to avoid a back flowing of gas when the MFC to the gas storage is opened. Then the next constituent is filled into the sample cylinder to the required pressure. Again the MFC is closed and the stabilization of the storage pressure awaited. Either further gas is added if the required pressure was not reached or the system is re-evacuated and the filling procedure repeated for the next constituent. Finally, the mixture of the gases has to be homogenized. Therefore, the diaphragm pump circulates the gas mixtures in the sample cylinder for about 30 minutes. Tests revealed that this circulation time was sufficient to effectively avoid layering of the gas components.

The final pressure of the mixture is limited by the closing limit of the MFC of 5 bar pressure difference between its inlet and outlet. Furthermore, depending on the composition of the mixture phase change of the individual components has to be prevented. Especially for the C_4 - C_5 alkanes the overall pressure has to be adapted according to their partial mole fraction in the mixture as their vapor pressures range from 0.69 bar to 3.51 bar at 298 K.

The described procedure allows for a large freedom of gas mixture preparation. But the limited accuracy of the pressure and temperature measurements also set limits to the achievable accuracies of the mole fractions of gases in a mixture. Therefore, a rough estimation of uncertainties in the mixture preparation will be given in the following.

Several uncertainty factors for the preparation of mixtures with highly precise mole fractions can be identified: error in pressure and temperature measurement, inaccuracies of the compressibility factors that depend on the temperature, pressure and composition of the gases in a mixture, the phase behavior of the gases to be mixed and generally the number and mole fraction of the components. To illustrate these influences the expectable uncertainties for just a binary mixture with hypothetical ideal gas behavior shall be calculated.

As stated in Table 3.1 the compressibility factors of methane and ethane only slightly deviate from an ideal gas at ambient conditions. Thus, Equation 3.2 can be applied assuming that the partial pressure of a component p_i is the product of its mole fraction χ_i and the pressure p of the gas mixture with all components injected.

$$p_i = \chi_i p \qquad (3.5)$$

According to Equation 3.2 the pressure of the gas p is dependent on its volume V and its temperature T. The volume of the gas sample cylinder is constant but the temperature may deviate as it is not stabilized. Taking temperature variations into account it follows for the mole fraction of the first component χ_1 in a binary mixture:

$$\chi_1 = \frac{p_1 \cdot T}{p \cdot T_1} \qquad (3.6)$$

As the sum of the mole fractions χ_1 and χ_2 must equal to 1 it follows that $\Delta\chi_1 = -\Delta\chi_2$ for the deviations of the mole fractions. In this simple model neglecting gas compressibilities

and their dependence on temperature, pressure and mole fractions of the components, uncertainties arise from errors in the pressure and temperature measurement. The manometer that monitors the gas volume pressure has an accuracy of the measured value of $\pm$ 5 mbar and a Pt-100 resistor thermometer measures the temperature in the pipe system close to the sample volume with an accuracy of ± 0.2 K. Due to the fact that the temperature measurement probe is not directly immersed into the gas volume cylinder and temperature variations occur due to ambient temperature changes the error of the measured temperature is assumed to vary in a range from 0.2 to 0.5 K.

With the propagation of uncertainty the maximum error Δx_1 of the mole fraction with the stated errors in pressure and temperature can be calculated. For a binary mixture with 1 bar pressure p and 500 mbar partial pressure for each components a relative error $\Delta \chi_1 / \chi_1$ of 0.85 % to 2.13 % is calculated.

This illustrates that the preparation of exact gas mixtures is difficult to achieve especially when the number of components increases and higher filling pressures are targeted. Also the error of the measured pressure value clarifies that the method is limited when mole fractions in the per mille range have to be realized in a mixture. Therefore, in the later measurements only binary and ternary mixtures have been prepared with the gas mixing setup in order to prevent large errors of the respective mole fractions. For the measurements of complex mixtures with all seven alkanes manufacturer pre-mixed and calibrated mixtures from an external supplier were employed. These mixtures were prepared with a gravimetric method that implies highly precise weighing of the gases that are filled into a test gas bottle. This preparation procedure guarantees to constrain the relative uncertainties to a range of 0.1 % to 2 % dependent on the respective mole fraction of the component.

3.3   Setup automation

The automation of the individual parts of the measurement system is of high importance to enable detailed measurements, especially for long-term spectroscopic measurements as will be illustrated later, cf. Chapter 5. The software for the computer control of the setup is based on the development environment LabVIEW from National Instruments. A brief overview of the developed graphical user interfaces and operation modes can be found in Appendix A. Here, the main functions for the measurement procedure are summarized.

The setup operation and measurement data acquisition is fully computer controlled. A graphical user interface (GUI) was developed to manipulate the gas mixing and supply unit. The GUI functions set the various analog and digital outputs and inputs that control the operation of the MFC, valves and pumps of the gas unit. For illustration Figure 3.4 shows a screenshot of the program. A self-designed breakout box with a signal board with the respective slots for the device connectors was built to transmit and acquire the signals for setup operation.

As illustrated in Figure 3.3 the main functions of the setup automation is the manual control of the gas supply by setting all parameters via the GUI. This also includes the automated gas mixture preparation which is realized corresponding to the procedure
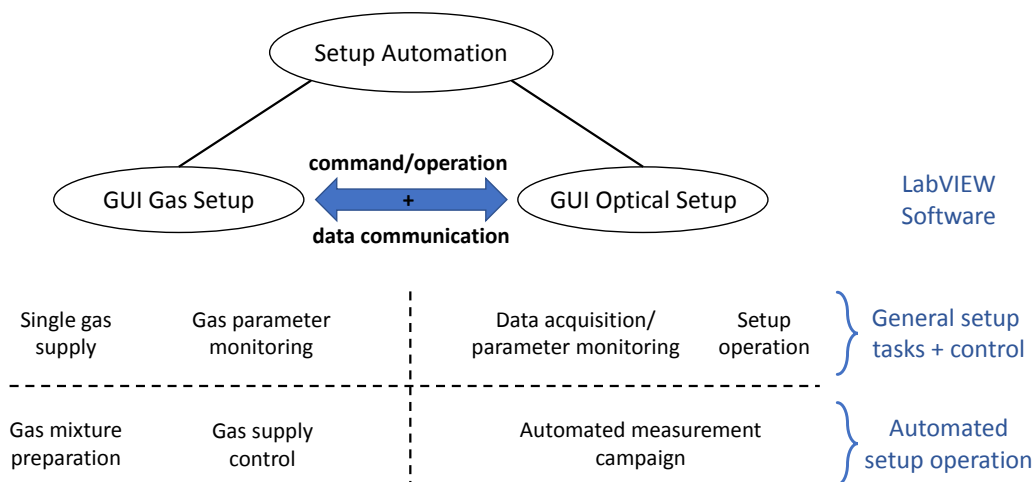
Figure 3.3: Breakdown of most important functionalities of the setup automation with two self-programmed LabVIEW graphical user interfaces. The program for the gas setup allows for manual control of the gas supply and monitors the respective parameters from gas flow till gas pressure. The gas mixture preparation and the supply during measurement campaigns can be automated. Similarly, the optical setup, cf. Chapter 4.1, allows for manual operation, parameter monitoring and data acquisition. In case of an automated measurement campaign it controls the commands for the operation of both GUIs.

described in Section 3.2.3. Gas parameters as the pressure at different points in the setup are acquired and can be saved to file if required. The supply of different gases to the spectroscopic measurement can either be set manually or is automated during long-term measurements. In this mode of operation the control GUI for the optical setup initiates the operation of the gas supply which changes between states of evacuation and gas supply according to the respective measurement protocol. Thus, an exchange of commands, operation state query and measurement data transfer is implemented for this modus operandi of the laboratory system.

Comparable possibilities for manual and automated operation are implemented for the control of the optical setup with its respective GUI, cf. Figure 3.5. As the details for this setup are given in Chapter 4 no further explanation of its operation shall be given here. The same applies to the developed measurement procedure for the spectroscopic measurement and data evaluation. The later is realized in a self-developed post processing analysis in MATLAB. Both will be explained in Chapter 5.
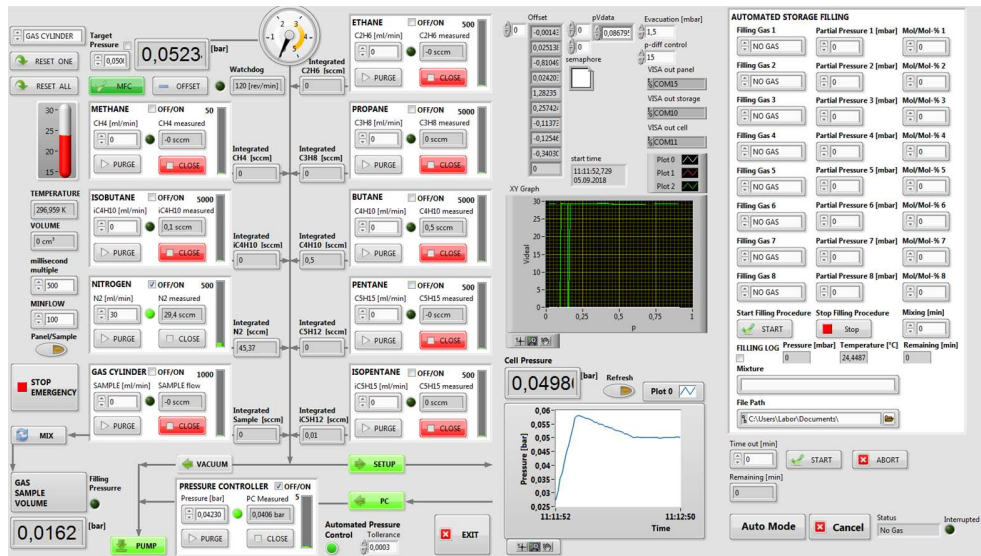
Figure 3.4: Screenshot of GUI for the gas setup (details in Appendix A).
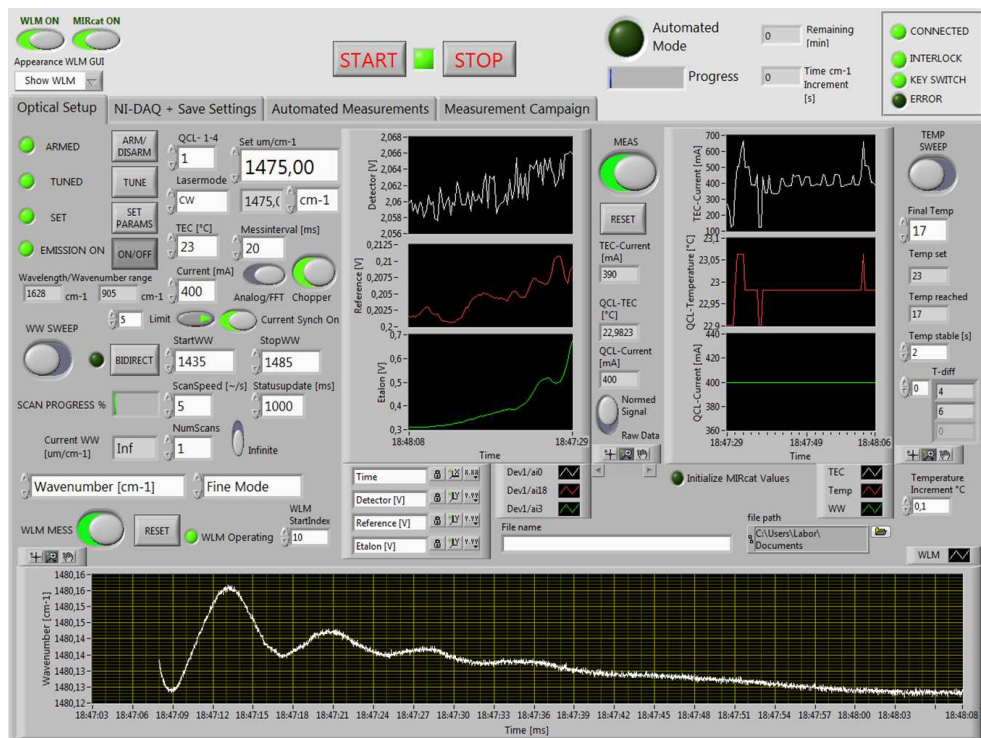
Figure 3.5: Screenshot of GUI for the optical setup (details in Appendix A).

Chapter 4

Laser spectroscopic measurement system for high resolution reference spectra

The purpose of the spectroscopic measurement system was to generate high resolution and high accuracy reference spectra. Measuring multiple pure gases as multi-species gas mixtures requires to comply with several parameters ranging from a broad wavelength coverage to a flexible adjustability of measurement conditions like temperature and pressure. Overlapping spectra of different gas species involves to discriminate resolved line spectra as unresolved broad band absorption of the larger molecules. High sensitivity should be combined with a wide dynamic range to measure gases from the permille to 100 % range. The developed system was designed to fulfill these requirements in order to reveal the challenges and limits of spectroscopic sensing of the targeted hydrocarbon species as of their mixtures.

In the following explanation the structure and functional principle of the spectroscopic measurement system will be divided into its three main entities:

- the optical setup, cf. Section 4.1 and its main components for the measurement: the gas cell, cf. Section 4.1.1, the detectors, cf. Section 4.1.2 and the etalon, cf. Section 4.1.3,

- the tunable external-cavity quantum cascade laser system - the MIRcat, cf. Section 4.2,

- the high resolution wavelength meter, cf. Section 4.3.

The focus of this chapter is to illustrate the major properties of the setup and its individual components. This knowledge was gained in extensive tests and applied in several intermediate stages of incremental development of the measurement system. The here presented configuration of the optical setup displays the final version. A profound understanding of the system and its characteristics forms the basis for the developed spectral measurement method and data analysis which will be discussed in Chapter 5.
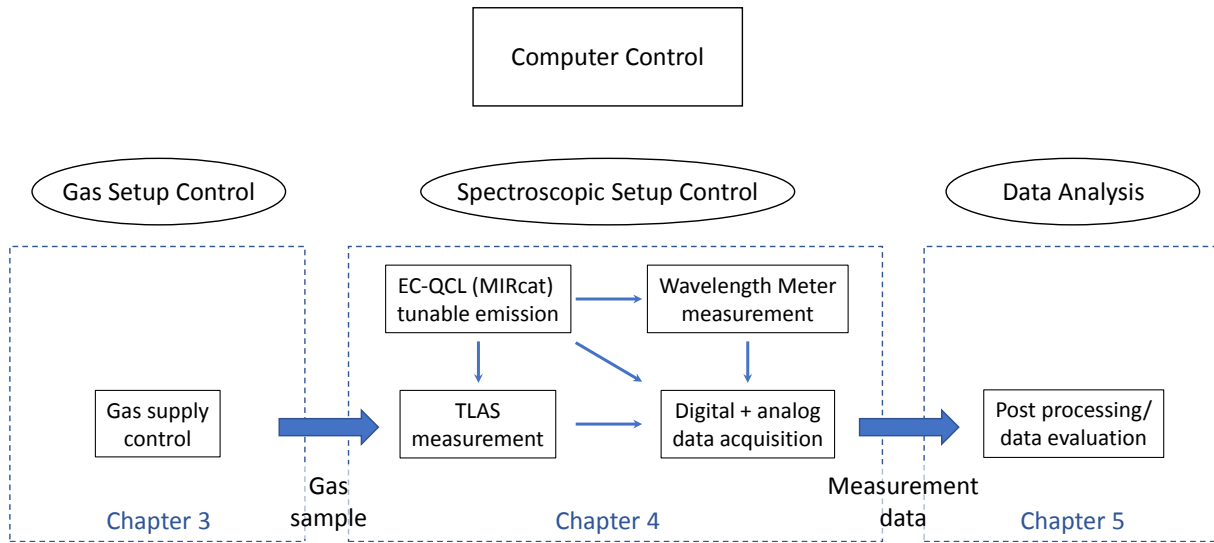
Figure 4.1: Schematic overview of the overall system to generate gas spectra. All parts are computer controlled and practically build upon one another. The previously described gas setup ensures that a gas sample is supplied to the spectroscopic measurement system which is the focus of the current chapter. The spectral measurements involve the respective components to interact that are described in this chapter. Subsequently, the measurement data has to be processed and analyzed which is outlined in the next chapter. The measurement procedure is neglected in the diagram but will be also explained in Chapter 5.

4.1   The Optical Setup

Figure 4.1 shows a schematic overview of the system parts that interact to enable the spectroscopic measurement of a gas sample. Each part is discussed in an individual chapter as indicated in the diagram. The operation and the data acquisition of the laboratory system is computer controlled and the generated measurement data post processed and evaluated separately, cf. Chapter 5.

The main part of the spectroscopic measurement system is the optical setup which connects all components to realize the TLAS measurements. The focus of the system development was to realize automated stable long-term operation. Consequently, in addition to an automated operation and measurement procedure the setup has to ensure stable measurement conditions. The assembly of the elements and their properties will be explained in the following. A sketch of the spectroscopic system with all components is given in Figure 4.2.

The EC-QCL and the Wavelength Meter are independent systems that are connected by the optical setup to realize the measurements. The explanation of their properties is covered in separate sections. All components of the optical setup are set in a nitrogen purged box to prevent distortion of the spectra by absorption from ambient water in the beam path. The EC-QCL is connected to the setup with a sealed vacuum flange. This
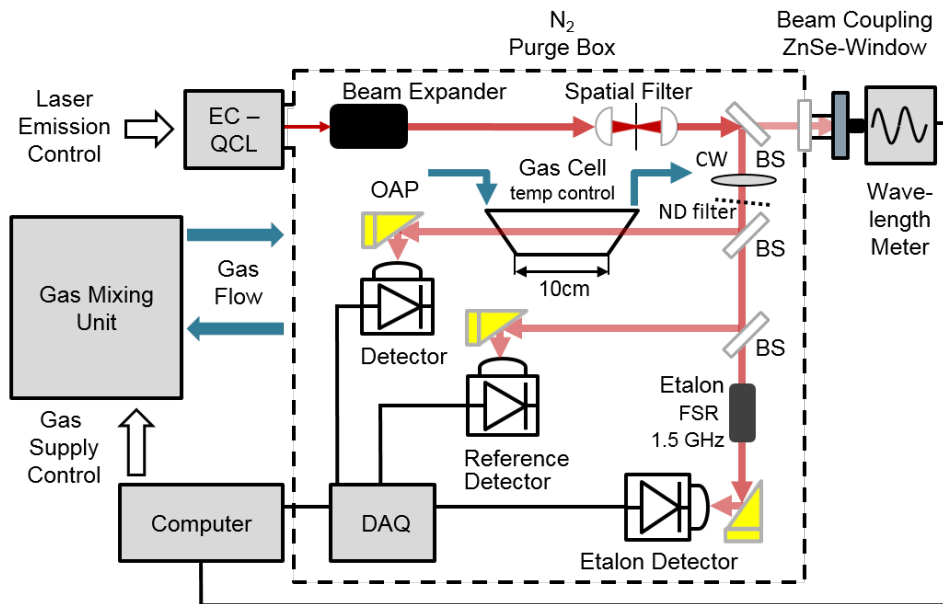
Figure 4.2: Sketch of all components of the spectroscopic system. Laser beam path indicated by red arrows. Abbreviations for elements of the optical setup: *BS* - beam splitter, *CW* - chopper wheel, *ND filter* - reflective neutral density filter, *OAP* - off-axis parabolic mirror, *FSR* - free spectral range, *DAQ* - data acquisition card.

allows to couple the beam into the setup without a supplementary window that could cause reflections or interferences. First a beam expander magnifies the beam diameter by a factor of four from 2.5 mm to 10 mm. The magnification reduces potential beam pointing fluctuations from the laser by a factor of four and thus helps to ensure a more stable beam guidance. Subsequently, a spatial beam filter or mode cleaner serves for cleaning the beam from higher mode emission and thereby realizes a stable spot of the laser radiation on the measuring devices. This spatial filter consists of two plano-convex and anti-reflection coated germanium lenses and a 150 µm pin-hole.

After this beam preparation a ZnSe beam splitter splits the beam intensity in two beams of approx. 70 % of intensity in reflection and 30 % of intensity in transmission. The transmitted beam part passes a anti-reflection coated ZnSe window and is coupled with an off-axis parabolic mirror into a polycrystalline IR fiber to be measured by the wavelength meter. The reflected part is modulated by a mechanical chopper wheel with a frequency of 987 Hz. Phase sensitive detection and demodulation (Lock-In technology) of the signals is implemented in the acquisition software in LabVIEW and briefly explained in Section 5.3.1. The procedure effectively reduces low frequency noise in the acquired signals. After modulation the beam has to be attenuated for not saturating the detectors as will be explained in Section 4.1.2. For that reason the beam passes a reflective neutral density filter that reduces the transmitted beam intensity to 10 % of the incident beam. The filter is put tilted into the beam path to avoid back reflection into the QCL. Then,

further beam splitters are used to guide the beam to three different measurement paths. In each path the beam intensity is measured with a respective detector.

In the first path the 10 cm long single path gas cell is set. Technical details of the gas cell are given in Section 4.1.1. The beam is transmitted through the gas cell and then focused with a gold coated OAP mirror with one inch focal length on the detector surface. The transmitted intensity contains the signature from the absorption of the respective gas sample in the cell. Due to the higher intensity of the reflected beam (approx. 70 %) the detector in the first measurement path acquires the highest signal. For this reason it is predestined for the gas transmission measurement to ensure a maximum signal to noise ratio. The detector in the second measurement path serves for acquisition of a reference signal. The reference intensity is used in the signal processing to normalize the signal from the measurement path which eliminates the effect of intensity fluctuations of the laser emission. The lengths of both paths were designed to have approximately the same length to minimize potential distortion of the spectra by residual water traces in the beam paths. The detector in the third path acquires the transmission through a highly temperature stable custom made air spaced etalon. The details of this optical element are covered in Section 4.1.3. The etalon transmission is used for relative wavelength referencing and data rejection in the signal processing, cf. Chapter 5, and is therefore a key element to achieve high accuracy spectra.

Special attention was set on the construction of the setup with respect to a maximum stability and adjustability of the beam guidance. The intention of these efforts was to guarantee a stable image of the beam spot on the detectors. This comprises to target an incidence of the beam on the OAP mirrors with minimum deviation from their optical axis. An inclined incidence of the beam on the OAP mirrors distorts the image on the detector surface. This can lead to fluctuations in the signal acquisition as the image of the beam spot might only partially impinge on the detector. For this reason all elements were set into a cage system and connected with metal rods. This guarantees a maximum of stability and control of the assembly of all elements. Figure 4.3 shows a photo of the setup.

The main elements of the setup for the spectroscopic measurements: gas cell, detectors and etalon will be explained in detail in the following.

4.1.1   The gas cell

The gas cell constitutes the element where the gas sample and the laser radiation interact. The light is transmitted through 37.5 mm diameter wedged and anti-reflection coated ZnSe windows and a 10 cm single path of a commercial single path stainless steel gas cell. A sketch of the cell is depicted in Figure 4.4.

The cell is heated with a heater jacket that is operated by a high stability temperature controller which allows for temperature set-points from ambient till 200° C. The heater jacket is insulated with a silicon foam insulation to stabilize the cell temperature. In addition, the inlet tubing of the gas cell is enhanced with a self-made insulation and can be heated with a heating wire that is controlled by another temperature controller. This kind of gas preheating ensures a constant gas temperature when the gas sample is fed into
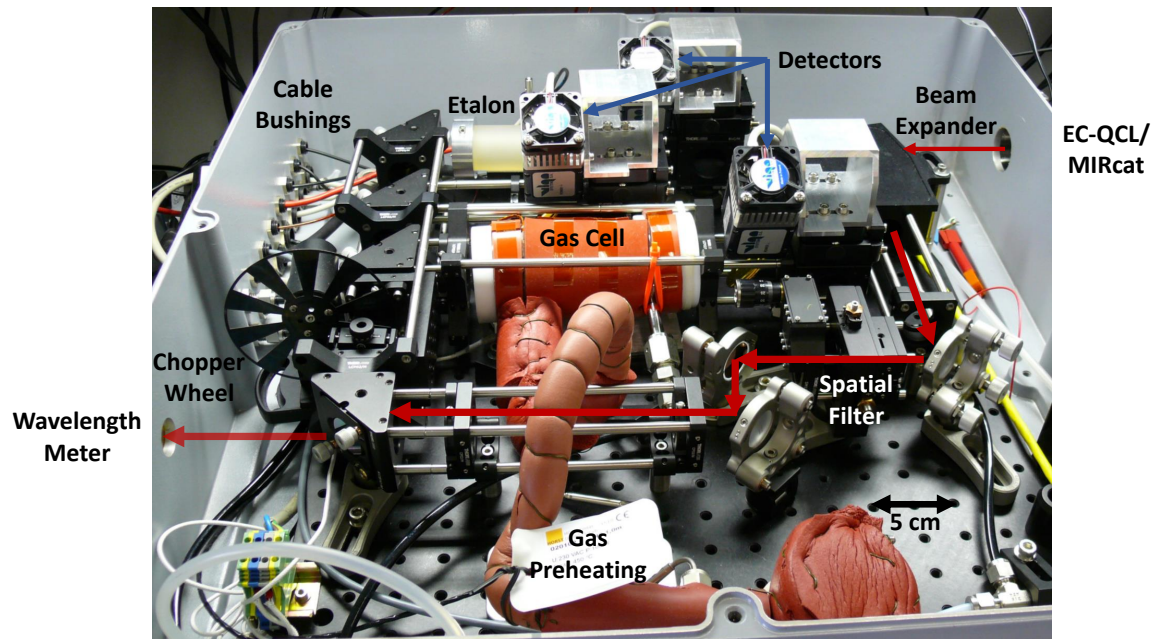
Figure 4.3: Setup with removed cover of the purged box. A part of the beam path is indicated with red arrows. The radiation from the EC-QCL enters the setup through an aperture in the upper right of the box. The main elements like the gas cell, the detectors and the etalon are labeled.
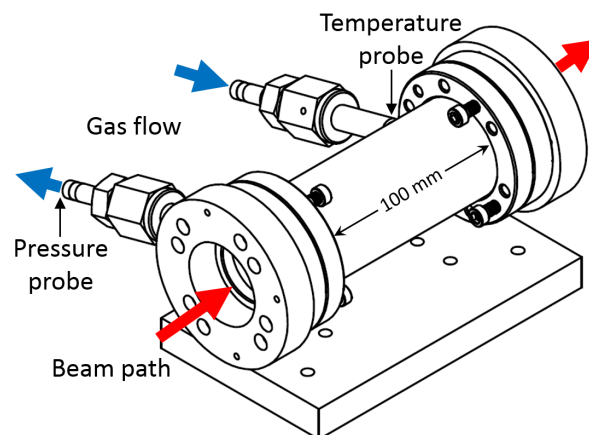
Figure 4.4: Sketch of 10 cm single path gas cell and base plate. In the setup the gas cell is wrapped in a heater jacket and insulation, cf. Fig. 4.3. At the inlet of the cell a temperature probe measures the temperature in the gas stream. A high accuracy pressure probe at the gas outlet serves as reference value for the pressure controller.

the gas cell. A Pt-100 temperature probe measures the gas temperature directly in the gas stream at the inlet of the gas cell and is monitored during the spectral measurements.

Beside the gas temperature also the pressure of the gas has to be stabilized and controlled. The pressure controller of the gas mixing unit serves for stabilization of the pressure while another high precision digital manometer probes the gas pressure directly behind the gas outlet of the gas cell. The manometer has a measurement range from 0 to 1000 mbar and a measurement accuracy of $\pm$ 0.5 mbar. The measured value serves as reference point for the pressure controller operation.

4.1.2   The detectors

The intensity of the split laser beam is measured at three points in the setup with infrared detectors of the same type, cf. Fig. 4.2. These are commercial planar mercury cadmium telluride (MCT) detectors (Vigo Systems, PVM-2TE-8) with photovoltaic multiple heterojunctions as detector surface. Thus, absorbed photons on the detector surface produce electron-hole-pairs that result in an external photocurrent. This detector current is subsequently amplified by a variable gain high speed current amplifier for each detector. The amplifier voltage output is then acquired with the analogue digital converters of a commercial data acquisition board[1] (DAQ) that is connected via USB to the setup computer, cf. Fig. 4.2.

The properties of the detector response have a crucial influence on the optical setup arrangement and the measurement procedure. Therefore, a brief overview of these characteristics and their implications will be given here.

Active area response   The detectors have an active area of 1×1 mm^2 which is cooled with 2 thermoelectric cooling (TEC) stages to an operation temperature of approx. 220 K. The manufacturer states a responsivity of the individual detectors from 0.5 % to 3 % A/W in a wavelength range from 2 to 11 μm with a responsivity peak around 8 μm.

The active area consists of multiple photovoltaic heterojunctions that are disposed in parallel line elements. The values of the responsivity curve of each detector are slightly different despite the same material systems used. Moreover tests revealed that the responsivity is not homogeneous on the detector surface but shows spatial variations in the range of $\pm$20 %. An exemplary test of the manufacturer that measured the spatially resolved signal and responsivity of a detector illustrates these findings, cf. Figure 4.5.

These properties of the detectors have the following consequences for quantitative intensity measurements: first, referencing one detector signal to another by dividing the respective signals yields not only the difference of the impinging intensities but also the difference of the individual detectors responsivities. Second, due to the inhomogeneous active area a beam pointing fluctuation of the laser emission causes variations of the detector signal even when the intensity remains stable. Therefore, the spatial filter not

---

[1] National Instruments DAQ USB-6363 BNC
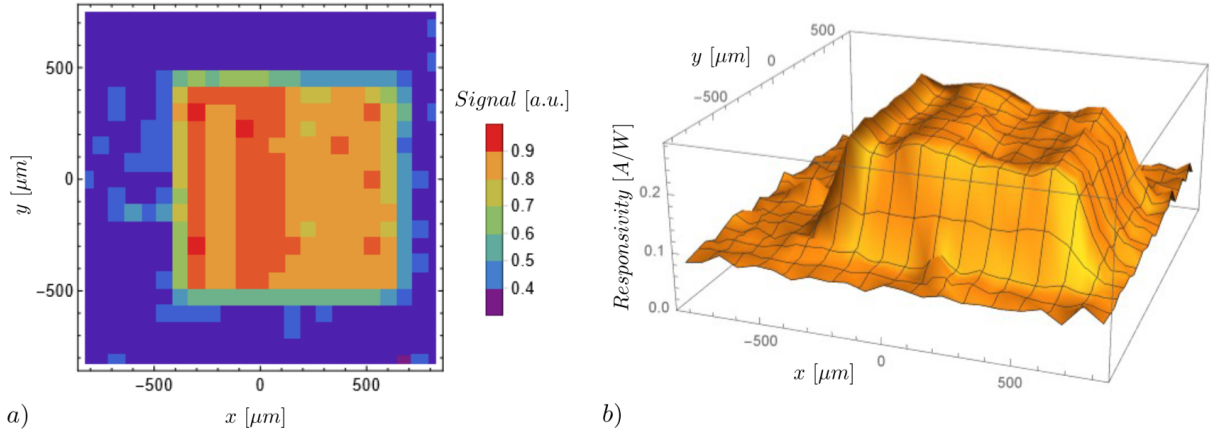
Figure 4.5: a) Measured signal of exemplary MCT detector with focused black body radiation. Estimated spot size 90 µm and scanning step 75 µm in x and y direction. b) 3D model of the responsivity of the active area (Data: courtesy of Vigo System SA).

only serves for mode cleaning but also to have a constant image on the detector surface. Both properties affect quantitative measurements and thus have to be considered.

Saturation and substrate influence   Another property of the detectors that has to be considered is their linearity range. The detectors yield a linear increase in photocurrent until 20 mW/mm². As the used EC-QCL emits cw radiation in the 100 mW range and the beam is focused by an OAP mirror on the detector surface impinging intensities can easily excess this saturation threshold. Hence, a reflective neutral density filter attenuates the beam transmission to approx. 10 % of the laser intensity, cf. Fig. 4.1.

Furthermore, the detectors possess a low responsivitiy in the range of 0.5 % to 3 % A/W. This corresponds to a low quantum efficiency for the photocurrent generation. As a result not the entire light impinging on the detector plane is absorbed in the active area. The not absorbed light intensity propagates into the detector substrate. In the substrate the remaining intensity propagates by multiple reflections and also partly reenters into the active area. This causes a wavelength dependent intensity modulation/fringing effect comparable to a Fabry-Pérot Etalon that becomes especially evident for measurements that cover a broad spectral range. In Figure 4.6 both effects, detector saturation and fringing, are qualitatively demonstrated.

The curves show fitted values of the signal ratio of two detectors for wide wavelength tuning of the laser emission. A part of the tuning range of one EC-QCL of the laser system is covered, cf. Section 4.2. Instead of using a ND filter the laser current was varied for the three measurements to reduce the emitted intensity. The gain profile dependent intensity variation of the emission of the QCL was removed by normalization of the detector signal with the reference signal of the second detector. Thus, the detector signal of the gas cell transmission was divided by the signal of the reference detector. The curves first reveal
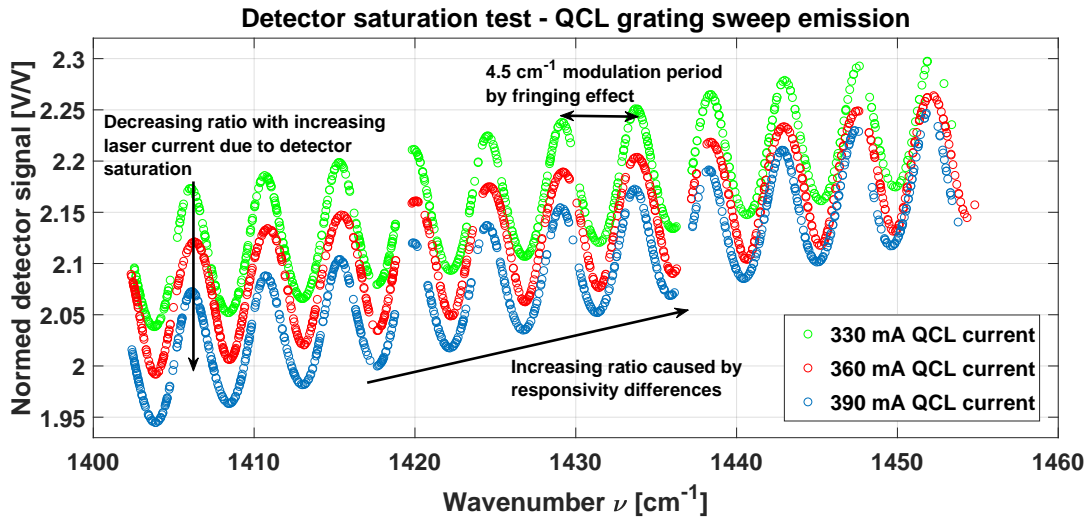
Figure 4.6: Demonstration of modulation of detector signal due to fringing in the detector substrate and nonlinear response caused by saturation of the detector. For lower laser currents the signal ratio of both detectors increases which verifies a saturation of the signal at higher laser currents.

the modulation of the signal by the fringing effect in the detector substrate. To be more precise it is a beating of the modulated detector signals due to the division of the signals. It results in a sinusoidal intensity variation with a periodicity of approx. 4.5 cm^{-1}. The linear increase of the signal ratio is due to the difference of the responsivity curves of the two detectors. Each curve corresponds to another laser current to demonstrate the saturation of the detectors.

   The ratio of both detector signals equals to two or greater. Consequently, the measured intensity behind the gas cell is twice as large as the intensity at the reference detector position. In case of a linear detector response the ratio of both detector signals should be independent of the QCL current. The signal ratio would be only modulated by the fringing effect and the deviations of the responsivity curves of both detectors. But the curves show that with increasing QCL current the ratio of the detector signals decreases. This clearly indicates a signal saturation at least in the active area of the first detector that receives twice as much intensity. The added ND filter in the beam path sufficiently reduces the laser intensity to acquire the measurement signals within the linear range of the detectors.

   To mitigate the fringing effect a custom detector mount was designed that allows for rotation of the respective detector around the center of the detector plane that coincides with the focus of the OAP, cf. Fig. 4.3. The tilted detector position reduces fringing but cannot entirely avoid it.

   Finally, these findings demonstrate that the spectral measurement signals are influenced by the detector properties. Its consideration in the data analysis procedure will be described in a Section 5.3 of the next Chapter.

4.1.3 The etalon

An etalon or Fabry-Pérot interferometer consists either of an transparent plate with two reflecting surfaces or two parallel partially reflecting mirrors. Depending on the optical distance of the two surfaces it creates a wavelength dependent transmission with equidistant maxima and minima. The surface reflectivity defines the strength of the intensity modulation. It serves as wavelength dependent relative measuring "standard" and as element in an optical setup it is commonly used as filter or spectral analyzer or both, respectively. Due to the phase dependent transmission an absolute referencing has to be implemented separately and will be discussed in detail in the later Section 5.3 about the measurement data analysis. However, a large variety of different etalons exist according to the application as to the bandwidth and the wavelength range of the transmitted light. [73]

For the spectroscopic measurements in the here described setup two different etalons were tested. The respective transmission signal is employed for the post processing of the acquired data in order to generate the gas spectra. A brief description of the function principle and the properties of the two etalons will be given here while the signal analysis is covered in the respective parts of the next chapter.

The transmission of the etalon is measured with the third detector of the setup. The modulation of the transmitted intensity is due to the partial reflection and interference of the incident light on the two parallel surfaces of the etalon. The inciding and reflected electromagnetic waves interfere and can be described as superposition of an infinite series of waves with successively decreasing intensity according to a geometric progression. The higher the reflectivity of the surfaces the stronger is the modulation of the transmitted light. The transmission can be expressed with the Airy-function:

$$\mathcal{T} = \frac{\mathcal{T}_{max}}{1 + (2\mathcal{F}/\pi)^2 \, \sin^2\varphi} \tag{4.1}$$

with

$$\mathcal{F} = \frac{\pi\sqrt{r_1 r_2}}{1 - |r_1 r_2|} \tag{4.2}$$

where $\mathcal{T}_{max}$ is the maximum transmitted intensity, $\mathcal{F}$ the Finesse is dependent on the product of the reflection coefficients $r_1 r_2$ of the two surfaces and φ the relative phase of the reflected waves. Hence, the function is dependent on a sine square modulation with the phase of the light that is proportional to its frequency and on the Finesse that sets the amplitude of the modulation. The sine function is at maximum for $\varphi = \pi$ which is the case when one round trip of the reflected wave is an integer multiple of the light's wavelength. Thus, with $\varphi = (\omega/c)d$ where ω is the angular frequency, c is the speed of light and d represents the distance between the reflecting surfaces and applying $\varphi = \pi$ one obtains

$$\nu_F = \frac{c}{2d} \quad \text{with} \quad c = c_0/n \tag{4.3}$$

where ν_F represents the frequency of the free spectral range (FSR) while n stands for the refractive index and c_0 for the vacuum speed of light. The FSR denotes the distance of the
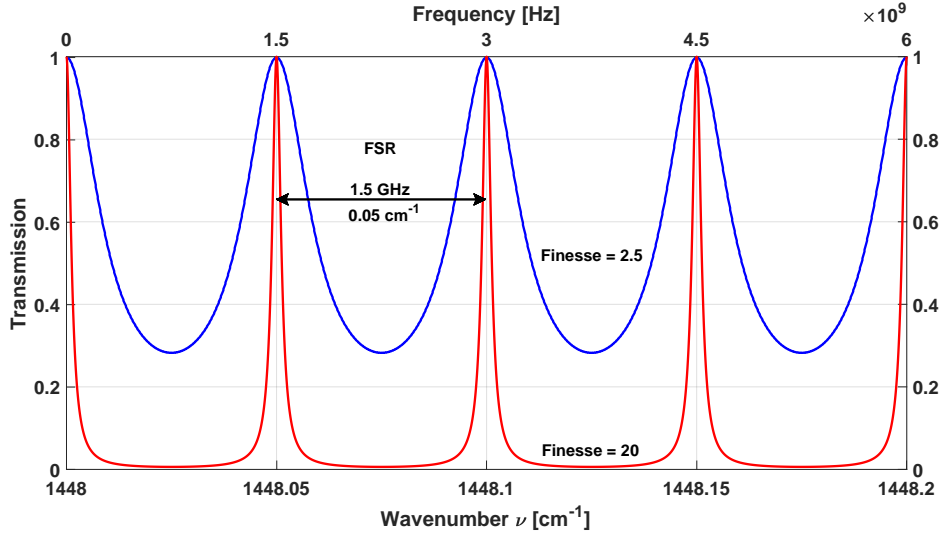
Figure 4.7: Airy transmission for two different finesse values (2.5 blue line and 20 red line) over small wavenumber/frequency range. The FSR of 1.5 GHz equals to the FSR of the etalon that was used for the spectral measurements.

transmission peaks of the Airy function, cf. Fig. 4.7. The transmission function can then be expressed as a function of the light frequency ν:

$$\mathcal{T}(\nu) = \frac{\mathcal{T}_{max}}{1 + (2\mathcal{F}/\pi)^2 \sin^2(\pi\nu/\nu_F)} \ . \tag{4.4}$$

Figure 4.7 illustrates the transmission through an etalon for two different finesse values. It reveals that a higher finesse leads to sharper and deeper resonance peaks where for small phase or frequency variation the transmitted intensity rapidly decreases.

For the spectral measurements of the gases in the setup a rather low finesse is preferable. A weaker modulation allows in the signal analysis to filter outliers and to linearize the wavenumber axis while a high finesse would lead to sharp peaks but no measurable signal between the resonances of the etalon. For that reason a germanium etalon was tested for the first measurements. Germanium is transparent over a wide range of the infrared making it preferable for mid-infrared applications and has an refractive index of approx. 4 at the targeted wavelength range. The etalon was a germanium cylinder of one inch length and one inch diameter that is manufactured with two highly parallel surface yielding an FSR of 1.46 GHz. With the reflection coefficients of the germanium air interface a theoretical finesse of approx. 3 can be expected. In the measurements a lower finesse of 2 was normally measured due to non-ideal measurement conditions (scattering losses, angle deviation, beam divergence, etc.).

Despite the general applicability of this etalon, the measurements revealed a disadvantage of solid state etalons: its susceptibility to thermal expansion. Especially, germanium has a rather large thermal expansion coefficient leading to a shift of the resonance frequency

for the etalon transmission. This shift scales linearly with the change of the distance d of the reflecting surfaces and thereby affects the resonance frequencies as the FSR. But while the FSR is in the range of GHz the frequency of the transmitted wavelength is around 10^4 larger for a wavelength of 7 µm. Thus, a temperature change during the measurements of 1°C leads to a variation of the peak distance of just 0.4 MHz while the peak positions shift more than 4 GHz for a wavelength of 7 µm. This hampers the applicability of the etalon transmission for a linearization of the wavelength axis as already a temperature change of only 0.3°C during the measurements shifts the peak positions by one FSR.

In order to mitigate this temperature characteristic another custom-made etalon was designed and manufactured. It consists of two wedged standard germanium windows of one inch diameter and 5 mm thickness and a custom-made 10 cm Zerodur hollow core cylinder as spacer of the two windows. The optical cavity of the etalon is the air path between the two windows. The cylinder was precision mechanically manufactured to guarantee a parallelism smaller than 1 µm of the two surfaces where the germanium windows are supported. The peculiarity of the Zerodur is a thermal expansion coefficient that is about a factor of 10^3 smaller than that for the Germanium. Consequently, a temperature shift of 1°C causes a shift of the peak position in the MHz range instead of GHz. This allows for a highly stable wavelength reference also for long-term measurements and is applied to linearize and thus improve the accuracy of the measured wavelength axis, cf. Section 5.3.3. The spacing of 10 cm of the windows determines a FSR of 1.5 GHz while the germanium windows air interface lead to a comparable finesse as for the germanium cylinder.

4.2 EC-QCL - The MIRcat

The laser for the spectroscopic measurements is a commercial external-cavity quantum cascade laser system from Daylight Solutions (MIRcat-1400). It consist of four individual EC-QCLs with Littrow-type cavities, cf. Section 2.3.2, with fixed cavity length that submit a combined gap-less gain from 6 to 11 µm. The opto-mechanical system enables a single output from all four QCLs. The laser radiation can be generated in pulsed and continuous wave while the continuous wave (cw) emission allows for high resolution spectroscopy. But, tuning the laser wavelength is neither entirely gap-less nor mode-hop free. A comprehensive analysis of the laser emission and its operation procedure was necessary to develop an appropriate measurement method for high resolution and high accuracy spectra over the entire tunable spectral range, cf Section 5.1.

In the following subsections the general specifications as the operation modes of the laser will be briefly illustrated. Concluding, the deficiencies of the system with respect to high resolution spectroscopic measurements are summarized.

4.2.1 System specification

The MIRcat system provides computer controlled operation for tuning the wavelength of the laser radiation and setting the temperature and current of the respective QCL.

Table 4.1: MIRcat laser beam and radiation specifications

Line width for the cw operation	typically < 0.01 cm^{-1}
Optical polarization	linear, vertical with $100 : 1$ ratio between axes
Beam profile	Elliptical Gaussian, non-astigmatic
Minimum spot size	< 2.5 mm
Beam waist	appr. 30 to 50 cm from laser
Divergence	< 5 mrad (full angle, $1/e^2$ intensity)
Pointing stability	< 1 mrad per 100 cm^{-1}
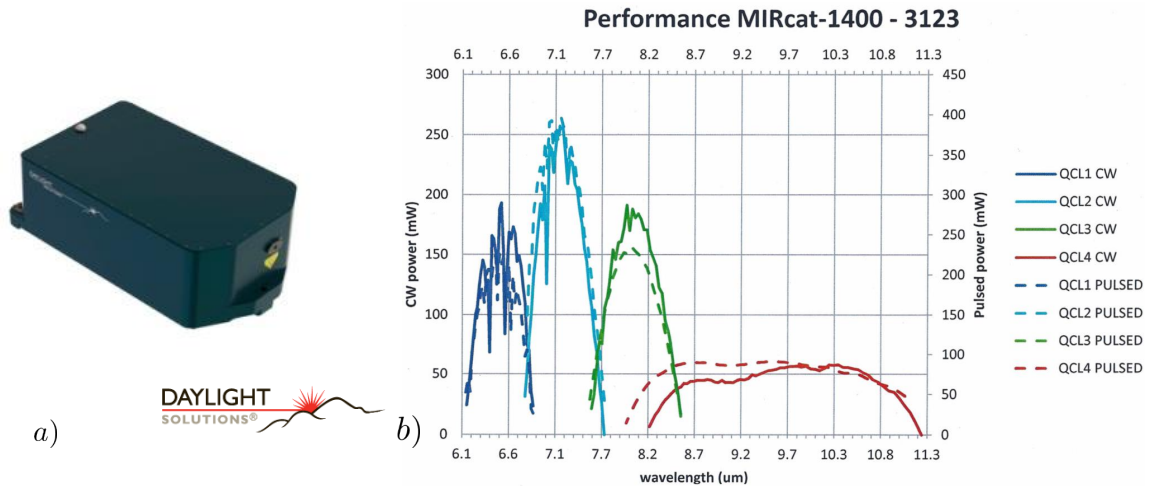
Figure 4.8: a) Picture of MIRcat EC-QCL system, b) power curves of the 4 EC-QCLs over the tunable wavelength range from 6 to 11 μm, courtesy of Daylight Solutions.

The operation can either be executed with a supplied GUI software or with a Software Development Kid (SDK) that facilitates implementation of the system functions in different programming languages. For the operation of the measurement system the laser control was implemented in the respective self-developed GUI in LabVIEW as illustrated in Section 3.3.

Table 4.1 displays an overview of the specification of the beam and the cw laser radiation given by the manufacturer [74].

In Figure 4.8 the laser system itself and the curves of power over wavelength of the emitted radiation are depicted. The tuning range of the individual EC-QCL modules can be gathered from the plot. All QCLs operate at room temperature but require water cooling at continuous wave emission.
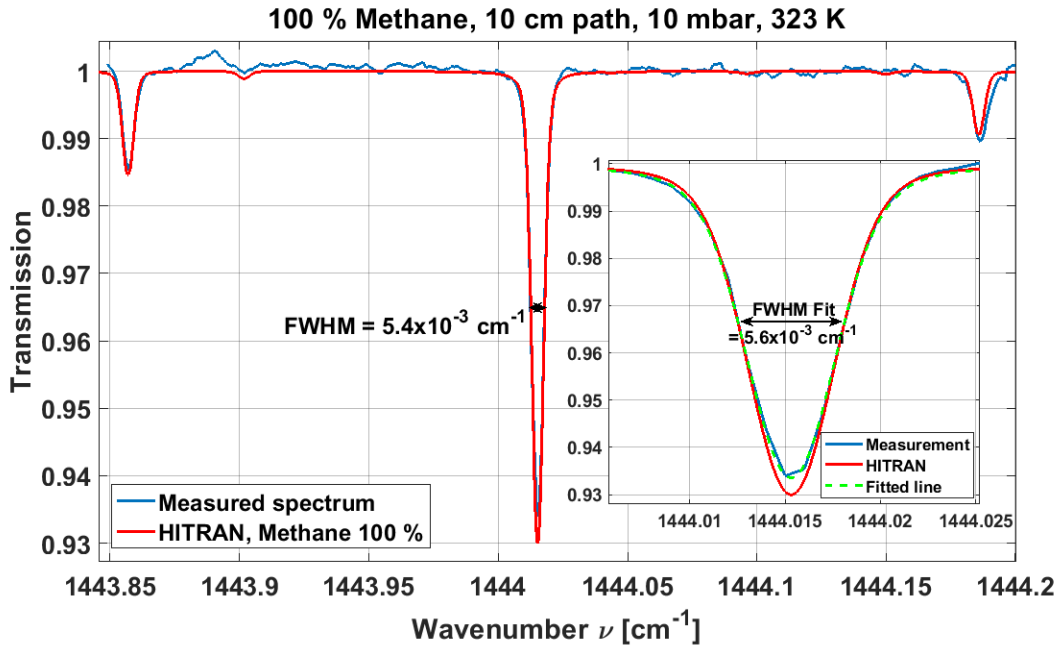
Figure 4.9: High resolution measurement of methane line transmission at a low pressure of 10 mbar and simulation of the line with parameters from the HITRAN database. The tabulated FWHM of the Voigt profile is 5.4×10^{-3} cm^{-1}. The inset reveals the small deviation of the FWHM between the measured line, the simulated line with the database parameters and depicts a simulated line with fitted line width.

Line width estimation In the specifications of the MIRcat system only an upper estimate for the laser line width is given as typical line width with < 0.01 cm^{-1}, cf. Table 4.1. For QCLs cw emission line width in the MHz or even kHz range can be achieved which corresponds to $10^{-4} - 10^{-5}$ cm^{-1} [75, 76]. A narrow line width is crucial to obtain high resolution gas transmission spectra.

Therefore, an estimation of the emitted line width of one EC-QCL of the system was done by comparing the measurement of a narrow methane line to its simulation. The measured methane line is depicted in Figure 4.9 and compared to a Voigt profile simulation with database parameters. The transmission was measured at a low pressure of 10 mbar to obtain a full width half maximum (FWHM) of the line width that is below the upper estimate of the laser width from the specifications. The FWHM of the simulation is indicated in the figure. At low pressures the major part of the line width is caused by the Doppler broadening having the distribution of a Gaussian profile while the Lorentz width from the pressure broadening is much reduced, cf. Section 2.1.2. The emission line width of the laser is assumed to have a Lorentz shape [77]. Measuring an absorption line with a broadened laser line width leads to a broadening of the measured line width of the absorption line according to a convolution of both line widths.

A Voigt function is invariant to the convolution with another Voigt function while for

the Gaussian line width f_G and the Lorentzian line width f_L by convolution the following equations apply:

$$f_G^2 = \sum_i (f_G^2)_i \qquad \text{and} \qquad f_L = \sum_i (f_L)_i \ . \tag{4.5}$$

As the laser line width is assumed having a Lorentzian profile the line width of the laser and Lorentzian part of the gas line add while the Gaussian part remains unchanged. Thus, a fit of the of the transmission with a broadened Voigt profile reveals the difference of the measurement and the tabulated Voigt width. The deviation of the fitted Voigt width can be assigned to the increased Lorentzian part from the laser line width.

The approximation of the line width of a Voigt profile by its proportions of Gaussian and the Lorentzian line width was given in Equation 2.28. This equation cannot only be used to calculated the Voigt line width from the Gaussian and Lorentzian width but also to calculate for example the Lorentzian width when the other two line widths are known. In this measurement the FWHM of the methane line is tabulated with a Voigt width of 5.4×10^{-3} cm^{-1}. The simulated transmission line is depicted in red in Figure 4.9. But as the line width varies with the measurement conditions the deviations of pressure and temperature should be considered. According to the error bands of the manometer and the temperature probe maximum deviations of $\pm$ 0.5 mbar and $\pm$ 0.3 K are assumed. The pressure variation directly affects the Lorentz width of the line while the temperature changes the Doppler broadening. However, the pressure deviation has a much higher relative error and is directly proportional to the Lorentz width while the Gaussian width is proportional to the square root of the temperature, cf. Eq. 2.24. Calculating the error propagation for the line width of the Voigt profile with the deviations of Lorentzian and Gaussian widths due to pressure and temperature uncertainties yields an deviation of the FWHM of $\pm 0.14 \times 10^{-3}$ cm^{-1}.

The visual inspection of the simulated line and the measured line in Figure 4.9 shows minor deviations in the wings of the line and a small difference in the peak intensity indicating a broadening due to a narrow laser line width. In order to estimate the laser line width the measured line was fitted to obtain a maximum overlap of measured and simulated line, cf. inset Fig. 4.9. The broadened fit of the Voigt line has a FWHM of 5.6×10^{-3} cm^{-1}.

By calculating the Lorentzian part of the line width of the tabulated Voigt width of $(5.40 \pm 0.14) \times 10^{-3}$ cm^{-1} and of the fitted Voigt width of 5.6×10^{-3} cm^{-1} the laser line width can be directly obtained from the difference of the Lorentzian line widths. A value of $(3.4 \pm 2.4) \times 10^{-4}$ cm^{-1} is obtained, which corresponds to 10.2 ± 7.2 MHz for the estimation of the FWHM of the laser line width.

The large relative error of the laser line width estimation illustrates the limited accuracy for the line width determination of narrow lines with the measurement. The assumed deviations of pressure and temperature reveal an upper estimate of the error. Concurrently, the resolution of the measurements is limited with 4 MHz or 1.3×10^{-4} cm^{-1} due to the employed wavelength meter[2] that will be introduced in Section 4.3. This resolution is in

---

[2] HighFinesse IR3-WLM6-200

the order of the line broadening confirming the limitations of the measurement. But the high congruence of measured and simulated line demonstrates that the laser line width is sufficiently narrow for high resolution measurements and significantly smaller than indicated in the specifications of the manufacturer, cf. Table 4.1.

However, even though the emitted line width is adequately narrow for high resolution measurements of the targeted gas species, a high resolution tuning of the emitted wavelength involves several difficulties. The modes of operation of the MIRcat and the accompanying behavior of the emission are described in the following sections. For realizing a high resolution gas transmission measurement, as depicted in Figure 4.9, a specific measurement and signal processing procedure had to be developed which will be explained in Chapter 5.

4.2.2 Operation modes

In general the MIRcat was employed in cw operation for the spectroscopic measurements. In pulsed operation the emission line width is in the range of one wavenumber and therefore too broad for high resolution spectroscopy. But regarding the wavelength tuning by rotation of the external cavity grating two modes of operation are available. In the following a brief explanation of both modes will be given.

Tune mode Each EC-QCL module can be independently tuned to a certain grating position while only one QCL can be operated at the same time. The minimum step of the grating rotation is indicated to be 0.1 cm^{-1} with an accuracy of $\pm$ 0.5 cm^{-1}. In this mode radiation can be only emitted when the grating is at a fixed position. During the tuning the QCL emission is switched off. Despite that, the laser current and the temperature of its thermoelectric cooling (TEC) stage can be varied during laser operation.

Sweep mode In the sweep mode the external cavity grating is rapidly rotated while the QCL is emitting. This allows a fast tuning over a part or the entire wavelength range of the respective QCL. The scan can also be combined to use the full range of the four EC-QCL modules. The scanning speed is set before the sweep in the range of 5-100 cm^{-1}/s or 0.01-0.5 μm/s.

Both modes were tested for spectroscopic measurements. The deficiencies of this preset operation modes are highlighted in the next subsection.

4.2.3 Deficiencies

The MIRcat is intended to be used for high resolution spectroscopy over its entire tunable range. The preset operation modes allow either stepwise tuning or fast sweeping of the laser emission. A high resolution spectrum would be limited by the line width of the laser emission which is < 0.001 cm^{-1}, cf. Section 4.2.1. The feasibility of high resolution measurements in both modes was tested.
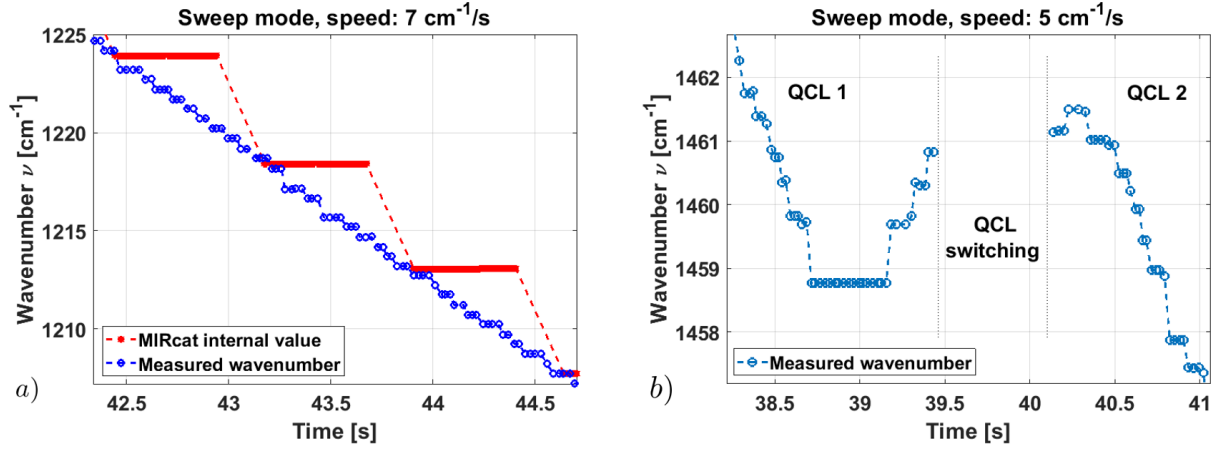
Figure 4.10: a) Internal wavenumber values from MIRcat software compared to measured wavenumbers by the wavelength meter during sweep tuning of the EC-QCL, b) Vibration of stepper motor when grating rotation is stopped or started during a sweep over two adjacent QCLs causes overshooting which leads to repeated emission of modes.

Stepwise tuning   As stated in Table 4.1 a 0.1 cm^{-1} tuning resolution of the QCL grating can be utilized. The emitted radiation was measured with a high resolution wavelength meter that will be introduced in Section 4.3. The specification of the MIRcat indicate an accuracy of the set wavenumber of $\pm$ 0.5 cm^{-1}. With the wavelength meter a deviation between the set and the measured wavenumber of 0.4 to 1.5 cm^{-1} was determined. The deviation even increased with the accumulated operation time of the respective EC-QCL unit. First this shows that the highest achievable spectral resolution by simple tuning of the EC-QCL grating is limited by the preset grating step resolution and second a supplementary reference measurement of the wavenumber is mandatory for correct assignment of the emitted frequency.

Sweep tuning   Fast rotation of the EC grating allows to cover a broad spectral range and for short measurement times but leads to mode-hops as the cavity length is not adjusted. By this coarse tuning emission modes with a spacing of approx. 0.5 cm^{-1} are sampled. The assignment of this modes to an exact frequency is hampered by a relatively slow update of the grating position in the MIRcat software. Polling of the wavenumber value yields an update every second. But even when the grating is rotated with the slowest available speed of 5 cm^{-1}/s this results in one wavenumber output from the MIRcat every tenth emitted mode. This emphasizes the need for the reference measurement of the emitted frequency with a wavelength meter. The measured values for a small part of a sweep tuning over time are depicted in Figure 4.10 a).

Concurrently, the rotation of the grating is sensitive to vibrations leading to further mode-hops and reveals an overshooting when the movement is started and stopped. As the grating is rotated by a stepper motor the starting and stopping of the motor movement is connected with a vibration, e.g. when the QCLs are switched in a broad sweep. This
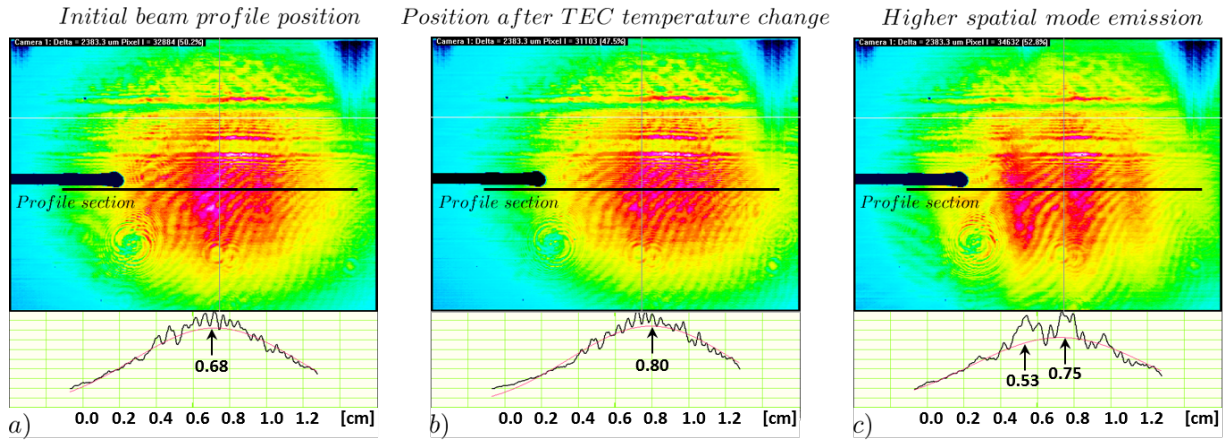
Figure 4.11: Beam profile pointing fluctuation (a and b) and higher spatial mode emission (c) due to temperature change of QCL TEC temperature. Profile section through beam pattern was fitted and the maximum position indicated, respectively. (graph below images).

overshooting is even more pronounced when a fast sweep with e.g. 100 cm^{-1}/s is executed. But also for slow turning speeds of the grating the effect still remains as illustrated in the graph of Figure 4.10 b).

Emission   In the specifications given in Table 4.1 the pointing stability of the emitted beam is indicated to be < 1 mrad per 100 cm^{-1}. In a simple test the beam pointing stability was verified. With a WinCam beam profiler camera[3] that was placed in a distance of 215 cm from the laser the intensity profile of the beam was acquired. A thin polypropylene plate was placed in front of the camera for intensity attenuation which caused slight distortions of the beam profile (horizontal lines of intensity variation in Figure 4.11 a) − c).

   The beam position remains stable at fixed grating position but shows slight variations when the TEC temperature is changed. A change of the TEC temperature induces also a tuning of the QCL emission frequency as the QCL chip cavity is altered by thermal expansion. These variations induce mode-hops which can lead to beam pointing fluctuations. For the three depicted images a horizontal intensity profile section was taken through the beam center and plotted below the image. Comparing image a) and b) by a fit to the intensity profile reveals an offset of the beam center of 1.2 mm after the TEC temperature change. This corresponds to a pointing deviation of approx. 0.6 mrad thus being within the laser specifications. But despite the beam pointing variations also the emission of higher spatial modes could be measured during the TEC temperature variations as shown by the intensity profile in image c). Both effects have influences on the spectroscopic measurements. In order to prevent a distortion of the acquired spectra the beam expander and spatial filter are added to the optical setup design as delineated in Section 4.1.

   Another constraint regarding the emission of the MIRcat are small gaps in the emission

---

[3] WinCamD-IR-BB - Broadband 2-16 µm MWIR/FIR Beam Profiler System
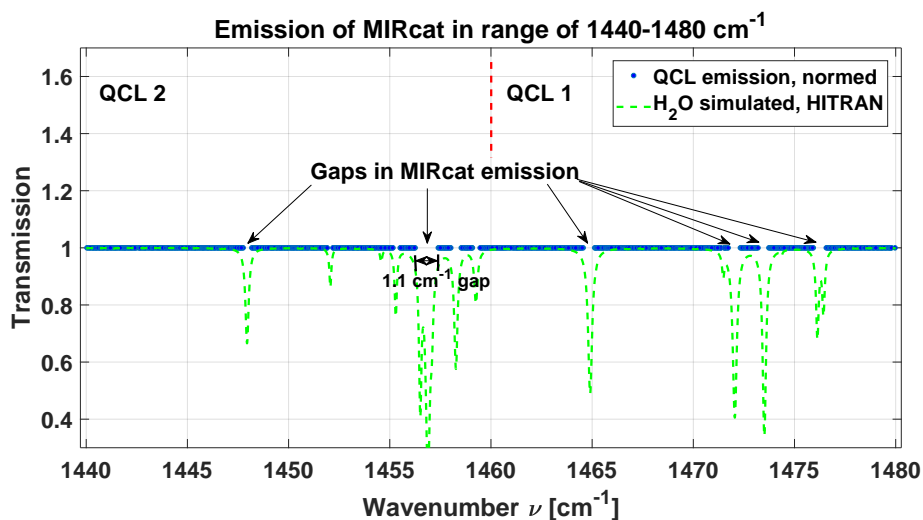
Figure 4.12: Gaps of emission for high resolution sampled emission in the targeted wavenumber range for the quantitative sensing of the seven hydrocarbons. Remaining water vapour in the external cavity of the QCLs hampers emission at strong water absorption lines which is illustrated by the dashed line of a simulated water transmission at ambient conditions (1% H_2O, 296 K, 1 bar).

spectrum. While measuring high resolution spectra, where the respective procedure is explained in Chapter 5, gaps in the acquired frequencies were determined. These gaps coincide with absorption lines of atmospheric water. Consultation with the manufacturer revealed that the cavity of the laser system is filled with dry nitrogen but contains a residual of water vapor in the ppm range. This trace concentration inhibits the lasing of the respective QCL at frequencies that coincide with strong water absorption lines. For the targeted wavenumber range for the hydrocarbon sensing the measured gaps in the emission spectrum are illustrated in Figure 4.12.

The different limitations of the MIRcat demonstrate that the laser system cannot facilitate by its standard operation the acquisition of high resolution absorption spectra. Nonetheless, the broad gain should allow to access each frequency in the whole range from 6-11 μm except for the gaps due to the residual water in the external cavities of the QCLs. A high resolution wavelength measurement of the emission requires to accurately determine the emitted frequency. The latter is realized with a Wavelength Meter that will be briefly introduced in the following Section.

4.3   The Wavelength Meter

For the accurate determination of the emitted wavelength from the MIRcat a high resolution wavelength meter[4] operational in the infrared range form 2-11 μm was used

---

[4] HighFinesse/Ångstrom, IR-3 WLM6-200

to monitor the laser emission during the measurements. An off-axis parabolic mirror couples the light into a multi-mode polycrystalline IR fibre with a transmission range of 3-18 µm. By a FC-PC connector the light is coupled into the wavemeter that consists of a temperature and pressure stabilized static Fizeau Interferometer [78]. The wavemeter allows for fast measurements up to 100 Hz acquisition rate with a high resolution of 4 MHz, a measurement precision of 100 MHz over the whole range as a guaranteed accuracy of 200 MHz of the measured value. This accuracy is realized by a routine calibration with an external calibration diode laser that is locked to an atomic acetylene line at 1532 nm which stabilizes the laser emission to ± 10 MHz.

A thorough analysis of the acquired spectra will show that an accuracy of 200 MHz is still to coarse for high resolution quantitative discrimination of the targeted gas mixtures. Therefore, a method was developed to correct for this deviation which will be explained in Chapter 5.3.3.

Chapter 5

Measurement procedure and data analysis

In the preceding chapters the development of a system for the measurement of transmission spectra of hydrocarbon gases and of their mixtures was described. In addition to the outlined technical realization a measurement procedure had to be realized. This procedure was specifically developed to compensate for the limitations of gap-less wavelength tuning of the EC-QCL system. A sophisticated processing serves for correction and evaluation of the measured signals. The precise analysis of the signals is vital to allow the generation of high resolution and high accuracy reference spectra that are suitable to analyze the spectra of multi-component gas mixtures. The procedure for the generation of these signals and their subsequent processing and evaluation are the main focus of this chapter.

In the following first the developed measurement procedure will be explained, cf. Section 5.1. A subsequent overview of the recorded data illustrates all signals that are used for the control of the measurements and the generation of the spectra, cf. Section 5.2. The multi-step post-processing of the data is necessary to generate the spectra from the measured signals. Therefore, an overview of the processing steps is given that highlights the most important parts, cf. Section 5.3 which are further explained afterwards in Sections 5.3.1-5.3.5. Additionally, the resulting spectra require an evaluation of their quality. The processing compensates for faulty measurement values and systematic errors but spectra can be affected by distortions that have to be identified and removed, cf. Section 5.4. Finally, the limitations of measurement sensitivity are discussed and a quantitative sensitivity estimation for single spectra measurements in the targeted wavelength range is given. The analysis of limits of averaging of consecutively measured spectra with the Allan-Werle deviation highlights the sensitivity limitations of the setup and quantifies the remaining noise level of spectral averages, cf. Section 5.5.

5.1 Laser operation for gapless spectral coverage

The developed setup complies with the requirements to measure transmission spectra of diverse gases in a broad range of temperature and pressure in the mid-infrared. But despite the combined broad tunability of wavelength of the EC-QCLs the system suffers from mode-hops caused by the fixed external cavity length of each individual laser. In

consequence, a gap-less coverage of the wavelength range for spectroscopic measurements cannot be realized with the preset operation modes of the MIRcat as illustrated in Section 4.2.2. Other EC-QCL arrangements in Littrow-type configuration have been reported where a piezo-actuated translation stage allows for fine control of the cavity length when the grating is rotated leading to mode-hop-free operation [61, 62]. Also, coarse tuning by rotating the grating around a pivot point shifted from the grating center enables wide tuning ranges for sectionwise mode-hop free operation and were demonstrated over more then 300 cm^{-1} tuning range with a single QCL chip [60]. Though, mode-hop-free operation is not realized over the entire gain range but by adjusting the set of parameters for each specific wavelength range resulting in 1-3 cm^{-1} mode-hop free operation at a respective grating angle. This reveals an inherent tradeoff between broad tunability and mode-hop-free operation.

The emission mode of the respective QCL in the MIRcat laser system is selected by the set grating angle and rotation of the grating allows to access other cavity modes by mode-hops. Nonetheless, a tuning of the amplified mode for a fixed grating position can be realized as outlined in the fundamental Section 2.3.2 by an additional modulation of the chip temperature within the factory-set range from 17° C to 23° C. Application notes from the laser manufacturer suggest tuning of the laser emission by sweeping of the EC grating at different QCL chip temperatures to induce mode-hops at different wavelength for each sweep [79, 80]. But the dominating chip modes of the QCL with 0.5 cm^{-1} mode spacing induce a relatively coarse sweep tuning. Despite repeated sweeps at different temperature levels, gaps in the spectrum remain and therefore does not allow for the same high resolution as the method that will be presented in the following.

For the spectral measurements with this setup an adapted temperature tuning method was developed which applies incremental changes of the QCL temperature at a fixed grating position and subsequently repeats the procedure after rotation of the grating to the next position. The graph in Figure 5.1a illustrates the laser operation procedure. The grating angle is set to a specific wavelength and the chip temperature is decreased stepwise from 23° C to 17° C by 0.1 K each step which is a factory-set limitation. Before each temperature decrement, the laser current is shortly set below the gain threshold of the QCL chip. By switching of the laser emission, the thermal load abruptly changes and the temperature of the QCL is oscillating around its set value due to the limited bandwidth of the employed thermoelectric cooler (TEC). This leads to a very effective tuning of the emitted mode around the central wavelength set by the grating position. The emission shows a combination of wavelength tuning of single modes and mode-hops which indicates a competition of EC modes and Fabry-Pérot chip modes of the laser, cf. Section 2.3.2.

The method is different from a controlled tuning of the wavelength by precisely controlled access of the modes as reported in other approaches before [81] but realizes the emission of a maximum of modes even though in a stochastic manner. The minimum mode spacing equals to approx. 0.04 cm^{-1} which corresponds to the EC modes. The procedure effectively covers nearly the entire gain profile with exception of some strong water line positions due to residual water vapor in the external cavities of the laser, cf. Section 4.2.3. After a full temperature sweep the grating is rotated to the following position 0.5 cm^{-1} next to
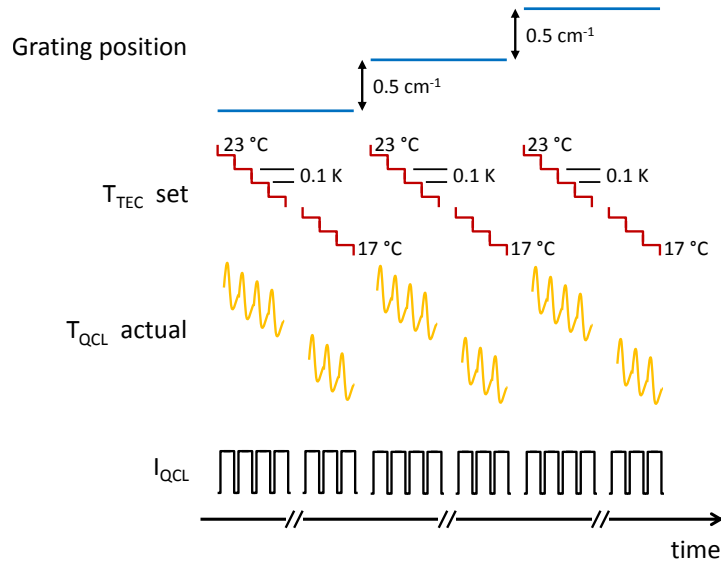
(a) Schematic illustration of the laser operation procedure for 3 grating positions: stepwise set-point of the TEC temperature (T_{TEC} set), resulting QCL temperature oscillating around set value (T_{QCL} actual), and QCL current switched on and off for every temperature step (I_{QCL}).
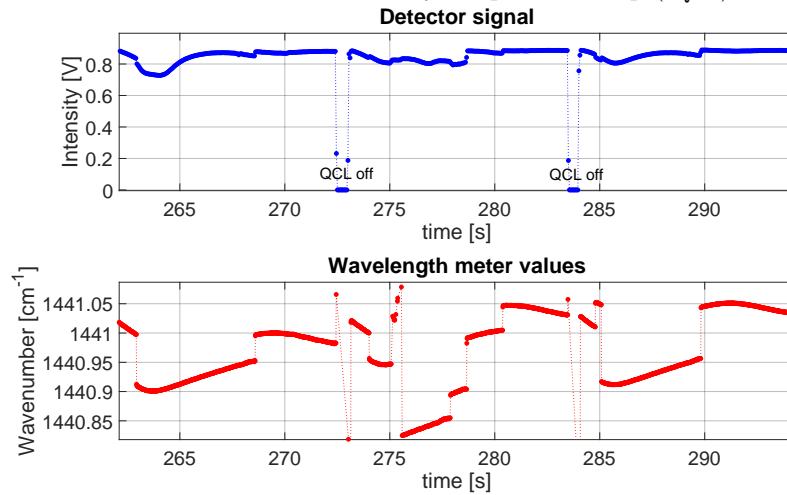
(b) Detector signal (*upper graph*) and corresponding wavelength meter values (*lower graph*) for three temperature decrements with a fixed grating position.

Figure 5.1: Illustration of the laser operation and exemplary measurement signal of one detector and the wavelength meter.

its former central mode and the temperature tuning is repeated in the same way. This procedure results in a measurement rate of 0.1 cm^{-1}/min.

The two graphs in Figure 5.1b depict the detector signal and the measured wavelength tuning, which result from three temperature increments at a fixed grating position. The zero intensity value of the detector signal corresponds to the switching of the laser current below threshold. In these exemplary graphs a temperature level is maintained

for 10 seconds before the next temperature value is set. Due to the statistic behavior of mode-hops several emission modes are accessed multiple times which results in a wavelength oversampling. Tests revealed that 5 seconds for maintaining a temperature level are sufficient to capture the amplitude of the temperature oscillation of the TEC and thereby to cover the whole emission spectrum. The collected data are sorted and stitched after the measurement.

5.2   Data acquisition

For the spectral measurements a multitude of signals is generated in the setup. These are either processed to generate the transmission spectra of the measured gases, cf. Section 5.3, or used for measurement control and monitoring. An overview of the respective devices, sample- and polling rates and the signal application is given in Table 5.1 to illustrate the monitored and processed data for the realization of the measurements.

The attainment of accurate spectral measurements requires to precisely control the measurement conditions and data acquisition. The generated signals can be monitored and recorded in the respective LabVIEW software, cf. Section 3.3. The acquisition of the individual analogue signals is realized with analogue digital converters of commercial data acquisition (DAQ) cards. The detectors and the reference output of the optical chopper are connected via BNC connectors to a National Instruments DAQ card[1] that acquires the analogue signals with its maximum sampling rate of 250 kSamples per channel to ensure highest averaging performance. Two separate ADLink DAQ cards[2] that are connected via PCI slots to the setup computer monitor and control the various analogue and digital input and output signals of the devices for the gas flow control. Further devices as the wavelength meter, the laser or the manometers have their individual digital signal outputs which are connected via USB to the computer.

---

[1] NI DAQ USB-6363 BNC

[2] ADLink DAQ 6216-GL Series Multi-channel Analog Output Card, ADLink DAQ-2204 Multi-function Data Acquisition Card

Table 5.1: Overview of devices and the acquired data during the spectral measurements. The maximum sample rate, given by the acquisition hardware, is employed for the spectra generation while the other device values are polled with a software set rate. Signals are either directly used for generation of the spectra, which means transmission and cross section calculation, for monitoring of the measurement conditions or specifically set for the automated measurement control.

Acquisition hardware and signal device	Sampling/polling rate in LV software	Analyzed for spectra evaluation	Application of signal
NI DAQ			
Detector Gas Cell	250 kSamples/s	yes	Spectra generation
Detector Reference	250 kSamples/s	yes	Spectra generation
Detector Etalon	250 kSamples/s	yes	Spectra generation
Optical Chopper	250 kSamples/s	yes	Spectra generation
USB			
Wavelength Meter	100 Samples/s	yes	Spectra generation
MIRcat (I_{QCL}, T_{QCL})	2 Hz	no	Measurement control
Pt-100 Gas Cell	2 Hz	yes	Setup monitoring
Manometers (Cell/Panel/Storage)	2 Hz	yes	Measurement control
N_2 Box temperature + relative humidity	sampling on demand	no	Setup monitoring
ADLink DAQ			
MFC gas flows (8x)	2 Hz (only monitored)	no	Measurement control
Pressure Controller	2 Hz (only monitored)	no	Measurement control

5.3   Signal processing for spectral data generation

The acquired signals have to be processed to generate gas transmission spectra. The processing and analysis of the signals is crucial to realize high resolution and high accuracy transmission spectra. Therefore, a comprehensive processing procedure was developed.

A first processing of the detector signals and the recording of the raw data of the other signals is realized in LabVIEW . All subsequent steps are done by post-processing of the data in MATLAB. A schematic overview of the main steps is given in the flow chart in

Figure 5.2. The procedure contains several general data processing steps as some filtering methods and synchronization of the independently sampled signals. In addition processing methods were developed that improve the spectral information of the signals that are obtained in the specific measurements with this setup. These are essential to obtain high accuracy transmission spectra from the acquired data. The respective parts in the flow chart are highlighted.

   The first two methods are necessary to remove modulations and artifacts on the signals that are caused by the setup operation. This includes the demodulation, cf. Section 5.3.1 of the modulated detector signals and filtering of signal parts that either contain no information or faulty data, cf. Section 5.3.2. The latter may be caused by the switching of the laser emission during the tuning process and the resulting mode-hops that need to be identified to omit a wrong wavelength assignment in the measurements. The subsequent processing serves for increasing the wavelength accuracy beyond limits imposed by the wavelength meter, cf. Section 5.3.3. The implemented method forms the essential element of the processing to obtain high accuracy transmission spectra. After these steps for preparation and correction of the signals the absolute transmission spectra are calculated by baseline normalization, cf. Section 5.3.4, and referencing of the measured absorption lines to high accuracy database values, cf. Section 5.3.5.

   As these methods constitute the main parts of the procedure a more detailed explanation will be given in the following.
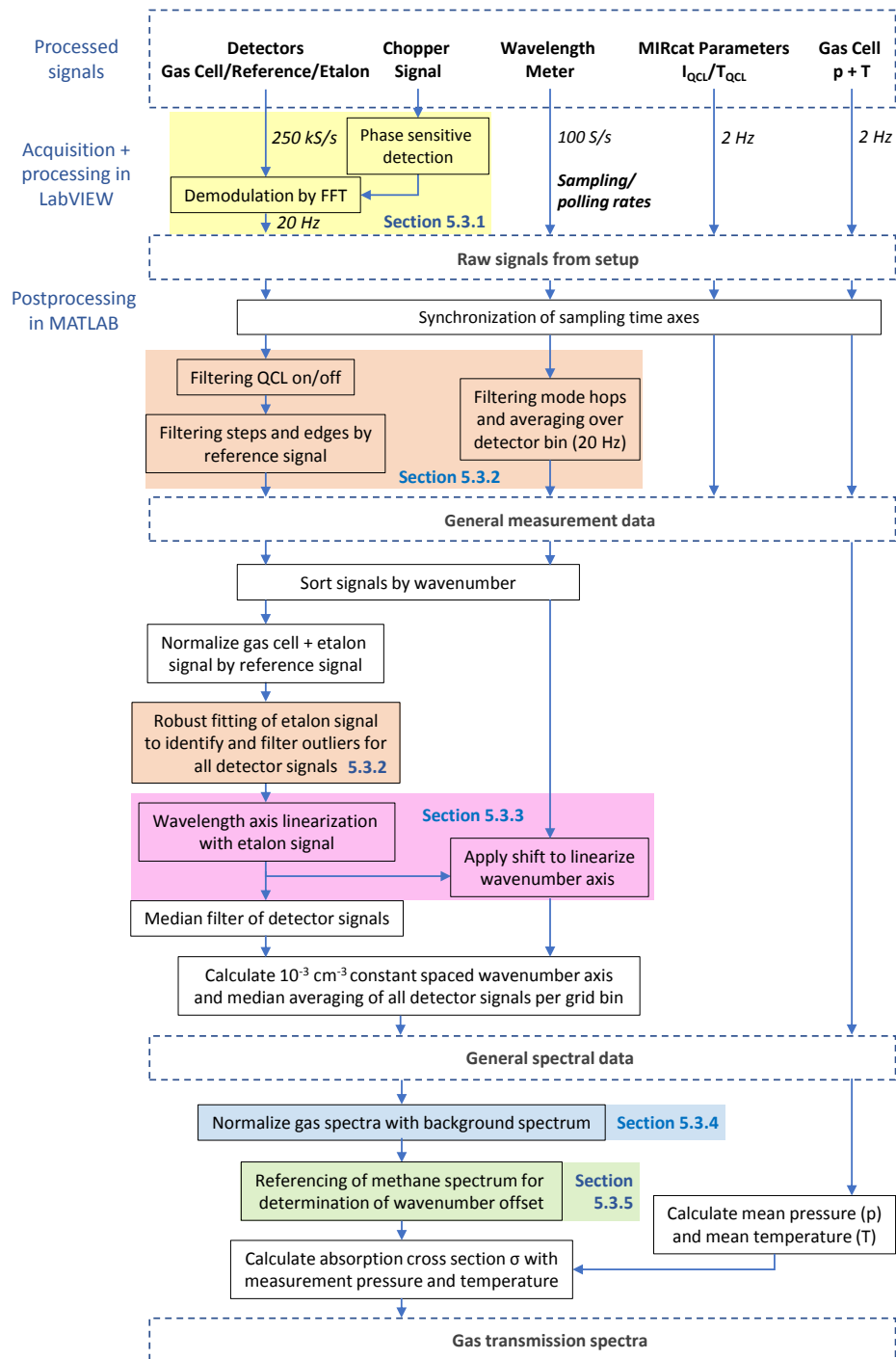
Figure 5.2: Flow chart of the signal processing for generation of the gas transmission spectra. Processed setup signals indicated on top. Processing is implemented in LabVIEW and MATLAB. The highlighted parts are explained in the indicated Sections.
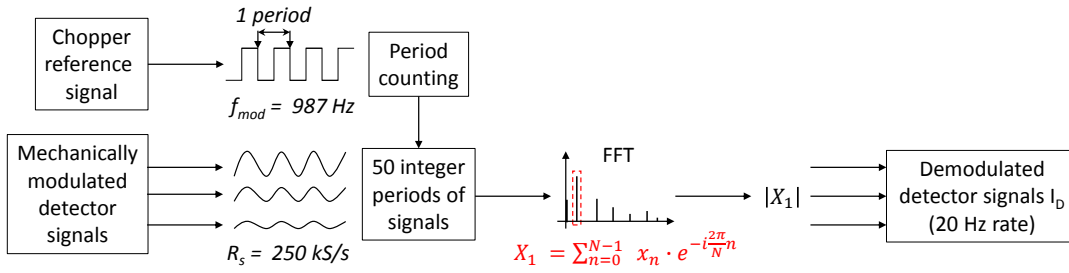
Figure 5.3: Illustration of demodulation processing of the detector signals. The chopper signal is used for counting of the modulated signal periods. After the FFT of the respective block with 50 periods of the modulated signal and N samples the amplitude of the first harmonic X_1 is kept. The sampling rate R_s of 250 kS/s per detector signal is reduced by the demodulation to a sampling of the detector intensities I_D with a frequency of 20 Hz for each detector signal.

5.3.1   Demodulation

The three detector signals and the chopper reference signal are recorded on independent channels with a sample rate of $R_s = 250$ kS/s each. The chopper mechanically modulates the laser radiation with a modulation frequency of $f_{mod} = 987$ Hz. The frequency value is set a few hertz below 1 kHz to avoid 50 Hz overtone parasitic frequencies in the Fourier spectrum that could arise from the electric supply frequency. First demodulation with a digital lock-in amplifier was tested and confirmed to effectively reduce low frequency noise. Then a digital demodulation of the detector signals was implemented in the LabVIEW software that acquires the digital samples from the acquisition card (DAQ).

The demodulation contains a self-implemented routine that counts the modulated periods by analyzing the reference signal of the chopper. This allows phase-sensitive demodulation over integer periods of the modulated signals. The implemented routine demodulates the detectors signals by a fast Fourier transform (FFT). The period counting allows to analyze integer period signal blocks. The complex amplitude of the first harmonic of the Fourier spectrum of the signals contains the measured intensity at the respective detector. The absolute value is calculated and stored. In addition to a noise suppression the demodulation allows to discard the dc of the Fourier spectrum. In consequence no correction for potential detector signal offsets or drifts has to be applied. The procedure is illustrated in Figure 5.3.

In demodulation a compromise has to be found between effective noise reduction and a sufficiently high update rate of signals that may have fast varying intensities. Long averaging times, thus demodulation over time constants much longer than the modulation period, yields very effective noise suppression but induces a slow update rate. In the processing of the signals for the spectral measurements a demodulation over 50 periods was implemented which reveals a sampling of the detector intensities I_D of approx. 20 Hz. Noise suppression and a time resolution that appropriately samples the slow intensity variation of the temperature tuned laser emission was obtained.

5.3.2   Data rejection

After the demodulation of the detector signals all data from the setup is transferred to the post processing in MATLAB, cf. Fig. 5.2. The first processing steps concern the rejection of data that include no spectral information or incorrect data. This applies to the detector signals and to the measured values from the wavelength meter.

In the acquired detector data first those parts are discarded where the QCL current is set below threshold, cf. Fig. 5.1. Secondly, steps in the detector signal are detected. These may arise either due to the switching of the QCL emission or due to mode-hops. The detection is done in the reference signal I_{Ref}, cf. Eq. 5.1, that is neither modulated by a gas absorption nor by the etalon transmission. For detected steps in the signal one value before and one after the step are discarded on all three detector signals. As empirical criterion for the signal step filter a discontinuity of the signal of 10 % or more than the mean reference signal was applied in the signal evaluation:

$$|I_{Ref}(n+1) - I_{Ref}(n)| \geq 0.1 \cdot \frac{1}{m} \sum_{n=1}^{m} I_{Ref}(n) \tag{5.1}$$

The measured wavelengths from the wavelength meter are sampled with a 100 Hz rate. This constitutes an oversampling in comparison to the 20 Hz rate of demodulated detector signals. Thereby, it allows to average wavelength values recorded during each demodulation of a detector value. In addition mode-hops that might occur during the demodulation can be identified. The criterion identifies a mode-hop, when the difference between two subsequently measured wavelength values reaches a value equal or larger than the internal mode spacing of the EC-QCL of 0.04 cm^{-1}. The corresponding demodulated detector signals are discarded.

These processing steps already effectively filter the acquired data. But the analysis of the filtered signals reveals still distortions due to outliers. These outliers may be caused by multi-mode emission that can arise from occasional back reflections into the laser. Reflections are well suppressed by exact alignment of the optical system but occasionally occur due to the wide spectral range of the acquired spectra and the wavelength dependent alignment.

An investigation of the etalon signal most obviously shows outliers in the signal data. After the first filter steps and the wavelength averaging the signals are sorted by wavelength and the gas cell and etalon detectors signals are power normalized by the reference signal. In the resulting etalon transmission curve outliers become particularly obvious. By fitting the Airy transmission function $T_{Airy}(x, \nu_i)$, cf. Eq. 4.4, to the measured etalon spectrum $I_{Etalon}(\nu_i)$ deviations between fitted and measured values can be determined.

The fitting procedure is performed with a least square nonlinear curve fit:

$$\min_{x} \sum_{i} (T_{Airy}(x, \nu_i) - I_{Etalon}(\nu_i))^2 \tag{5.2}$$
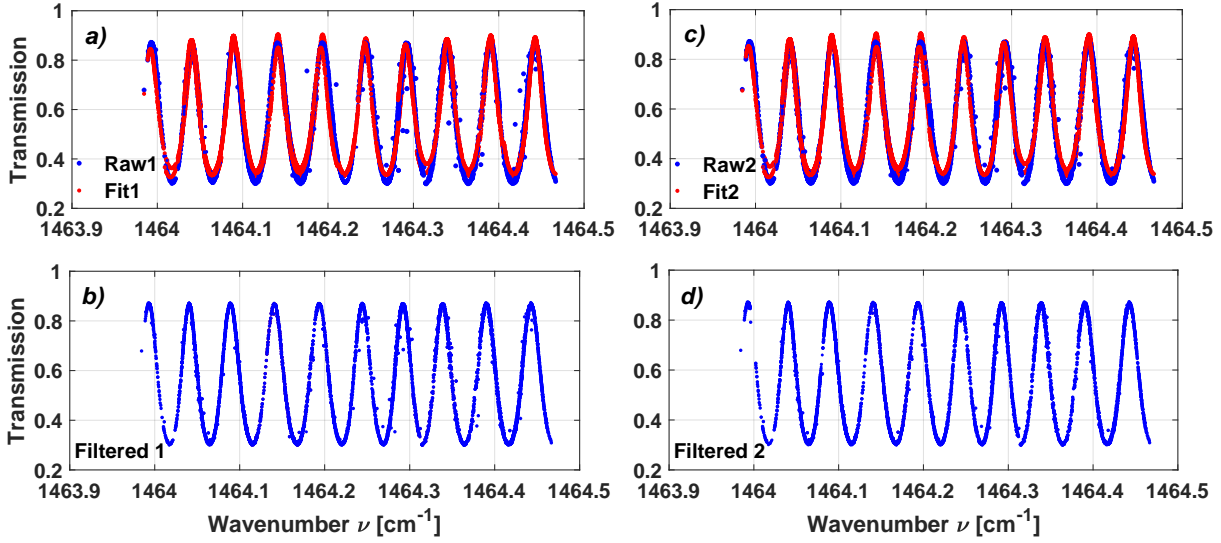
Figure 5.4: Robust fitting of etalon transmission to filter outliers in the data: a) raw data from etalon transmission (Raw1) for one grating position of the EC-QCL and fit (Fit1), b) filtered data with 10 σ_{mean} filter threshold, c) data after first filtering (Raw2) and second fit (Fit2), d) filtered data with 5 σ_{mean} filter threshold.

as parameters x of the fitted Airy function the maximum transmission $\mathcal{T}_{max}$, the finesse $\mathcal{F}$, the phase φ and the free spectral range ν_F are varied to minimize the loss function. The fitting is applied to each single period of the transmission as the acquired wavelength axis shows deviations due to the limited accuracy of the wavelength meter. The correction of these deviations is covered in Section 5.3.3.

Furthermore, the sampling point density is not constant due to the mode-hops of the laser that stochastically cover parts of the spectrum leading to parts with more and parts with less measured values. In order to ensure that the least square algorithm evenly weights all parts of the spectrum the signal values are multiplied with a weighting function that is inversely proportional to the data point density of the measured transmission. The point density is determined over equidistant bins of 0.001 cm^{-1}. In addition the standard deviation σ of the transmission values per bin is determined. These values are used for the subsequent outlier determination.

For higher robustness the rejection of the outliers is realized in two steps. An example set of measured data is given in Figure 5.4. The raw data is fitted period wise and the difference between fit and measured data determined. If the deviation of the measured data from the fitted curve is larger than ten times the mean standard deviation σ_{mean} of the transmission data bins the value is discarded from the etalon curve. Then, the filtered curve is fitted again and the threshold set to five times the mean standard deviation. The procedure effectively rejects the majority of the outliers, cf. Fig. 5.4, that are also discarded from the two other detector signals.

The fitting of the data with a further decreased deviation threshold was not implemented

to avoid too exaggerated data rejection which may be caused by imperfect fitting of the transmission. Fitting errors and faulty data rejection is mainly caused by partly incomplete data coverage due to small measurement point density or fitting of partial Airy transmission peaks. In Figure 5.4 d) this effect can be observed. At 1464 cm⁻¹ the etalon transmission peak is incomplete. Therefore, the fit slightly deviates in graph c) from the measured transmission. In consequence the difference between measured data and the fitted curve is increased even though no obvious outliers exist. The set threshold leads to the effect that a part of the transmitted curve is rejected that has no outliers. For higher clarity Figure 5.4 b) and d) can be compared at 1464 cm⁻¹. Repeated fitting of the transmission and discarding signal with a further decreased threshold revealed that depending on the measurement range and data quality this effect can strongly remove parts of the spectra that contain correct data.

5.3.3 Wavelength axis linearization

The wavelengths in the spectral measurements are determined with the wavelength meter, cf. Section 4.3. The guaranteed accuracy of the measured wavelength values within its operating range is ≤ 200 MHz. Comparison of spectra that were acquired at different dates revealed variations of the wavelength axis in the specified accuracy range. The main reason for variations are temperature changes in the laboratory environment that slightly influence the calibration of the Fizeau Interferometer in the wavelength meter and thus affect the determined wavelength. Due to the long measurement times for the spectra acquisition of hours or days this effect hampers the analysis of the high resolution spectra especially for the quantitative determination of the components in gas mixtures.

In order to improve the accuracy of the wavelength determination a method was developed to correct these deviations. The basis for this correction is the transmission of the employed etalon. This is used for linearization of deviations in the measured wavelengths axis. Subsequently to the linearization by data processing a referencing of the measured transmission to highly accurate methane line positions that are tabulated in the HITRAN database is applied for the absolute determination of the wavelength position, cf. Section 5.3.5.

As outlined in Section 4.1.3 we employ a custom-made air-spaced etalon. The spacer of the windows is made of Zerodur which is a highly temperature stable material, thus yielding a "quasi-zero" expansion coefficient at room temperature. Therefore, the modulation by the etalon generates a very constant spacing of the transmission peaks which serves as a highly stable relative wavelength reference.

The analysis of the measured etalon transmission reveals a non-equal peak spacing due to the uncertainties in the wavelength meter measurements. Hence, a correction of the respective phase deviation of each measured value has to be realized. This is implemented in the signal processing with a complex demodulation of the measured signal with a synthetic transmission function with constant FSR.

The signal processing for the linearization of the wavelength axis involves several steps that are briefly summarized in Figure 5.5. Due to the non-homogeneous distribution of
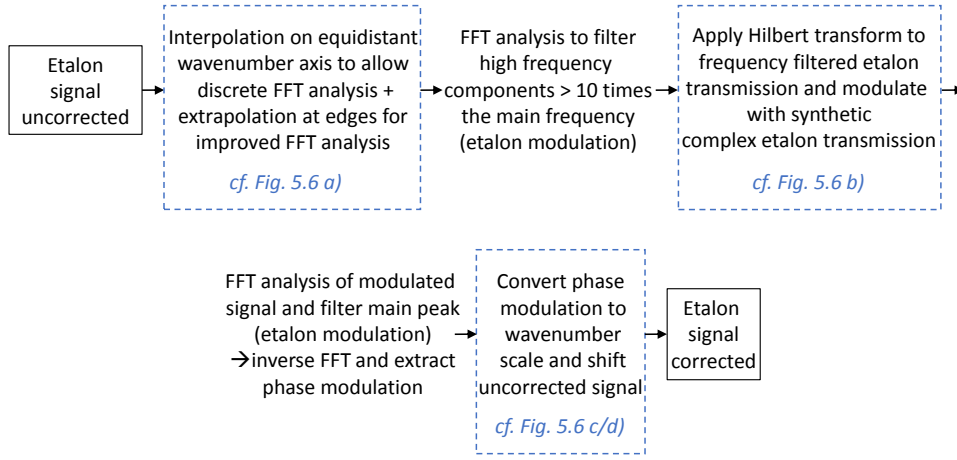
Figure 5.5: Overview of signal processing steps for wavelength axis linearization.

the acquired data an interpolation of the signal and the extrapolation at the edges serves as preprocessing for an effective FFT analysis. In the FFT analysis higher frequencies are filtered to obtain a smoothed transmission after the inverse FFT. Afterwards, a Hilbert transform is applied to the smoothed signal to calculate the analytic signal representation of the etalon transmission [82, 83].

The Hilbert transform is a linear integral transform that is applied in signal processing to derive the analytic signal representation of a real-valued signal. The transform is given in Equation 5.3:

$$g(y) = \mathcal{H}\left\{f\right\}(y) = \frac{1}{\pi}\int_{-\infty}^{\infty}\frac{f(x)}{y-x}dx \tag{5.3}$$

where x and y are real value variables of the real- or complex-valued functions f and g. The Hilbert transform can also be expressed by a convolution with the function $1/(\pi y)$:

$$g(y) = \mathcal{H}\left\{f\right\}(y) = f(y) * \frac{1}{\pi y} \tag{5.4}$$

The representation of the transform in the frequency domain is particularly simple as it applies a phase shift of 90° to every Fourier component of a function. Thus it can be applied to a signal to derive the analytic signal that has no negative frequency components. The analytic signal $f_a(y)$ is a complex-valued function representation of a real-valued function $f(y)$ comprising the original function and its Hilbert transform as given in Equation 5.5:

$$f_a(y) = f(y) + if(y) * \frac{1}{\pi y} = f(y) + i\mathcal{H}\left\{f(y)\right\} \tag{5.5}$$

where i is the imaginary unit with $i = \sqrt{-1}$. In the spectrum of a Fourier transform of the analytic signal the negative frequencies can be discarded with no loss of information.
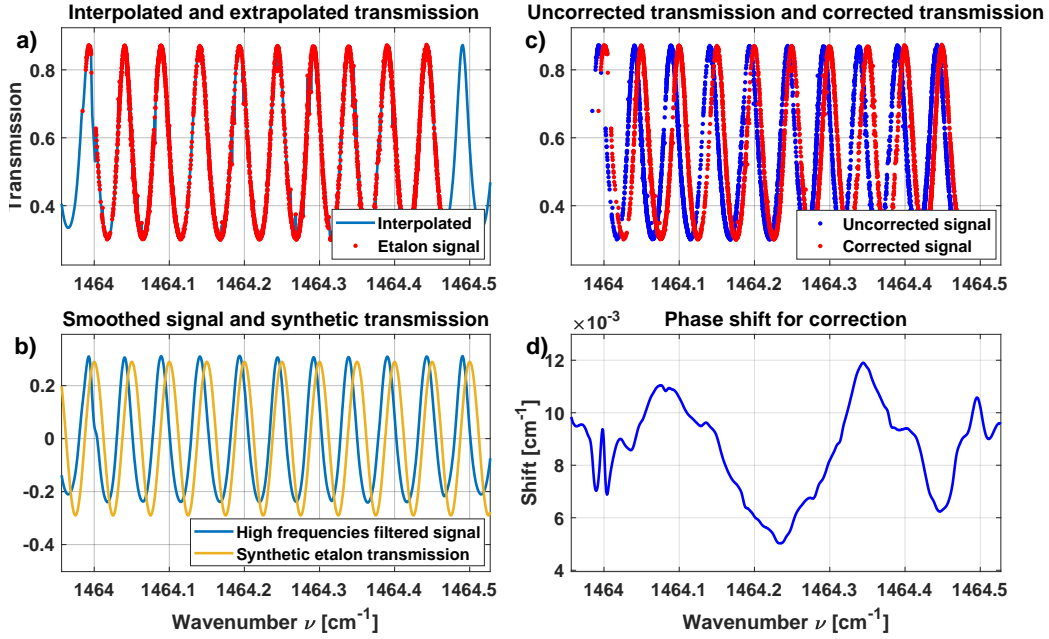
Figure 5.6: Illustration of signal processing steps for wavelength axis linearization:
a) interpolation of acquired signal and extrapolation at the edges for improved FFT analysis,
b) smoothed transmission after high frequency filter in FFT analysis and synthetic transmission
for demodulation, c) raw signal and phase corrected raw signal, d) applied phase correction
converted in cm^{-1}.

This facilitates modulation and demodulation that is applied for the linearization of
the wavelength axis. For correction of the distorted wavelength axis a multiplication
of the analytic signal representation of the etalon transmission signal with a synthetic
complex transmission function with a constant FSR of 0.05 cm^{-1} is applied. Subsequent
calculation of the FFT spectrum allows to discard the main frequency that corresponds to
the modulation by the etalon. After this frequency filter an inverse FFT is calculated from
which the phase difference between the analytic signal and the synthetic etalon transmission
can be extracted. This procedure is analogous to a complex demodulation of the etalon
transmission signal [84]. The obtained phase in radiant is converted to the wavenumber
scale as a radiant phase of 2π equals to a full FSR of 0.05 cm^{-1}. These values are added to
the measured wavenumber scale of the measurement to linearize the peak spacing of the
etalon tranmission and thus the measured frequency axis.

   Figure 5.6 illustrates the different steps of the signal processing by showing intermediate
results of the analyzed signal. To better illustrate the stretching of the wavelength axis
that creates the constant peak spacing Figure 5.7 shows the peak spacing of an exemplary
transmission before and after the correction. The depicted data was averaged on a
wavenumber axis with equidistant spacing of 0.001 cm^{-1}, cf. signal processing flow chart
in Fig. 5.2.
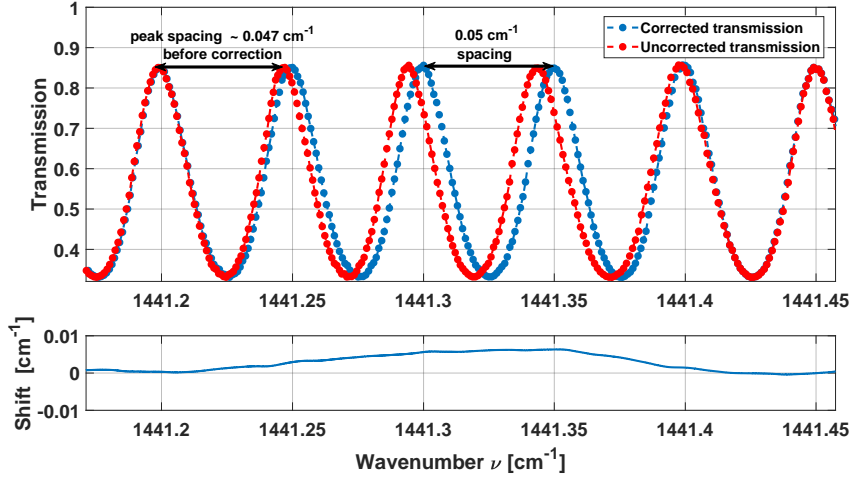
Figure 5.7: Exemplary phase correction of etalon transmission with uncorrected and corrected signal (*upper graph*) and the phase shift applied to the uncorrected signal (*lower graph*). The peak spacing before and after the correction is indicated.

Finally the linearized wavenumber axis has to be referenced to an absolute wavelength axis. The applied shift equalizes the peak spacing but due to the phase dependence of the modulation of the etalon the absolute position of the frequency is undetermined. The employed method for correcting this offset will be described in Section 5.3.5.

5.3.4   Normalization

After the processing steps that rejected faulty data and corrected the systematic deviations of the wavelength measurement the signal from the gas cell transmission needs to be normalized to obtain transmission spectra. The normalization includes the correction for gain dependent intensity variation of the laser emission, the wavelength dependent baseline modulation by the optical setup (e.g. lenses, windows, beam splitter, etc.) and especially the modulation of the acquired signal by the detector properties , cf. Section 4.1.2.

Generally, variations of the laser intensity are effectively compensated by the division with the reference detector signal while the setup induced modulations remain as signatures on the acquired signals.

Thus, normalization is most effectively realized by the acquisition of background spectra that include all intensity modulations of the measurements. For these background spectra the gas cell is purged with dry nitrogen. The spectra are acquired as described in Section 5.1. The quotient of the background signal from the detector behind the gas cell $I(\nu_i)_{bkg}$ and the reference detector $I(\nu_i)_{ref_{bkg}}$ yields the background of the measurements. The measurement of a gas transmission spectrum with the transmission signal $I(\nu_i)_{gas}$ and the respective reference signal $I(\nu_i)_{ref_{gas}}$ is then normalized with the previously measured

background spectrum. The resulting transmission signal $T(\nu_i)$ is given by the following equation:

$$T(\nu_i) = \frac{I(\nu_i)_{gas}}{I(\nu_i)_{ref_{gas}}} \cdot \left(\frac{I(\nu_i)_{bkg}}{I(\nu_i)_{ref_{bkg}}} \right)^{-1} \tag{5.6}$$

The normalization of a measured gas transmission spectrum assumes that the previously measured background does not change during the measurements. The baseline stability of the measurements will be analyzed in Section 5.5.

5.3.5 Methane line referencing

As described in Section 5.3.3 the correction of the wavelength axis lacks the determination of the absolute position of the spectra. But after the normalization the acquired transmission spectra can be compared to simulated spectra that are generated with database parameters. For the targeted hydrocarbons methane is the most extensively studied molecule. The *high*-resolution *trans*mission molecular absorption database (HITRAN) [29] lists the line parameters for the simulation of pure methane transmission spectra. In the targeted spectral range the database states an accuracy of the line positions of $0.14 - 0.55 \times 10^{-3}$ cm^{-1} [85]. Hence, a direct comparison of the acquired spectra and simulated spectra is feasible to investigate the accuracy of the spectral shape, cf. Section 6.1.1, and the spectral position. The accuracy of the listed line positions is higher than the resolution of the acquired spectra (0.001 cm^{-1}). Therefore, the offset for the acquired spectra can be determined without a loss of accuracy.

The offset is determined by calculating the cross-correlation [86] $X_{cross}(\nu_k)$ of the measured spectrum $T_{meas}(\nu_i)$ with i transmission values with a simulated spectrum $T_{sim}(\nu_i)$ as given in Eq. 5.7.

$$X_{cross}(\nu_k) = \sum_{k=-i}^{i} T_{meas}(\nu_i) \cdot T_{sim}(\nu_i + \Delta\nu_k) \tag{5.7}$$

The obtained result corresponds to the similarity of the spectra as a function of the displacement $\Delta\nu_k$ of one relative to the other. It is thus similar to the convolution of two functions. The resulting function is maximum when both functions have the largest overlap. The respective value of displacement $\Delta\nu_k$ corresponds to the offset of the measured transmission spectrum.

Figure 5.8 shows 10 consecutively measured methane spectra without an offset correction and with the correction compared to a simulated HITRAN spectrum. The graphs reveal several characteristics of the acquired spectra: 1) the similarity of measured and simulated spectra is very high, 2) the measured spectra show only minor deviations among each other, 3) the determined offset obviously corrects the position of the spectra and is constant for all spectra, thus constant over a time series of consecutively measured spectra.

Especially the last point is of great relevance for the measurement of other gases and gas mixtures. A constant wavenumber offset signifies that also the spectral position of
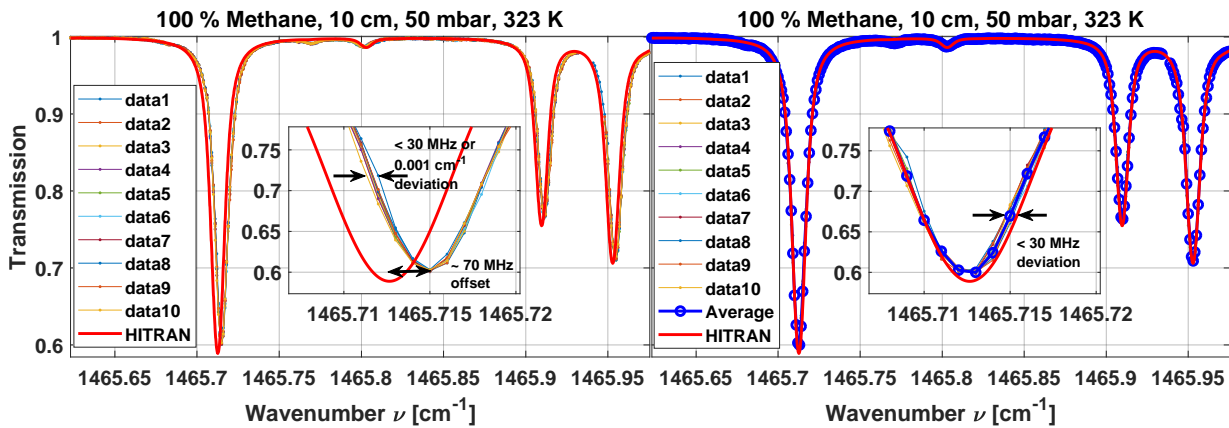
Figure 5.8: *Left:* Consecutively acquired methane transmission spectra without offset correction and simulated HITRAN spectrum; *Right:* Offset corrected spectra, average of the measured spectra and HITRAN simulation.

other gases can be corrected even when the exact comparison to simulated spectra is impossible due to unknown spectral parameters. In order to verify these findings the offsets for a longtime series of methane measurements over nearly a whole day was measured.

Figure 5.9 shows the variation of the wavenumber offset over time compared to the internal temperature of the wavelength meter. The temperature change and offset variation show a rough correlation. Within a time of approx. 3 hours the maximum drift of the offset
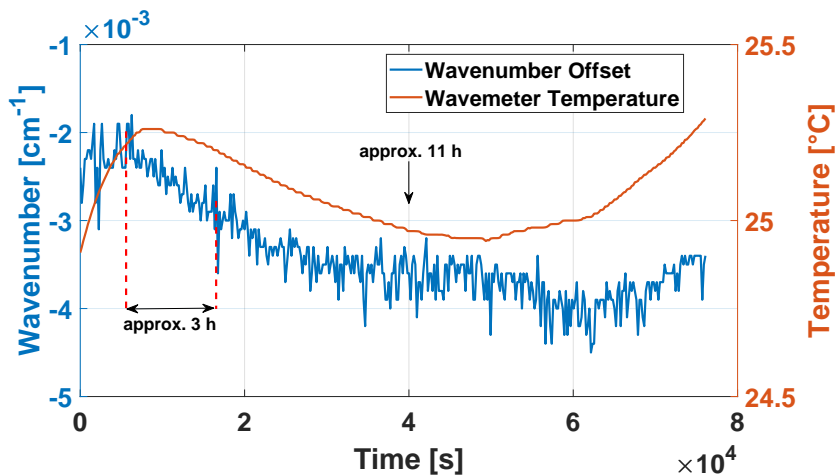
Figure 5.9: Variation of spectral offset for consecutively measured methane spectra during approx. one day. The spectral offset variation correlates with temperature changes in the wavelength meter.

is 0.001 cm^{-1}. Thus, for the later measurements the offset was determined by measuring a methane spectrum every 2 hours. In consequence we assume a spectral accuracy of $\pm$ 0.001 cm^{-1}.

5.4 Distortions of spectra

The generation of the spectra can be affected by several distortions and limitations in the system. Limitations that are induced by the system devices have been highlighted in previous sections. In consequence a measurement system design and a measurement procedure was developed to overcome limitations and reduce or identify incorrect operation. The operation procedure of the setup allows for broadband coverage and high resolution but simultaneously may generate measurement artifacts. The described signal processing procedure realizes a rejection of faulty data and correction of systematic errors.

However, signal distortion cannot be avoided in all cases despite the multiple measures. The main reason for accidental artifacts are back reflections into the laser that affect the emission. Back reflections can be effectively suppressed by exact alignment. But alignment is wavelength dependent and due to the broad tuning range and the need to use two EC-QCLs of the MIRcat an entire suppression is practically impossible. The main source for back reflections is the coupling IR fibre of the wavelength meter. The use of an angled fibre connector reduces the effect but cannot avoid it. The back reflections influence the laser emission leading to mode hops or multi-mode emission by the laser. It results in a possibly wrong wavelength measurement and leads to intensity distortions in the spectra. Figure 5.10 illustrates the effect.

Ten successively acquired methane transmission spectra are depicted. Two of the spectra are distorted due to back reflections at the same wavelength. During the measurements the alignment of the optical setup was unchanged. This shows the stochastic nature of back reflections that is due to the stochastic mode selection during the temperature stepping for the wavelength tuning, cf. measurement procedure in Fig. 5.1. Thus, averaging of several spectra is a possibility to reduce the influence of measurement artifacts. The averaging of the spectra reveals that the median average is advantageous compared to the arithmetic mean. The median corrects distortion when the majority of the spectra is not distorted while the arithmetic mean cannot revise the deviation but only reduce it, cf. Fig. 5.10.

Due to the challenging prevention of back reflections a visual inspection of the spectra is required to ensure that measurement artifacts have been discarded. In case of dominating distortions in the spectra the fiber coupler to the wavelength meter was realigned and the measurements repeated. Averaging not only serves for reducing deviation but to increase the sensitivity of the measurements by reduction of random noise. The estimated sensitivity of the measurements and the limits of averaging are discussed in the following section.
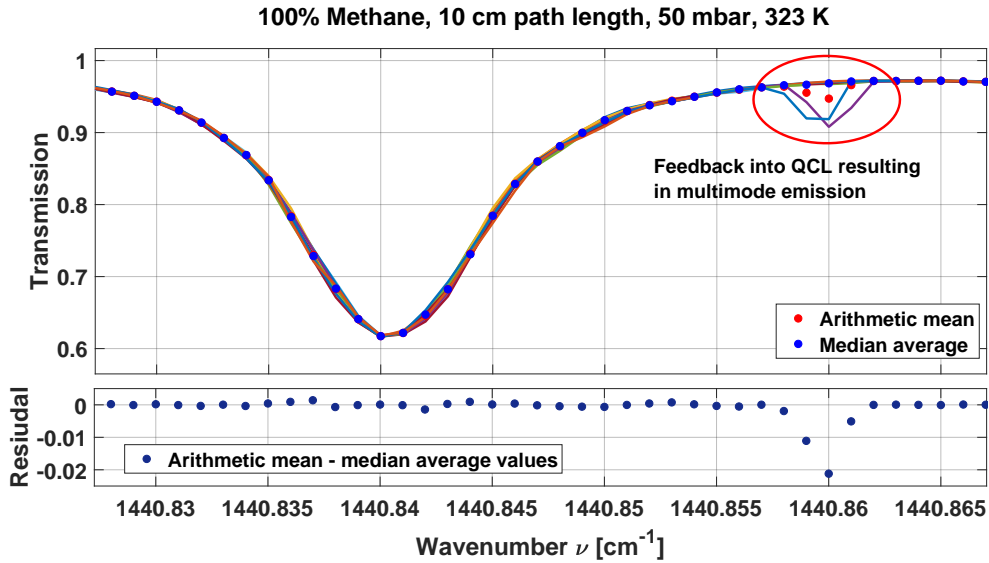
Figure 5.10: *Upper graph:* ten successively methane transmission measurements with spectral distortion in two spectra. Calculation of the arithmetic mean and the median average of the spectra reveals the median as advantageous to reduce distortion in averaged spectra.
Lower graph: Pointwise difference of arithmetic mean and median average.

5.5   Sensitivity estimation and Allan-Werle deviation

The sensitivity of spectroscopic gas detection is commonly specified by quoting the minimum detectable concentration of a target species [6]. This is especially useful for trace gas detection applications. But as this detection limit depends on the cross-section of the respective molecule this quantity makes comparison difficult between instruments that measure different species. As a more general figure for an instrument the minimum detectable absorption (MDA) or the noise equivalent absorption sensitivity (NEAS) of the measurements can be defined. These quantities are related to the 1σ standard deviation value of the limiting noise level of the measurement. In case of the MDA this value is normalized by the acquisition band width to a value unit of per $\mathrm{Hz}^{-1/2}$, which refers to the minimum detectable absorption for one second acquisition time of the measured signal. For wavelength scanned systems values in the scale of 10^{-4} $\mathrm{Hz}^{-1/2}$ for a MDA per scan are reported [87]. For the NEAS calculation the MDA value is additionally scaled to the absorption path length of the instrument which is of higher importance for cavity enhanced detection techniques with particularly long absorption paths which can scale up to several kilometers. The MDA value is than divided by this path length leading to values in the order of 10^{-11} $\mathrm{cm}^{-1}\mathrm{Hz}^{-1/2}$.

Regarding the presented system determining a general sensitivity of the measurements is challenging. As stated before the minimum detectable concentration is dependent on the targeted species and thus different for each of the seven investigated alkanes in

the measurements. In addition the molecule's cross section at a specific wavelength is also dependent on the measurement conditions as temperature and pressure that can be varied over a wide range in the setup. Furthermore, the wide tunability involves a wavelength dependent sensitivity due to wavelength dependent properties as transmission and reflection of the optical elements. The four different EC-QCLs imply variations in their beam characteristics which affects the alignment and their respective gain profile leads to intensity variations that influence the signal to noise ratio of the measurements. Also the responsivity curves of the detectors influence the results for example by leading to stronger fringing in the longer wavelength range due to a lower quantum efficiency in the active layer of the detector. Hence, the sensitivity of the setup depends on the measurement conditions and is wavelength dependent.

However, the targeted wavelength range for the investigated gases is comparatively narrow to the entire tuning range of the setup. Although, two EC-QCLs are required to cover the range from 1440-1480 cm^{-1}, which includes intensity and alignment variations, the deviations for the properties of the optical elements and detectors is less pronounced. In consequence the determination of a sensitivity limit relates to the specific measurement conditions. Nonetheless, an exemplary determination for the targeted wavelength range illustrates the limitations of the system even though the figures are not generally transferable to other wavelength ranges of the system.

Single spectrum sensitivity estimation A common approach to calculate the standard deviation of a spectrum is to fit the respective transmission curve and determine the residual between fit and measurement. Due to the limited knowledge in accurate line parameters and absorption cross sections for the targeted $C_1 - C_5$ hydrocarbons the measured spectra cannot be numerically modeled at the measurement conditions. The discussion in Section 6.1.2 highlights the specifications of the available databases and of the spectral data therein.

Therefore, the sensitivity of the measurements is estimated by a comparison of the measured etalon transmission with the fit of an Airy function to the data, cf. Eq. 4.4. For the transmission measurement the Germanium-Etalon that was described in Section 4.1.3 was employed. Due to its more precise end face parallelism of ≤ 0.5 μm and its physically smaller length of 1 inch the transmission of the Germanium-Etalon can be more accurately modeled with the Airy function than the transmission of the air spaced etalon where the parallelism is ≤ 1 μm and the physical light path 10 cm.

The upper graph of Fig. 5.11 depicts a fit of the Airy function to the measured etalon transmission data that was normalized to 1 at its peak transmission. The lower graph depicts the residual of signal and fit. By calculating the squared deviation of each transmission value from the Airy fit, subsequent averaging and taking the square root a root mean squared error of RMSE = 0.59 % is obtained. It is reasonable to assign the deviation of the etalon transmission to the gas transmission measurements as well. According to
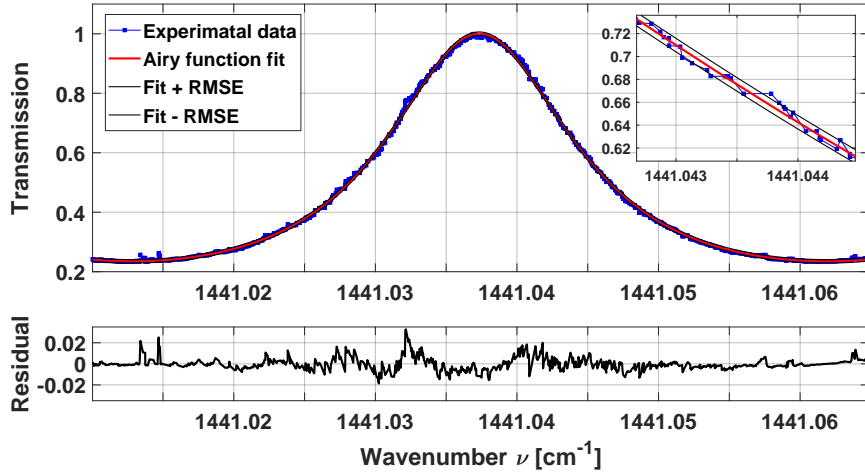
Figure 5.11: *Upper graph:* normalized transmission of the Ge etalon and numerical fit to the data; *Lower graph:* residual of the experimental data and the numerical fit.

the metrics discussed by Moyer *et al.* [87] a "per point" minimum detectable absorption (MDA$_{\mathrm{pp}}$) can be calculated for comparison to common instrument sensitivity data via

$$\mathrm{MDA_{pp}} = \frac{\Delta P}{P} \cdot \frac{1}{\sqrt{BW}} \ . \tag{5.8}$$

The term $\Delta P/P$ describes the limiting noise level ΔP of a measurement normalized by the total power P while BW corresponds to the sampling bandwidth that is given by the demodulation of the measurements. Accordingly, the RMSE is inserted for $\Delta P/P$ and 20 Hz for the bandwidth BW. This leads to a value of $\mathrm{MDA_{pp}} = 1.3 \times 10^{-3} \ \mathrm{Hz}^{-1/2}$ as per point minimum detectable absorption for 1 s acquisition time. This value compares well with other broadband spectroscopic techniques, cf. Table 5 in in Ref. [6]. The sensitivity is higher than for FTIR instruments due to the higher intensities that the EC-QCL can supply and in the same range or an order less sensitive than e.g. frequency comb based spectroscopy which is also laser based and broad range.

Tunable laser absorption spectroscopy (TLAS) with tunable single-mode laser sources, e.g. a DFB laser, can indeed achieve MDA$_{\mathrm{pp}}$ values that are two orders of magnitude lower, cf. assumptions for laser sources in Figure 2.6, and allow therefore much higher sensitivities as required for trace gas sensing. But these systems are optimized for a particular narrow wavelength range and a specific gas species. The wide tuning range from 6-11 μm of the developed setup comes along with reduced sensitivities compared to other TLAS measurement systems but simultaneously offers the valuable access to measure a multitude of species and absorption features while achieving higher sensitivities than FTIR systems and comparable sensitivities to other broadband approaches [6]. Notably, the considerable good sensitivity of the measurements gains special worth not only by the large spectral tuning range but also due to the high resolution and accruacy of the spectra,

cf. Section 6.1.

As outlined before the noise level of the measurements depends on several parameters that mainly vary with wavelength. The fitted etalon transmission in Figure 5.11 is a single spectrum where the acquired data points have not been averaged over equidistant wavenumber bins but only filtered for outliers. Analyzing the residual of measured data and fit reveals some not filtered outliers on the left edge and slight distortions of the transmission in the shoulders close to the peak of the transmission. In contrast in the far wings the residual is much lower. This illustrates that the MDA_{pp} value is affected by further structure on the signal than only white noise. Nontheless, reducing the noise level would also further decrease the MDA_{pp} and improve the sensing capabilities of the system.

Allan-Werle deviation Noise reduction is generally realized by averaging. The detection limit of gas concentrations in spectroscopic measurements by signal averaging can be determined with the Allan-Werle deviation [88]. The method was first proposed by Peter Werle in order to analyze the stability of an instrument for trace gas detection with the concept of the Allan variance [89]. It assumes that for short acquisition times a measured value is mainly perturbed by random noise. Averaging over a longer acquisition time should reduce the noise level according to a square root relationship when the system is white noise dominated. Thus yielding a higher measurement sensitivity. For further increasing acquisition times drifts in the system will dominate the result and reduce the sensitivity of the measurement. The square root of the variance corresponds to the deviation of the measured value and therefore to the detection limit. Equation 5.9 describes the Allan-Werle deviation:

$$\sigma_y(\tau) = \sqrt{\sigma_y^2(\tau)} = \sqrt{\frac{1}{2m} \sum_{n=1}^{m} (\bar{y}_{n+1} - \bar{y}_n)^2} \tag{5.9}$$

where τ is the averaging time and $\bar{y}_n$ the average of the nth sub-ensemble of successively measured values y and $\bar{y}_{n+1}$ the following sub-ensemble over the same averaging time τ. The integer value m is the number of measurements over the averaging time τ. For example for trace gas detection the concentration value of the gas species of successively measured spectra is determined by fitting. The concentration value can then by inserted for y into the equation and averaged for increasing number of values, thus an increasing averaging period τ. The minimum deviation of the time averages then indicates the detection limit of the measurements provided that the concentration is constant.

The investigated measurements of the hydrocarbon spectra and of their mixtures do not focus on trace gas detection of a single species but on realizing high accuracy reference spectra and the determination of mole fractions of several species in complex gas mixtures. Obviously, a lower noise level will increase accuracy, especially when determining small mole fractions in a mixture. But fitting of an isolated line to determine a concentration by the peak absorption value is not sufficient for these measurements. In particular for the large hydrocarbons a multitude of absorption lines overlap and form spectral bands of absorption. Hence, also the spectral shape over a broad range must show decreasing
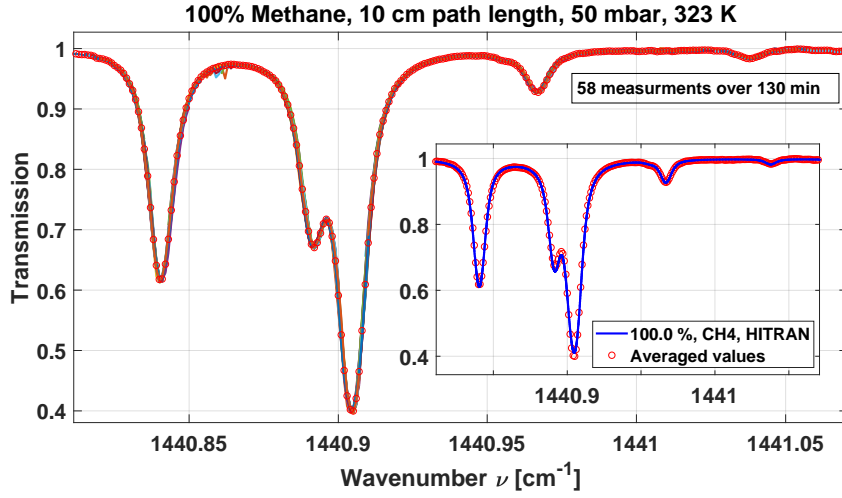
Figure 5.12: Consecutive methane transmission measurements for Allan deviation analysis. The inset compares the averaged values of all spectra to a spectrum that was simulated with line parameters from the HITRAN database.

deviations with increasing averaging time. Therefore, another parameter is required.

In order to determine the stability of the spectral measurements and the limits of noise reduction a longtime series of consecutive methane transmission spectra was acquired. Figure 5.12 shows a part of the acquired measurements.

The first spectrum was taken as reference. It is assumed that the reference spectrum S_{ref} equals to a consecutive spectrum S_n but for an exponential parameter a that corresponds to deviations in the spectral form and an exponential parameter b that corresponds to an offset of the baseline of the spectrum as given in Equation 5.10.

$$S_n(\nu) = I_n(\nu)\mathrm{e}^{-A_n(\nu)} = (S_{ref}(\nu))^a\mathrm{e}^b \tag{5.10}$$

S_n corresponds to the Lambert-Beer law with the incident intensity I_n and the absorbance of the measured gas A_n. This equation can be linearized by applying a natural logarithm on both sides of the equation:

$$\ln(S_n(\nu)) = a \ \cdot \ \ln(S_{ref}(\nu)) + b \tag{5.11}$$

In this way a and b become linear parameters in the equation system for all measured spectra S_n that can be solved. Both parameters are determined for each measured spectrum, peak normalized and analyzed by Equation 5.9 with $y = \{a, b\}$. Figure 5.13 shows the Allan-Werle deviation plot for both parameters for long averaging times.

Parameter a correlates with spectral shape deviations over consecutive spectra. It is therefore dependent on the cross-section variation of the measured gas species relative to the variations of the measured wavelength axis. In consequence it cannot be considered
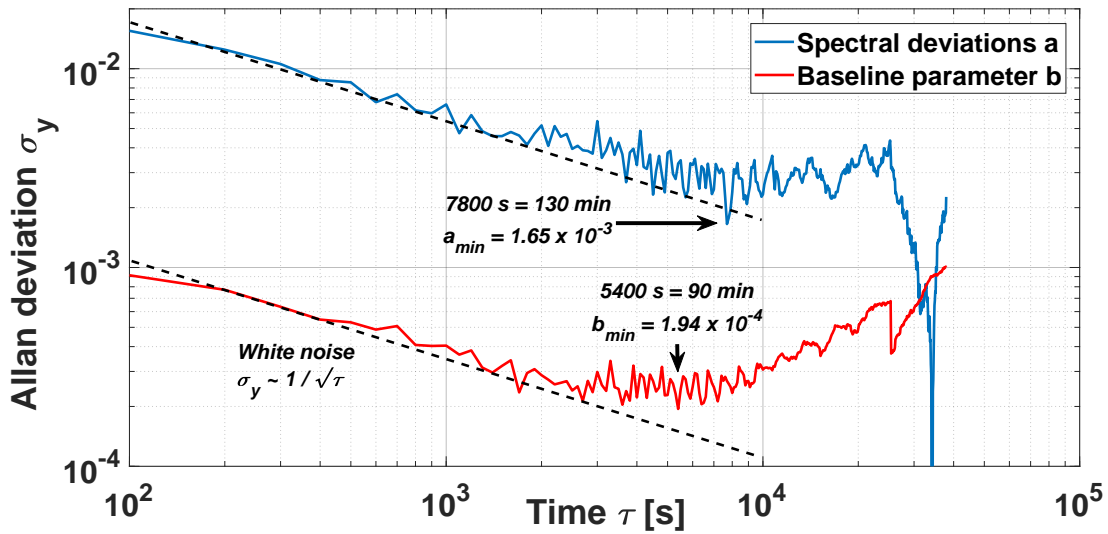
Figure 5.13: Allan-Werle deviation plots of the parameters a and b of methane transmission measurements. Parameter b corresponds to a noise-equivalent transmission of the spectral baseline. The minimum b_{min} of 1.94×10^{-4} is reached after 5400 s measurement time while an average plateau of 2.5×10^{-4} from 3000 to 7000 s indicates the reasonable measurement time for averaging. The subsequent drift is most likely due to temperature changes in the setup environment.

as value that corresponds to a general noise-equivalent absorption but rather allows for a conclusion on the deviations of the measured wavelength axis. Parameter b equals to a baseline drift of the measured spectra which is independent of the measured species. The deviation of both parameters decreases with averaging time and is compared to the trend of purely white noise averaging displayed by the dashed lines in the graph.

Due to the slow measurement procedure the acquisition of several spectra for noise reduction implies long averaging times. The minimum of the parameter a is reached after 130 min. This illustrates the stability of the wavelength axis linearization and the stability of the measurements as spectral shape deviations are mainly affected by white noise like deviations over more than two hours. However, the spectral shape may be also distorted by stochastic back reflections, cf. Section 5.4, and is generally dependent on the cross-section of the measured gas species. Thus, deviations of the wavenumber axis within its uncertainty of $\pm$ 0.001 cm^{-1} mainly influence this parameter. Nonetheless, the decreasing deviation over long averaging time of parameter a confirms the system stability but its minimum of 1.65×10^{-3} cannot be considered as a sensitivity limit of the instrument.

In order to understand the progression of the Allan deviation of parameter a after this minimum, it has to be considered that for longer averaging times the number of averaged sub-ensembles y_n decreases as they contain an increasing number of single measurements y. In consequence, the evaluation gets less stable as a smaller number of datapoints is employed to calculate the deviation. The abrupt and strong decline of the curve at

long measurement times is therefore a measurement artifact and not an indication of a pronounced decrease in the deviation of the measurement data.

The deviation of the baseline drift parameter b yields a minimum of 1.94×10^{-4} after 90 min total acquisition time. Thus, drifts in the system that are most likely due to temperature variations affect the baseline earlier than the spectral shape. The baseline deviation b is one order of magnitude smaller than a which explains an earlier impact of a drift in the system. However, the spectral baseline is independent of the measured species or measurement conditions and therefore corresponds to a general noise-equivalent transmission for the measurements at a specific wavelength range. Even though the minimum is reached after 90 min a plateau for averaging of the parameter b of approx. 2.5×10^{-4} from 50 to 120 min indicates the reasonable time for averaging.

The results illustrate the stability of the setup and the achievable noise limit by averaging. These findings impact in particular the acquisition of the reference spectra. According to the plateau of b all transmission spectra that are presented in the following where obtained by averaging of ten successively acquired spectra at a fixed grating position before tuning to the next wavelength. This procedure results in approx. one hour acquisition time per grating position for a spectral coverage of 0.5 cm^{-1}.

Chapter 6

Spectral measurement results and discussion

The acquisition of high resolution and high accuracy reference spectra form the basis for the discrimination of multiple species in a complex gas mixture. In the analysis of gas mixtures overlapping spectral features have to be identified and discriminated, cf. Fig. 2.4. This requires high measurement quality and high quality pure reference spectra which are not available for all targeted gases in the investigated wavelength range and for the chosen measurement conditions. The quantitative analysis of the spectra and the identification of spectral deviations is therefore limited by resolution and accuracy of the acquired pure reference spectra. A thorough investigation of these spectra is the prerequisite for the subsequent mixture analysis.

The objective of quantitatively measuring complex gas mixtures of up to 7 different alkanes is challenging. It requires

1. to study the pure gas spectra and identify strong spectral lines or bands that allow for sensitive quantification of a specific species and discrimination against others, cf. Section 6.1,

2. a stepwise investigation of collisional effects on the spectral shape starting with binary gas mixtures to identify mutual broadening, cf. Section 6.2,

3. to measure complex gas mixtures, correct for deviations due to spectral broadening and to identify the remaining deviations and limitations of the results, cf. Setion 6.3.

For a better discrimination of the measured spectra in a multi-component mixture it is necessary to reduce the line width of the spectra. The Lorentz width of a transmission line scales linearly with the gas pressure as described in the fundamental Section 2.1.2. Reducing the pressure leads to smaller overlap of the narrowly spaced lines and yields spectra with a more pronounced structure. This structure is essential for quantitative analysis of the mixtures. Concurrently, a lower pressure leads to a lower density of the gas and therefore to less absorbing molecules in the fixed path of the gas cell. As compromise between a resolved ro-vibrational structure of the spectra and sufficient gas density for high absorbances a gas pressure of 50 mbar was chosen for the measurements that are presented in the following.

First the measurements of the pure gas species will be presented and compared to the spectral databases which tabulate either line parameters or cross sections of the alkanes. The comparison serves for verification of the accuracy of the obtained spectra and to illustrate the limitations of the available databases. The subsequent section discusses the analysis of binary gas mixtures with the measured pure reference spectra and the effects of collisional broadening. Simplified approaches are evaluated to compensate for collisional broadening of the line width of the gases. The last section is intended to give an overview on multi-species gas detection in order to compare the results with the state-of-the-art of research and measurement technology before the spectral measurements and their evaluation will be presented and discussed in detail. A concluding summary of the results completes the chapter.

6.1 Pure gas reference spectra

For the acquisition of the pure gas reference spectra first a measurement range from 1440 cm^{-1} to 1480 cm^{-1} was identified to contain the strongest absorption features of the alkanes, especially for the absorption bands of the larger molecules $C_3 - C_5$. This region can be covered by QCL emission and was chosen for the more promising discrimination of the spectra in comparison to the 3 μm range as outlined in Section 2.1.1. The evaluation was based on the cross section data that is tabulated in the Pacific Northwest National Laboratory (PNNL) database [90]. The specifications of the database spectra and comparison to the measured spectra will be given later, cf. Section 6.1.2.

Accordingly, the first investigation of the spectra in this wavenumber range was done by the acquisition of non-averaged single spectra over the entire 40 cm^{-1} for all 7 gases. The spectra over the whole spectral range are depicted in Figure 6.1a and a close-up in 6.1b is shown to better reveal the spectral structure and distinguish the individual spectra.

Nearly gap-less spectra could be recorded but for some gaps in the emission of the EC-QCL. The gaps coincide with strong water lines in this spectral range. Therefore, they are attributed to residual water vapor in the ECs of the QCLs that alters the cavity losses and impedes emission in these wavelength ranges, cf. Fig. 4.12. However, the measurements allowed to reassess the spectra and identify the strongest absorption features of each gas.

A reduced range of three regions that cover in total 10 cm^{-1} was chosen for the acquisition of high sensitivity spectra for the evaluation of gas mixtures with the pure reference spectra, cf. Section 6.3. This decision was taken due to the long measurement times for the spectral acquisition of approx. 0.1 cm^{-1}/min. The objective of the measurements was to obtain spectra with a maximum sensitivity which includes averaging of consecutively recorded spectra for approx. 1 hour per EC grid position, cf. Section 5.5.

The acquired spectra reveal the differences of the ro-vibrational absorption bands for the different alkanes as already illustrated in the Fundamentals chapter. For methane multiple resolved or partially overlapped absorption lines can be identified. But with increasing molecule size spectral density of transitions rises forming a smooth overlapping absorption band, e.g. pentane. These first measurements also indicated the dynamic range of the
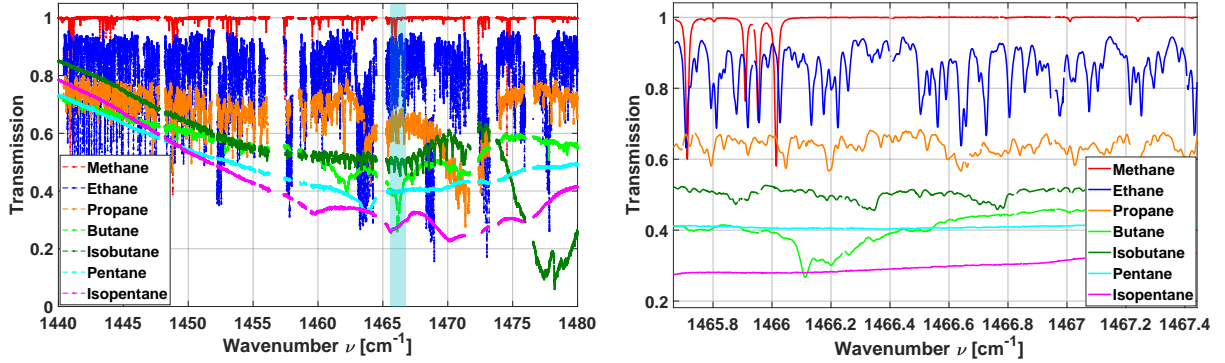
(a) Single spectrum acquisition of all 7 alkanes over the target wavenumber range from 1440 to 1480 cm^{-1}.

(b) Close-up (shaded spectral range in **(a)**) to show the rich structure of the measured pure gas spectra.

Figure 6.1: Transmission spectra of all 7 alkanes with 100 % concentration measured over a path length of 10 cm at 50 mbar gas pressure and 323 K gas temperature.

transmission signal yielding a minimum transmission of approx. 0.07 for the isobutane spectrum close to 1478.2 cm^{-1}. Longer path length or higher gas density would therefore lead to saturation of the signal. But concurrently a maximum transmission range, that covers ideally $0-100$ % of transmission, allows for higher sensitivity due to a higher signal to noise ratio.

The measurement conditions for the acquisition of the pure gas spectra and of the gas mixtures was generally set to a gas temperature of 323 ± 0.3 K and reduced pressure of 50 ± 0.25 mbar. Especially, the increased structure of the spectra due to the reduced pressure will become apparent for the comparison of the spectra to the tabulated database cross sections, cf. Section 6.1.2.

In the previous chapter a high resolution of 0.001 cm^{-1} and a accuracy of $\pm$ 0.001 cm^{-1} for the spectra acquisition was demonstrated. The accuracy of the spectral shape of the acquired spectra will be validated in the following Subsection by comparison of a measured methane transmission to a simulated database spectrum.

6.1.1 Accuracy analysis

The sensing of methane is of great interest for various fields of applications ranging from atmospheric research [91] to planetary remote sensing of exo-planet atmospheres [92] and industrial process gas analysis [2]. Therefore, the infrared spectrum of methane is by far the most extensively investigated and best documented of the seven targeted alkanes. Also due to its comparable small size theoretical models are well understood leading to a high congruence of measured and simulated spectra. This is a big advantage for this research as it allows to benchmark the measured spectra with simulated methane transmissions.

The line parameters of methane are tabulated in the HITRAN database [22] as already outlined in the signal processing section for the referencing of the wavenumber position
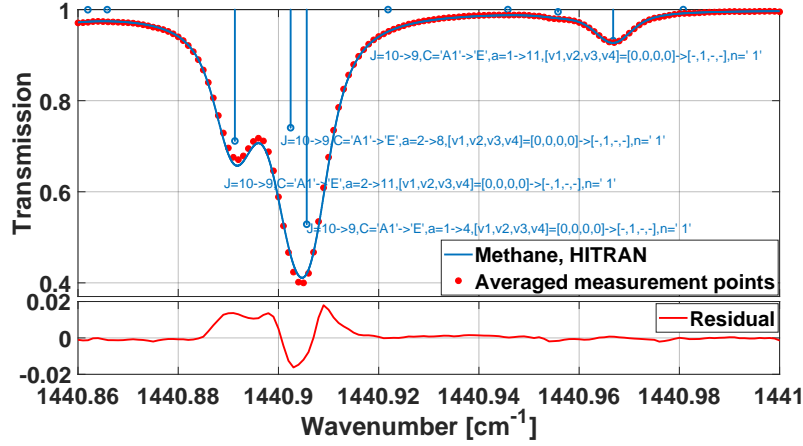
Figure 6.2: Comparison of the average of 40 successively acquired methane spectra and the HITRAN simulated transmission for this multiplet of the ν_2 band (*upper graph*). The notation of the ro-vibrational transitions is stated according to the HITRAN database. The residual is in the range of the database uncertainties for methane (*lower graph*).

of the acquired spectra, cf. Section 5.3.5. The methane parameters in the targeted wavelength range are specified to have an accuracy of the transition wavenumber position of $0.14 - 0.55 \times 10^{-3}$ cm^{-1} and relative line strengths intensity deviations in the range of 3 % to 5 % [85] for theoretical modeling of the spectrum. A more detailed presentation of the modeling of the spectra with the Voigt profile line shape function will be given in the subsequent Section 6.2.1.

The values of the relative line strengths deviations illustrate that for the modeling of the methane spectrum deviations have to be expected. These arise due to limited data for effects like collisional broadening, line mixing, speed dependence or collisional narrowing [93] which alter intensity and shape of the spectral lines. For more accurate modeling non-Voigt profile line shape functions are required. Other line shape functions, which consider the stated effects and allow to minimize shape deviations by further parameters, are a vivid field of current research [16, 94, 95] but not yet included in public databases.

Figure 6.2 shows the comparison of averaged measurements of the transmission of a methane multiplet compared to a spectrum that was simulated with the tabulated line parameters. The measurements were averaged for an acquisition of multiple spectra over two hours. According to the Allan-Werle deviation measurements this is the maximum average time to obtain a minimum deviation, cf. Fig. 5.13. In the upper graph the simulated spectrum is depicted as blue line and the respective line positions are given by vertical lines that are labeled with the line transition parameters of the database. The values of the averaged measurements are depicted as red points. The lower graph shows the residual of the measured minus the simulated spectrum.

The residual shows an obvious deviation in the range of $1 - 2$ % transmission at the

two main peaks of the overlapping multiplet lines. The baseline and the small side-peak at 1440.967 cm^{-1} show minor residual values. The residual is in the range of the outlined uncertainties of database line intensities and could be caused due to line mixing of the overlapping lines. In order to investigate the reasons for the deviation other line shape models should be applied which was not in the focus of this research. But the high congruence of the peak positions and the small residual for the side peak as for the baseline exemplify the high accuracy of the measurement wavenumber scale. It shows that the measurement setup and the evaluation method of the signals are capable of generating spectra with very high accuracy. A more detailed analysis would require a more sensitive and more accurate reference measurement system or more accurate database parameters. In consequence the measurement system can compare to state-of-the art quality of the database spectra in the targeted spectral range.

For the other alkanes the database parameters are different and not suitable to verify the accuracy of the measurements. But as the quality of the spectra could be demonstrated with the analysis of the methane spectrum the comparison of the other pure spectra illustrates the limitations of the database spectra for the $C_2 - C_5$ alkanes and the need for the acquisition of high resolution reference data.

6.1.2 Comparison to database spectra

Different databases for molecular gas absorption and emission have been established which include a large amount of line parameters and measured cross sections for a multitude of gas species over broad spectral ranges. These spectral compilations are continuously extended and improved, with respect to data coverage as well as to data accuracy. In order to name some of the most important databases: the GEISA [96], the HITRAN [22] and the PNNL [90] databases were created to serve for atmospheric research and remote sensing. In addition the HITEMP database [97] includes line parameters of small molecules at high temperatures for combustion gas sensing. For the targeted alkanes methane and ethane line parameters are covered by the HITRAN database and for propane to pentane cross section measurements are tabulated in the PNNL database.

While the methane documentation already achieves a very high level of accuracy, the investigation of the ethane spectrum is more complicated due to its large number of transitions. For the $C_3 - C_5$ gases the transitions and line parameters have not been determined, yet. Figure 6.3 shows several plots. In each axis a part of one measured alkane spectrum is plotted together with the scaled database spectrum.

The measured ethane spectrum will be analyzed more in detail in Subsection 6.2.2.2. But the graph in Figure 6.3 reveals already some major aspects of the simulated database spectra: 1) positions of the majority of lines are well known and coincide with the measured spectrum, 2) line intensities and widths of the simulated spectrum show obvious deviations compared to the measurements. The ethane line parameters in this spectral range were determined by di Lauro *et al.* [98] by high resolution Fourier transform infrared (FTIR) spectrometer measurements. In their results they emphasized that the line positions were measured with an absolute accuracy of ~ 0.0002 cm^{-1} and modeled with an average root
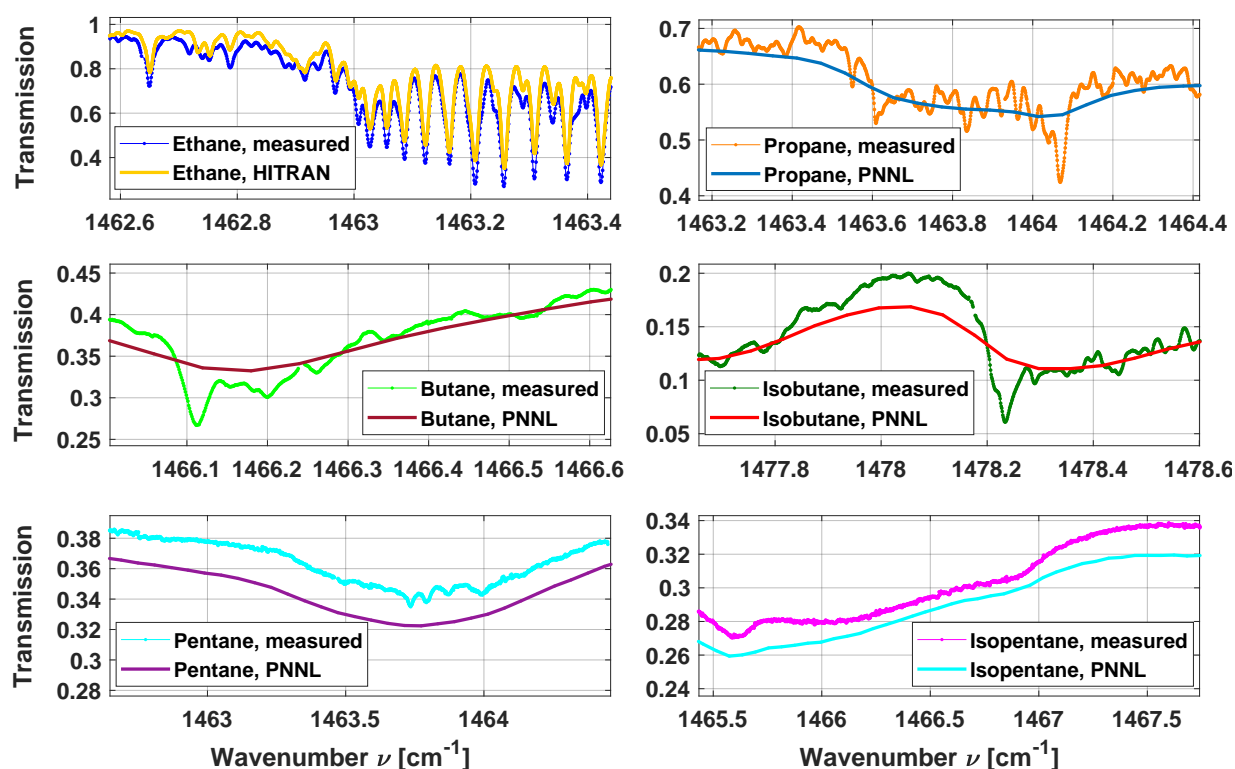
Figure 6.3: Comparison of small ranges for the measured $C_2 - C_5$ spectra with the scaled database spectra. The depicted wavenumber ranges were chosen due to prominent absorption features of the respective gas. Cf. Figure 6.1a for the assignment of the selected parts to the entire measured wavenumber range.

mean square error of ~ 0.004 cm^{-1}. For the modeling of the line intensities systematic differences of $10 - 20$ % should be expected dependent on the vibrational band and the respective transition. Hence, the database parameters are not suitable to model the ethane spectrum at the same accuracy as for methane.

For the $C_3 - C_5$ alkanes cross sections of the gases are tabulated in the PNNL database that were measured for a short path length of approx. 20 cm, at different temperatures (278 K, 298 K and 323 K) and for various concentrations at atmospheric pressure (760 ± 5 Torr). The spectra were recorded over a wide spectral range from 6500 to 600 cm^{-1} with a FTIR spectrometer with a resolution of 0.112 cm^{-1}. This is much less resolution than for the measurements presented here. In the database measurements the gases were diluted in ultra high purity nitrogen due to their strong cross sections in the MIR and for obtaining ambient pressure conditions. In consequence the spectra are pressure broadened by nitrogen yielding broad absorption features. At ambient pressure conditions the spectral shapes are well resolved with the resolution of the FTIR spectrometer and the nitrogen broadening corresponds to the conditions for trace gas measurements in the atmosphere. But for comparison to the measured 50 mbar spectra only the gas density

can be scaled to calculate the transmission level at reduced pressure while the pressure broadened shape remains. Due to the unknown line parameters a simulation of the transmission spectra for reduced pressure broadening is impossible.

Nonetheless, the comparison shows a good match of the transmission level of the measured and the scaled database spectra. The reduced pressure and therefore reduced pressure broadening reveals several partially resolved lines of the propane and the butanes that highly increase the structure of the measured spectra compared to the PNNL data. This structure allows for much better discrimination of superposed spectra in mixtures. The pentane spectra on the contrary contain such a multitude of lines that with exception for the peak transmission a rather smooth spectral shape is measured. It has to be emphasized that no comparable resolution for transmission measurements of theses gases have been documented in the literature before in this spectral range. This demonstrates the potential of laser spectroscopic measurements and especially the capabilities of the unique realization in the developed setup.

The transmission level of the pentane spectra show a small offset between the database and the acquired spectra. The possible reasons for this deviation can only be estimated. For the database spectra the pentane sample were diluted in nitrogen. A difference between nitrogen and self-broading should be expected but cannot be quanitified as the lines are unresolved. The database indicates a purity of > 99 % of the pentane samples while the pentane source for the here presented measurement should have a purity level of 99.5 %. In addition the PNNL database states possible deviations of ≤ 3 % for the measured transmission spectra. The highest deviation of the measurement conditions of the database spectra might result from the uncertainty of the pressure value of ± 5 Torr. Regarding the measurement conditions for the recorded spectra, pressure and temperature were controlled and stabilized to levels of deviation as indicated before.

6.2 Binary gas spectra

The investigation of the transmission spectra of binary gas mixtures allows to study the effects which are caused by collisional broadening. The set of 7 alkanes and nitrogen as non-absorbing buffer gas yields a large multitude of possible combinations of the gases. Already just all binary mixtures include 28 possible combinations without considering the possibility to have binary mixtures with different ratios of the two components. In order to reduce the measurements to a feasible amount the strongest broadening effects were examined. Thus the focus of the investigations was set on the resolved line spectra of methane and ethane. Nonetheless, measurements of binary mixtures for all gas species will be presented in the following.

First the approaches for the fitting of the spectra are outlined in Section 6.2.1 before the broadening effects are analyzed, cf. Section 6.2.2. All binary mixtures were prepared with the developed gas mixing unit that was presented in Chapter 3. The partial pressures of the gases in the binary mixtures were calculated with the AspenPlus software, cf. Section 3.2.1,

that employs the Peng-Robinson equation of state and considers the real gas properties of the alkanes.

6.2.1   Fitting approaches of gas transmission spectra

In the spectrum of a gas mixture the absorbances of the individual species superpose. The exact knowledge of the absorbances or cross sections of the pure gas spectra allows to discriminate the features of the gas components in the mixture for quantitative analysis. This implies that the mixture is measured in a wavelength range where the structures of the absorbances of the two components have significant differences. Otherwise the quantitative evaluation may be incorrect. This will be further emphasized by the later presented quantitative measurements of multi-component mixtures.

When the frequency positions of the transitions, the respective line strengths and the line widths under the pressure and temperature conditions of the measurement are known, the transmission profile of a single or several lines can be simulated. At ambient and moderately reduced pressures the Voigt profile is the most widely used model as it considers effects of Doppler and pressure broadening on the line shape, cf. Section 2.1.2.

Both approaches, measured absorbances/cross sections and simulated transmissions, were applied for the evaluation of measured gas mixtures. The basic equations that were used for the numerical analysis are briefly explained in the following.

6.2.1.1   Fitting with pure reference spectra

The spectrum of a gas mixture is composed of the superposed spectra of the individual species that scale according to their mole fraction in the mixture. As a first approach a simplified assumption can be made that the spectral shapes of the species' absorbances in the mixture is identical to the pure gas absorbance but for a scaling factor. Then the transmission of the mixture can be calculated according to the Lambert-Beer law. The pure gas spectra are scaled to the respective mole fraction in the mixture to generate a synthetic spectrum of a gas mixture. It should be emphasized that all gas spectra have to be acquired at the same temperature and pressure for this approach.

Equation 6.1 describes the Lambert-Beer law for the synthetic generation of a gas mixture spectrum. The measured transmission spectra of the pure species are given by $I_i(\nu_k)$. Taking the logarithm yields the absorbance of the gas that is scaled according to its mole fraction c_i in the exponent of the equation. This simple calculation allows to compose the spectrum of an arbitrary mixture $I_{\mathrm{mix}}(\nu_k)$ with n components while the sum of the mole fractions c_i must not exceed 1:

$$I_{\mathrm{mix}}(\nu_k) = \exp \sum_{i}^{n} c_i \ln I_i(\nu_k) \ . \tag{6.1}$$

For the quantitative evaluation of a measured mixture the mole fractions c_i of the components can be set as unknown parameters. They are determined by minimizing a

cost function χ^2 that is solved by a least-squares nonlinear curve-fit. Then $I_{\mathrm{mix}}(\nu_k)$ is the measured spectrum of a gas mixture with unknown components. The general cost function for n gas components is given in Equation 6.2:

$$\chi^2 = \sum_k \left[I_{\mathrm{mix}}(\nu_k) - \exp \sum_i^n c_i \ln I_i(\nu_k) \right]^2 . \tag{6.2}$$

The curve-fitting is solved by implemented routines in MATLAB that also allow for the determination of the confidence interval of the model parameters. Their calculation relies on the determination of the Jacobian matrix that is composed of the partial derivatives for each fitted model parameter at each point of the model vector. The Jacobian forms a linear approximation of the nonlinear model and can be used to determine the covariance matrix of the model parameters. This procedure is used to estimate the uncertainties of the fitted parameters. A brief description of the underlying maths is given in Appendix B. The fit results and a discussion of the obtained uncertainties are given in Section 6.3.2 for the multi-species gas spectra evaluation.

6.2.1.2 Fitting of Voigt profile line-shape model

The Voigt profile is well suited to describe the shape of a transition line as explained in the fundamental Section 2.1.2. With the respective database parameters the line spectrum of a gas can be simulated for the measurement conditions and compared to the measured transmission, cf. Section 6.1.1. In gas mixtures molecular collisions alter the line shape by changing the Lorentzian width of the transition. Fitting of the measured transmission reveals the deviation of the line width.

For the evaluation of the measurements the line spectra of methane and ethane were fitted to determine broadening coefficients in binary mixtures. The fitting routines have been developed in the research group before [99] and allow to simulate the transmission spectrum by either taking tabulated database parameters or defining values as line width, line position or line strength as fit parameter. Uncertainties are estimated with the computed variances as illustrated in Appendix B.

For the calculation of the Voigt profile the area normalized line shape $\phi_V(\nu)$ with the Gaussian width ν_G and the Lorentzian width ν_L is given by

$$\phi_V(\nu) = (\phi_L * \phi_G)(\nu) = \frac{\sqrt{\ln 2}}{\sqrt{\pi}\nu_G} \mathrm{Re} \left\{ w\left(\frac{(\nu + i\nu_L)\sqrt{\ln 2}}{\nu_G} \right) \right\} \tag{6.3}$$

where $(\phi_L * \phi_G)$ is the convolution of the Lorentzian and Gaussian line profils of the transition and w represents the Faddeva function [27, 32, 100]

$$w(z) = \mathrm{e}^{-z^2} \left(1 + \frac{2i}{\sqrt{\pi}} \int_{-\infty}^z \mathrm{e}^{t^2} \mathrm{d}t \right) = \mathrm{e}^{-z^2} \mathrm{erfc}(-iz) \tag{6.4}$$

that allows an analytical calculation of the Voigt profile.

6.2.2   Spectral broadening

In general the width of ro-vibrational transitions is altered by collisional interaction [16]. The magnitude of the collisional broadening depends on the respective transitions, the collisional partner and the environmental parameters as temperature and pressure. Hence, in binary mixtures the spectrum of both gas species is disturbed by each other. But depending on the gases the perturbation on its respective line shapes can be more or less pronounced. Overlapping and narrowly spaced transitions complicate the exact distinction of mutual broadening as line shape deviations can occur in both of the superposed spectra of the measured species. But depending on the investigated species strong isolated lines can be identified which allows investigations of the line broadening despite the overlapped spectra.

The evaluation of binary gas mixture transmission spectra revealed distinguishable line widths broadening for the individual species and could be quantified. In the case of an absorbing and a non-absorbing species the broadening of the line profile of the absorbing species can be directly analyzed. If both species absorb and lines are overlapped, spectral shapes have to be separated which is ambiguous and usually requires measurements at different pressures or even temperatures. For the here presented analysis of the hydrocarbon spectra the simplified assumption is made that for only one of the two species the line widths are changed by the other species. This means that for quantitative analysis the self-broadened pure spectrum of the other gas species is just scaled according to the Lambert-Beer law to match the transmission level that is given by its mole fraction in the binary mixture. Then the scaled spectrum can be practically subtracted as constant background from the binary spectrum and the broadening of the line shapes of the other species can be analyzed.

These assumptions led to the investigation of three "cases" for spectral broadening: (1) the broadening of the methane spectrum by other species, (2) similarly the broadening of the ethane spectrum and (3) the transmission spectra of binary mixtures of the heavier hydrocarbons $C_3 - C_5$. The obtained results and their inferences for the analysis of multi-component gas mixtures are presented in the following.

6.2.2.1   Simplified model for line spectra – The methane spectrum

The methane spectrum contains the fewest lines of the 7 alkanes which are mostly well separated at the reduced pressure of the measurements. Changes of the Lorentzian line width due to collisional broadening are therefore easy to verify. Figure 6.4 illustrates the broadening of methane lines for two perturber gases in a small section of the investigated wavenumber range for the gas mixture analysis.

The upper graphs a) and b) show the measured transmission of the pure gases, while graph c) displays the measured transmission of a binary mixture by the black line and by the red line the weighted sum of the transmissions from the pure gas spectra that were
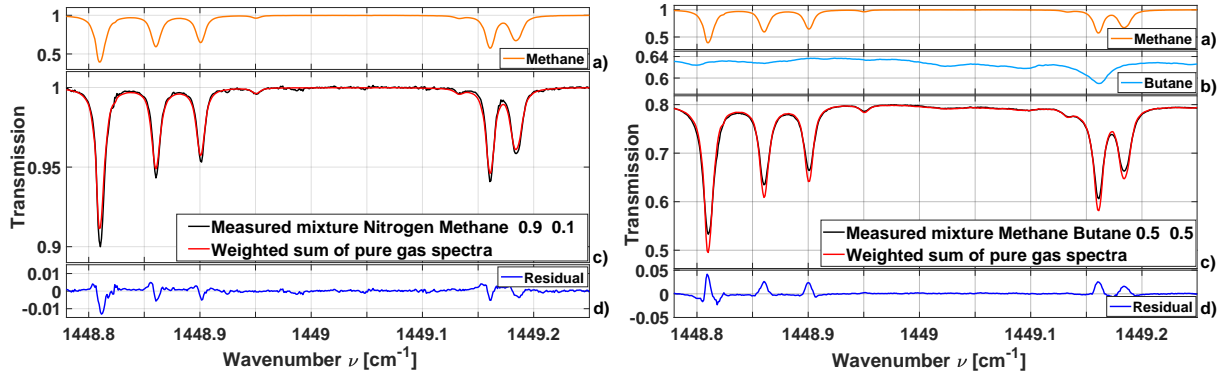
Figure 6.4: The diagrams depict the measured transmission spectra of the pure species in a) and b) (nitrogen is not absorbing in the mid-infrared) and the measured (black line) and calculated (red line) transmission spectra of the mixtures in c). The synthetic spectra are obtained by calculating a weighted sum of the pure spectra according to the Lambert-Beer law. The residual of measured and calculated spectrum in graph d) reveals the reduced and increased line broadening of methane in the respective mixture.

scaled according to their mole fraction in the mixture. The weighted sum was calculated as defined in the Lambert-Beer law, cf. Eq. 6.1. The synthetic spectrum neglects mutual line broadening in the mixture as the self-broadened spectra are scaled to the transmission level of their mole fractions in the mixture. But the residual in graph d) obviously shows a broadening of the methane lines. The residual was calculated from the pointwise difference of measured and synthetic spectrum.

The Lorentz width of the methane lines is reduced in a binary mixture with nitrogen. As the integrated area of the transmission and thus the sum of the absorbance is constant a reduced line width leads to larger peak value which results in negative dips in the residual of Figure 6.4 (*left graph*). On the contrary the line widths are broadened in butane which is illustrated by the inverse deviations of the residual in Figure 6.4 (*right graph*). While nitrogen is not absorbing in the MIR and therefore not depicted, the butane spectrum has a comparably smooth nearly constant transmission in this wavenumber range due to a multitude of overlapping lines. A broadening effect of the butane lines cannot be observed from this measurement.

The broadening of methane lines was investigated in numerous former studies as for example for the broadening of several lines of the $2\nu_3$ band around 1.64 μm [101–103]. Broadening and line shift coefficients were determined for methane in air and noble-gases, thus in perturber species that do not absorb at the measured methane lines. Zéninari *et al.* [101] compared the measured broadening and shift coefficients of the methane lines regarding the overall pressure, atomic mass and polarizability of the perturbing species. In general, they validated the linear increase of line broadening and line shifts with pressure and observed stronger broadening and larger shifts for perturbing species with higher atomic mass and higher polarizability. Broadening of hydrocarbons among each

other was not specifically analyzed in former research due to the difficulty of the superposed spectra. As outlined before the presented investigation of the methane spectrum was simplified by ignoring broadening effects in the perturber species. In addition for the evaluation an approximation of uniform line broadening was assumed due to the large spectral range of the measurements for the gas mixtures.

The parameters of transition lines are tabulated in HITRAN and as the line widths differ also the pressure broadening or pressure shifts are different for each line. Pressure shifts are ignored in these measurements due to the reduced pressure as outlined in Section 2.1.2. For the Lorentz width ν_L of a single line the following applies:

$$\nu_L(T, p, c, c_i) \ . \tag{6.5}$$

The parameter ν_L depends on the gas temperature T, pressure p and the mole fraction of molecules of its own species c and the perturber species c_i in a binary mixture. A common assumption is that the Lorentz width varies linearly with the gas concentration of the collisional partner. Therefore, the collisional width can be calculated by the self-broadened width $\nu_L(T, p, 100\%, 0)$ and the hypothetical width $\nu_L(T, p, 0, 100\%)$ for a molecule of the absorbing species that only interacts by collisions with the perturber molecules. The width $\nu_L(T, p, c, c_i)$ in a mixture with the mole fractions $c, c_i \neq 0$ can then be calculated by the respective line width limits scaled by the mole fraction of each component in the mixture:

$$\nu_L(T, p, c, c_i) = \nu_L(T, p, 100\%, 0)c + \nu_L(T, p, 0, 100\%)c_i \ . \tag{6.6}$$

The theoretical width $\nu_L(T, p, 0, 100\%)$ cannot be measured but due to the linear relationship a slope g_i for a perturbing gas species can be defined that alters the self-broadened line width dependent on the mole fraction and pressure of the gas mixture:

$$\nu_L(T, p, 0, 100\%) = \nu_L(T, p, 100\%, 0) + g_i p c_i \tag{6.7}$$

In Equation 6.7 the mole fraction c_i equals 1. Hence, by measuring the self-broadened line width and the collisional width in mixtures of varying mole fraction the line slope g_i of a perturber species can be determined and the line width $\nu_L(T, p, 0, 100\%)$ extrapolated.

In spectral databases it is common to tabulate a so called broadening coefficient γ_i which is the Lorentzian half width of a line at a reference temperature T_0 of normally 296 K, at atmospheric pressure p and given for the respective broadening gas species in units of cm^{-1}atm^{-1}.

This broadening coefficient was already introduced in Equation 2.25 and can be used to estimate the Lorentz width of a transition in gas mixtures. For the presented methane lines in Figure 6.4 the Lorentz widths were determined for the self-broadened lines by fitting of the Voigt profile to the measured transmission. The line widths in binary mixtures were determined for 0.1, 0.5 and 0.9 as mole fractions of the perturber species. The analysis was simplified as for all lines an equal perturber induced broadening of the self-broadened line

widths was assumed that scales with the decreasing methane mole fraction c and increasing perturber mole fraction, respectively:

$$\gamma_i = \gamma_{C_1} + (1 - c)g_i \; . \tag{6.8}$$

Equation 6.8 applies for a single line width γ_{C_1} while g_i corresponds to the respective perturber gas i. But g_i is assumed to be identical for all methane lines. The simplification was made to investigate in a first approach the overall behavior as measuring all transitions for the investigated 10 cm^{-1} in the range from 1440 cm^{-1} to 1480 cm^{-1} would imply to prepare the binary mixtures with the respective ratios for at least 20 different positions of the EC-QCL grid. In order to illustrate the measurement effort: one self-prepared mixture is sufficient for one hour of measurements, thus for one grid position. The preparation of a mixture takes one hour as well and the background measurement also one hour. Hence, measuring all lines for three different mixing ratios at 20 different grid positions requires 180 hours of measurement time for one binary mixture out of 7 different perturber species. Thus, as first approach the simplified model was applied. In addition, the approximation that the broadening of the lines is the same is reasonable as all rotational transitions belong to the same vibrational band ν_2, thus line widths and broadening coefficients are in the same order.

A comprehensive analysis of this vibrational band was done by Smith *et al.* [104] who determined multiple line parameters from high resolution FTIR measurements and their respective broadening coefficients in dry air and in pure methane. The broadening coefficients of the lines in Figure 6.4 were calculated and are compared to the results from [104] where the coefficients for three of the investigated lines were determined. The results are depicted in Figure 6.5 by plotting the values of the broadening coefficients on the y-axis over the molecular mass of the respective perturber species on the x-axis.

For higher clarity the mean values of γ_i of the methane lines are presented. In the fitting procedure the standard deviations of the self-broadened line widths were determined, the deviation of the linear slope parameter g_i and an uncertainty of the mole fractions of 2 % for the self-prepared mixtures was assumed as outlined in Section 3.2.3. These deviations were applied to calculate the error estimation of the coefficients in accordance with Equation 6.8.

In the study of Smith *et al.* uncertainties of 1 % are assumed for the half width coefficients. The mean half width for the determined broadening in nitrogen is 0.0606 ± 0.0012 cm^{-1}atm^{-1} and for self-broadening in methane the mean half width of 0.0726 ± 0.0011 cm^{-1}atm^{-1} was determined. This corresponds to a deviation of less than 4 % of the mean value compared to the air-broadened and smaller than 8 % for the self-broadened individual line widths that were ascertained by Smith *et al.* .

A deviation should also result from the elevated temperature of 323 K compared to the broadening coefficients in Ref. [104] that were determined for 296 K. The temperature dependence can be calculated with the line specific coefficient n_γ as introduced in Equation 2.26. On average a reduced half width of 9 % in air and of 2 % in methane should be expected. However, these values are also line specific and considering that the fitting of the line width was done in a simplified model by assuming an identical broadening
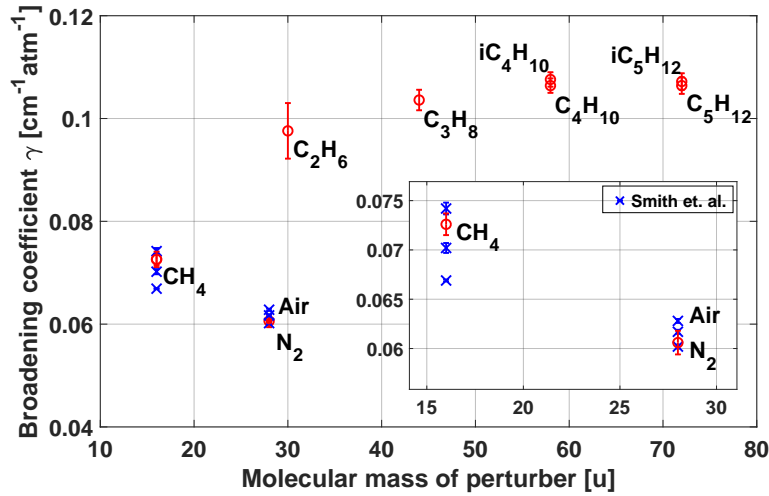
Figure 6.5: Average methane line broadening coefficients γ for self-broadening and different perturber gases. The broadening species is indicated by its chemical formula, and the values are sorted according to the molecular mass u of the perturber species. Previous results for the half width for self-broadening and broadening in air by Smith *et al.* for three of the investigated lines are depicted as crosses. The inset shows a magnification comparing their results to the determined mean Lorentz half width of the lines.

for all lines a reasonable consistency of the results can be concluded.

Regarding the general line broadening behavior of methane, for nitrogen as perturber the broadening of line widths reduces with increasing mole fraction, while it increases from C_1 to C_5 and saturates for the heavier hydrocarbons ($C_4 - C_5$). The broadening behavior among the hydrocarbons complies with the findings of Zéninari *et al.* [101] that perturber species with higher molecular mass lead to larger broadening coefficients of methane. Due to the reduced pressure no spectral shift of the lines was observed.

For the estimated uncertainties the highest deviations are found for the ethane broadening coefficient. This indicates that the approximation that only the methane spectrum is broadened neglects the broadening behavior of the perturber species in the mixture. Therefore, the broadening for a small range of selected ethane lines will be analyzed with the similar method in the following. The determined broadening coefficients for methane will be applied to correct deviations in spectra of gas mixtures and thus to improve the quantitative measurements of the methane mole fractions. The developed approach and obtained results are presented and discussed later in Section 6.3.2.

6.2.2.2   Database based pseudo line list - The ethane spectrum

Measurements of binary spectra revealed a broadening of partially resolved lines of ethane. In Figure 6.6 the spectrum of an example mixture for ethane and pentane is depicted. The spectra are given in the same order as for the methane mixtures before, cf. Fig. 6.4: the
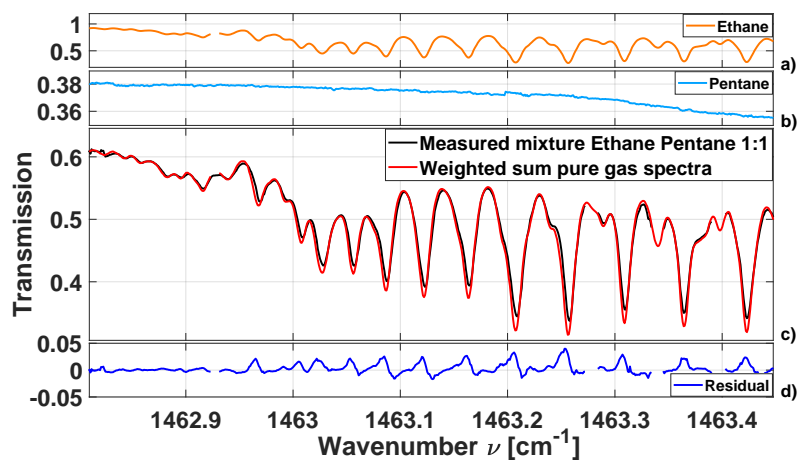
Figure 6.6: Pure gas spectra of ethane and pentane in the upper graphs a) and b). Comparison of measured 1:1 mixture (black line) and calculated spectrum (red line) in graph c). The residual shows a broadening of the partially resolved strong lines of ethane in graph d).

measured pure spectra are depicted in the upper graphs a) and b), the measured and the calculated mixture in graph c) and the residual of measured and calculated transmission is shown in graph d).

This exemplary spectrum demonstrates that the strong partially resolved lines of ethane between 1463 cm^{-1} and 1464.5 cm^{-1} are obviously broadened by the pentane in the mixture while the absolute residual values show much less deviations for the weaker unresolved lines at smaller wavenumbers.

Analyzing the ethane broadening is much more difficult. On the one hand many more strongly coupled lines overlap than for methane forming a dense and complicated spectrum and on the other hand line parameters have not been determined with the same accuracy as for methane, yet. Figure 6.3 already revealed differences for a part of the ethane transmission spectrum in comparison to the simulated spectrum that was generated with the tabulated line parameters from HITRAN [22] and Voigt profile calculation. The comparison of measured and simulated spectrum for a wider range and the residual of both are given in Figure 6.7.

As outlined before in Section 6.1.2 systematic deviations for the simulation of the ethane spectrum have to be expected [98]. Therefore, the tabulated parameters in HITRAN are only partially suitable to simulate the measurements. In order to analyze the general broadening behavior of ethane, the spectral range that is depicted in Figure 6.6 was investigated by determining "pseudo" line parameters. These "pseudo lines" could then be used to study the ethane broadening in mixtures.

The tabulated line positions of ethane are determined to a high accuracy while the line strengths and widths reveal larger deviations. But neither a simple scaling of the line strengths with a constant factor nor of the line widths yields appropriate correction. Hence, it was decided to simulate the spectrum with a so called pseudo line list. This concept tries
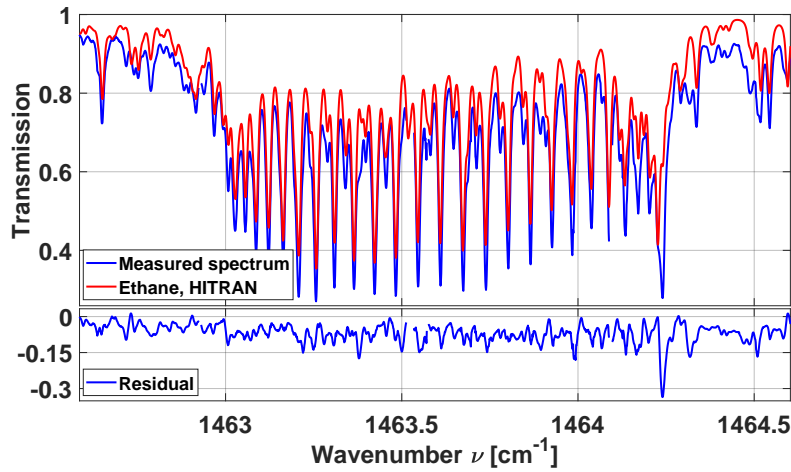
Figure 6.7: Comparison of measured and simulated ethane spectrum revealing large deviations in the residual of both spectra.

to reproduce the spectral shape with the simulation of physically reasonable line shapes as the Voigt profile but free parameters for line widths, strengths and positions. In the case of the analyzed ethane spectrum the tabulated line positions are taken as initial values but for the possibility of a small variation of ± 0.0015 cm^{-1} in the fit which is smaller than the estimated average deviations in the database (± 0.004 cm^{-1}) and only slightly larger than the precision of the measurements (± 0.001 cm^{-1}). Line strengths and line widths were set as free parameters in the fit. The spectrum was only fitted with the strongest lines of the spectrum, thus reducing the number of free parameters by taking only 28 of the 125 tabulated lines in the investigated wavenumber range. The pure ethane spectrum was measured at several pressures to reveal if the chosen pseudo lines can reproduce the measured transmission for varying measurement conditions.

Figure 6.8 shows the results of the analysis. In the upper graph the measured spectra (solid line) and simulated spectra (dashed line) of ethane for different pressure values are depicted. The residuals of measurement and fit are given below. In the lower graph the selected strongest lines that are tabulated in HITRAN are indicated with their line positions while on the left y-axis the Lorentz line widths ν_L values from the database are given as circles and on the right y-axis the line strengths cross section S are depicted as stars. The selection criterion was a minimum line strength cross section of $4.2 \cdot 10^{-23}$ cm^2/mol corresponding to approx. 3 % of the maximum line strength in the examined spectral range. Weaker lines have been discarded from the fit, cf. Appendix C for details.

The residual is significantly reduced in comparison to the former deviations of the measured spectrum and the simulated HITRAN spectrum, cf. Fig. 6.7. Thus for the various pressures the spectral shape can be reproduced except for some deviations. The still remaining deviations show the limitations of the method. The coarse selection criterion of neglecting weak lines for the fit fails at the smaller wavenumber range. The unresolved part of the spectrum cannot be reproduced with only the few strong transitions in this
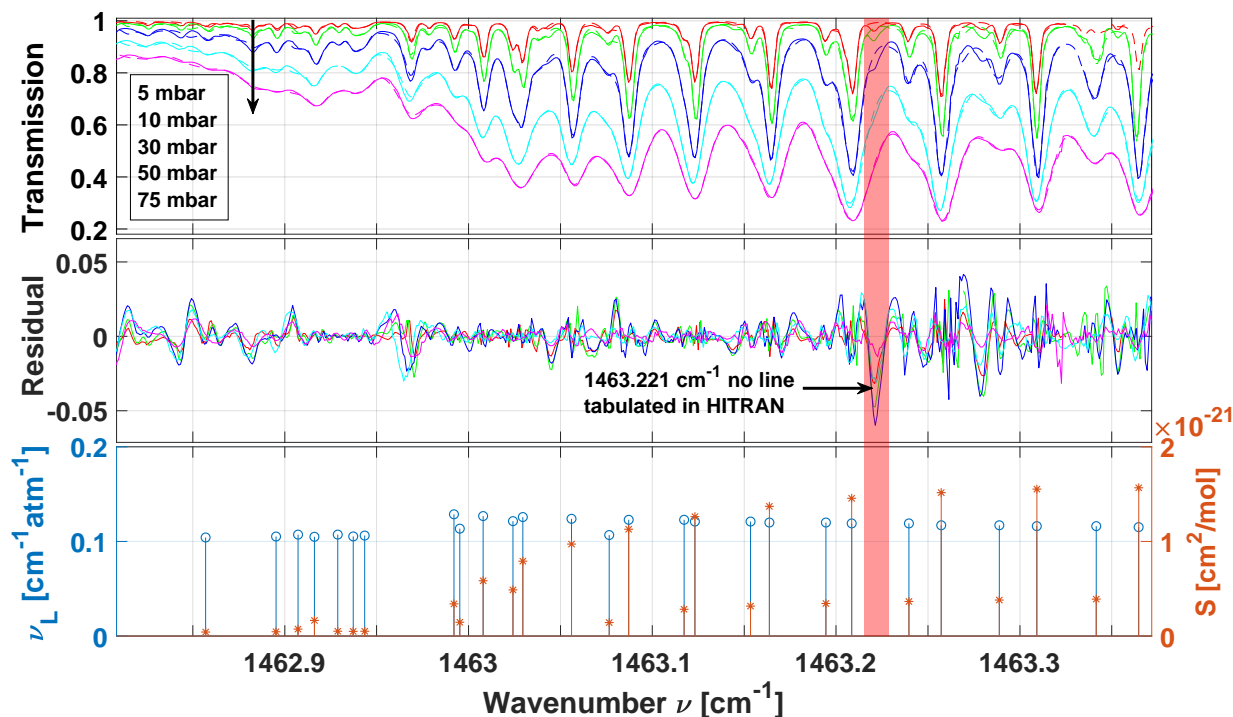
Figure 6.8: Fitted ethane spectra for various reduced pressures (*upper graph*), residual of measured and fitted spectra (*middle*), position, Lorentzian line width ν_L and line strength S of selected lines from HITRAN database for the fit (*lower graph*). In the red marked wavenumber range the maximum residual results from a transition line that is not tabulated in the database.

range. Another difficulty arises due to to undocumented transitions. In the figure the position of the strongest deviation in the residual is marked in red. The deviation results from a missing line that becomes visible for reduced broadening at lower pressure values ($p < 30$ mbar). This transition was not discarded in the line selection of the fitting procedure but is a line that is not tabulated in the HITRAN database. An analysis of the entire ethane spectrum between $1440 - 1480$ cm^{-1} reveals several missing lines also for the 50 mbar spectrum compared to HITRAN. This illustrates that despite the high accuracy of the line positions in the database and the great effort that has already been taken to generate this extensive and valuable compilation, a complete database is still subject of research.

As example for the differences between the tabulated and fitted Lorentz widths and line strength cross sections the respective values for one strong line of the spectrum at 1463.209 cm^{-1}are given in Table 6.1. It should be emphasized that the fitted pseudo values are not based on a physical model for the transition strengths but only adjusted to reduce the cost function in the least square fitting procedure. The deviations between tabulated and fitted values is large but could be expected. This is mainly due to the set of reduced lines of the pseudo line list which compensate the discarded weak lines in the spectra. But

Table 6.1: Comparison of fitted values for Lorentz width ν_L and line strength S to the HITRAN values and relative differences Δ for exemplary single line at 1463.209 cm^{-1}.

	Fitted value	HITRAN value	$\Delta[\%]$
ν_L [cm^{-1}atm^{-1}]	0.166	0.128	24.0
S [cm^2/mol]	$2.548 \cdot 10^{-21}$	$1.456 \cdot 10^{-21}$	74.9
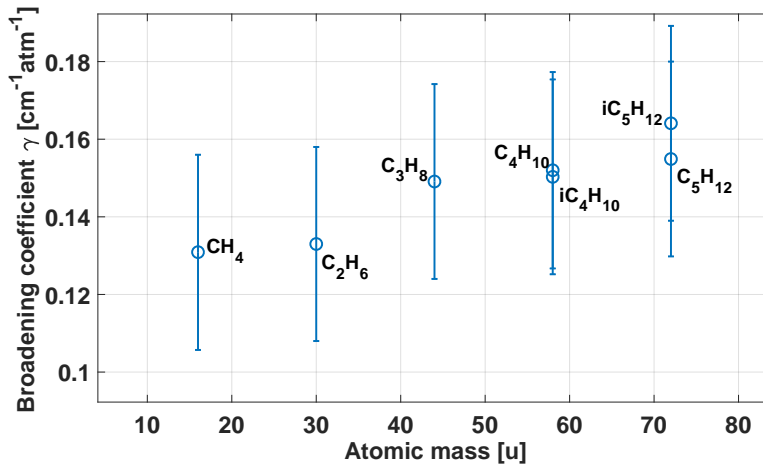
Figure 6.9: Mean "pseudo" broadening coefficients γ for selected strong lines of ethane perturbed by the other alkanes in investigated spectral range. The large relative uncertainties of $\pm$ 20 % emphasize the limitations of the evaluation method.

also the large residual that has been demonstrated for the measured and the simulated HITRAN spectrum, cf. Figure 6.7, reveals that the tabulated values must show strong deviations compared to fitted line parameters.

Nonetheless, the pseudo line parameters are generated with the Voigt profile model which considers pressure broadening in the line shape function by the Lorentzian line width value ν_L. The fit of the self-broadened ethane spectrum at different pressures could be demonstrated. Therefore, binary mixtures of ethane with the other 6 alkanes for the same ethane mole fractions as for the methane analysis (0.1, 0.5, 0.9) were measured. These mixtures have been evaluated with the determined pseudo line parameters of the self-broadened ethane spectrum at 50 mbar, cf. Fig. 6.8. For the evaluation of the collisional broadening of the pseudo ethane lines the same simplified assumption as for methane was made that all lines broaden identically and linearly with increasing perturber concentration, cf. Eq. 6.7. The obtained averages of the broadening coefficients of the ethane pseudo lines are depicted in Figure 6.9.

The estimated uncertainties are in the range of $\pm$ 20 % of the broadening coefficients.

This is much higher than for the determined values for methane and mainly caused by the large standard deviations that already result from the fit of the pseudo line widths to the pure spectrum. The values were determined with the experimental accuracy of the setup with a simplified evaluation method and limited data. They display the broadening behavior of these selected lines of ethane in a qualitative way. From these results it can be concluded that the ethane spectrum is only slightly disturbed by the presence of methane molecules in the mixture as the broadening coefficients are nearly identical. In addition for the broadening caused by C_3 to C_5 a smaller relative increase than for methane is found and probably also a kind of saturation of the broadening coefficients. But the high magnitude of the deviations and the simplified approach make it difficult to draw an explicit conclusion.

However, the deficiencies of the database parameters for the ethane spectrum were analyzed and a pseudo line list approach with selected real line positions could be applied to get a qualitative understanding of the broadening behavior of ethane. A more detailed analysis of the ethane spectrum would require measurements over a wider spectral range, for varying measurement conditions of temperature and pressure and a comprehensive physical model of the ethane transitions. All of these aspects have not been the focus of this thesis. But the qualitative results for the ethane broadening will be resumed for the discussion of the quantitative results in the evaluation of the multi-component measurements in Section 6.3.2.

6.2.2.3   Larger hydrocarbons $C_3 - C_5$

The analysis of the line broadening of the larger hydrocarbons $C_3 - C_5$ is first of all hampered by the unknown line parameters. In consequence the simulation of a spectral shape would entirely rely on pseudo line list approaches while no values for the line positions as for ethane or for line strengths and widths could be used as starting point. The reduced spectral structure due to the strongly overlapping transition lines for increasing molecular size also complicates an evaluation. Furthermore, the detailed analysis of binary mixtures for all 5 C_3 to C_5 alkanes, as it was done for methane and ethane, would include an enormous measurement effort of several weeks or even months, cf. estimation for methan lines in Subsection 6.2.2.1. Nonetheless, some exemplary binary mixtures were measured in order to verify the broadening of these hydrocarbon species. In the case of strong broadening effects these would have to be considered in the quantitative evaluation of the spectra of multi-component gas mixtures. As for methane and ethane the effects in the binary spectra allow to deduce the broadening effects for mixtures with several species.

For illustration purposes the graphical evaluation of a binary mixture of propane and isobutane is depicted in Figure 6.10. For the measurement the strongest absorption structure of isobutane and therefore the strongest absorption of all investigated alkanes in the targeted spectral range was chosen, cf. Fig. 6.1a. A distinct broadening is not obvious as the scale of the residual reveals deviations that are one order of magnitude smaller than that for the methane butane or ethane pentane mixtures. Concurrently, individual line broadening cannot be distinguished due to the unknown line parameters. Probably the effect is less distinct since it is simultaneously spread over numerous strongly overlapping
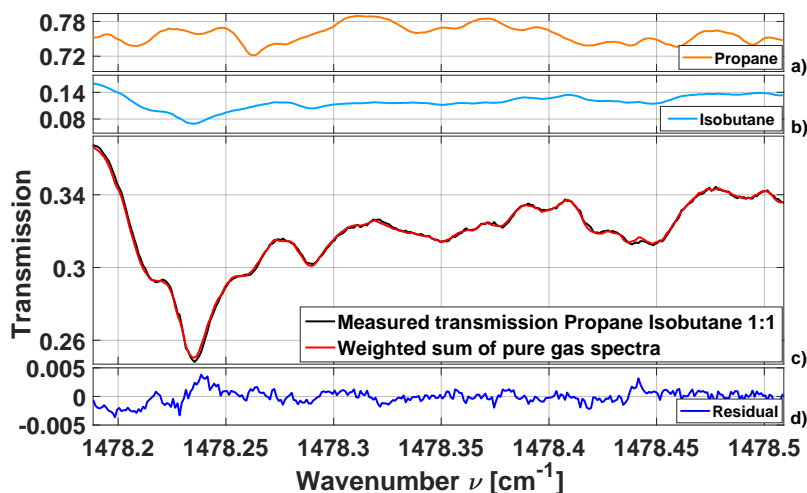
Figure 6.10: Pure gas spectra of propane and isobutane in the upper graphs a) and b). Comparison of measured 1:1 mixture (black line) and calculated spectrum (red line) in graph c). The residual in graph d) does not reveal obvious line broadening but only minor deviations that are one order of magnitude smaller than for the methane or ethane spectra.

lines, thus leading to no clear deviations in the residual of the spectra.

Comparable results were obtained for other binary mixtures of the butanes and pentanes. Presumably, weak collisional effects could be measured for propane as it has the most structured spectral shape and least overlapped transitions. But as the small deviations show that the effects are much smaller than for methane and ethane, a broadening of the $C_3 - C_5$ gases will be neglected in the analysis of multi-species gas mixtures. A more detailed analysis would require even higher measurement sensitivities and could be prospect of future research.

However, the results led to the conclusion that the broadening of the lighter molecules $(C_1 - C_2)$, which shows to be more pronounced and where the respective line positions are known, has to be considered for the quantitative analysis of multi-component gas mixtures. Their consideration is important for improving the quantitative discrimination of light hydrocarbon absorption features in spectra of complex mixtures.

The small deviations of the determined broadening coefficients for methane compared to former research of Smith *et al.* suggests that the results could be helpful to simulate the methane line broadening in gas mixtures. The strong uncertainties of the results for ethane and large deviations of the tabulated line parameters in HITRAN complicate the adoption of a comparable simple model for the broadening of the ethane lines. Even though, a collisional broadening should also be expected for the heavier alkanes, much weaker influences on their spectra were measured.

6.3 Quantitative analysis of multi-species gas spectra

In this section first an brief overview of state-of-the-art research on multi-component gas analysis will be presented and discussed. Then the results for the quantitative analysis of several multi-species gas mixtures containing all 7 alkanes will be presented and approaches to correct for the deviations due to spectral broadening of the methane line spectrum are discussed.

6.3.1 Overview and limitations

Laser based multi-species gas detection is of large interest for a multitude of fields of application as it promises fast and robust sensing capabilities, cf. Chapter 1. The investigation of the pure alkane spectra and of their binary mixtures revealed challenges that still remain for the quantitative sensing of hydrocarbon gases, e.g. untabulated transmission spectra at reduced pressure and missing or unknown line parameters as broadening coefficients. This section serves for giving a brief overview of the state-of-the-art of spectroscopic gas sensing of multiple components and for differentiating the chosen approach in this thesis from former research.

The spectral measurement of multiple gas species demands in most applications several or even all of the following measurement conditions: wide spectral coverage, high spectral resolution, high sensitivity and accuracy, high quality database spectra or the acquisition of reference spectra and in the case of non-atmospheric sensing composition dependent spectral broadening coefficients. Data in the today available spectral databases mainly tabulate self-broadening coefficients and line broadening in dry air or nitrogen.

Spectral coverage, sensitivity, resolution and accuracy rely on the measurement system while the latter aspects depend on the application or targeted gas species. As outlined before in Section 6.1.2 the detection of trace gas concentrations in ambient air or in higher layers of the atmosphere are a large field of research. Hence, present spectral databases were predominantly developed for atmospheric gas sensing. A recent review of mid-infrared tunable laser based broadband fingerprint absorption spectroscopy for trace gas sensing by Du *et al.* [105] summarizes the efforts and results that have been accomplished in the field over the last decade.

For a large spectral coverage in the mid-infrared EC-QCLs are preferably employed. The review of Rao *et al.* [58] covers trace gas sensing with this technology. Regarding multi-species trace gas detection with EC-QCLs the research of Phillips, Taubman and Brumfield from the Pacific Northwest National Laboratories has to be highlighted as they realized real-time capable systems for the simultaneous sensing of e.g. four fluorocarbons [106] or quantitative isotopic measurements of gas-phase alcohol mixtures [107] using broadly tunable fast swept EC-QCLs. Despite the excellent sensitivity and fast response of their measurements, fast swept EC-QCLs are limited in their spectral resolution due to the fixed external cavity length, cf. Section 2.3.2, which restricts their application to the detection of large molecules with broad unresolved band spectra.

Higher spectral resolution can be achieved with other laser systems that are continuously

tuned by current or temperature sweeps. A vast number or demonstrations exist. As one of the most recent demonstrations the realization of multi-species trace gas spectroscopy using dual-wavelength QCLs should be stated [108–110]. The technologies compromise dual section distributed feedback (DFB) QCLs, with two active regions designed for different emission wavelengths in a single waveguide, neighbor DFB QCLs, where two single-mode DFBs are placed next to each other with minimal lateral distance and electrically switchable laser devices with digitalized dual-frequency gratings, where the Vernier effect is used to switch between two frequencies. Multiplexing of these laser sources was demonstrated in a spectrometer to measure up to ten different compounds [108]. Despite the higher complexity due to the use of several laser sources, the small size of the lasers allows to realize the measurements in a single instrument.

To reduce the number of noteworthy findings in the field, this overview focuses on the approaches for hydrocarbon sensing in the following. Fast and sensitive detection of propane and butane was realized with a 3 µm FP QCL that served for leak detection thus also sensing of trace gas levels in ambient atmosphere [111]. A pulsed vertical external-cavity surface emitting laser also emitting in the 3 µm range was demonstrated to detect mixtures of the first four alkanes down to the ppm level with a resolution of 1.3 cm^{-1} [112]. The development of Interband Cascade Laser (ICL) [12, 39] based multi-mode absorption spectroscopy (MUMAS) [113, 114] revealed a method for simultaneous detection of methane, acetylene and formaldehyde in a gas mixture with relative uncertainties of 10 %. The method assumes stable laser operation and is limited when many absorption features overlap. Quartz enhanced photoacoustic absorption spectroscopy with an ICL was recently presented to be capable to detect trace gas levels of methane, ethane and propane in a single sensor [115, 116].

While all of these approaches realized high resolution and high sensitivity for trace gas detection, the sensing of hydrocarbons in trace concentrations at ambient conditions is different from the high concentration complex mixtures that are targeted in this thesis.

Due to their broad spectral coverage FTIR measurements are more often used to measure dense gas mixtures. MIR absorption spectroscopy with a FTIR spectrometer of gas-phase gasoline [117] revealed the capability to quantitatively discriminate five hydrocarbon classes based on reference spectra from the PNNL database. Quantitative on-line multi-component alkane mixture analysis with a FTIR spectrometer [118] was realized with 4 cm^{-1} spectral resolution from 400-4000 cm^{-1}. The system was tested in comparison with a gas chromatograph and the same gas set of alkanes as used in this thesis. In order to realize a detection range from 0 to 100 % sets of 6000 pre-mixed gas samples were employed to train a neural network. The physical effects of spectral broadening were not specifically analyzed in the published research. But due to the large training set broadening effects have to occur and are included in the training data of the neural network. With this approach quantitative on-line measurements could be realized. In the results relative errors for the individual gas species mole fractions in the range of $5 - 15$ % remain, depending on the species and its mole fraction level. Generally, the relative error decreases with increasing mole fraction of the species with this approach. But a relative error of ≤ 4 % for mole fractions above 60 % is still large compared to the

targeted absolute accuracy in the permille range of the research in this thesis.

Last but not least, Raman spectroscopy has to be mentioned as technology that targets the quantitative measurment of natural gas component mixtures [119]. Recent approaches are also data driven [120] for discriminating multi-species mixture. The mole fractions are either confined to certain ranges of concentration or larger relative errors in the $3 - 12\%$ range are obtained. Both, FTIR and Raman spectroscopy cannot realize the same high spectral resolution as tunable laser based spectroscopy but have the advantage of broad spectral coverage.

The approach in this thesis of high resolution measurements at reduced pressure with a slowly temperature tuned EC-QCL tries to combine the advantages of highly resolved and accurate laser based spectroscopy and broad band techniques [6] for the quantitative measurements of multi-species gas mixtures. The improved accuracy compared to the databases and the findings of the formerly not investigated collisonal broadening of the line spectra of the alkanes in binary mixtures is an advantage of the developed system. The obtained reference spectra and broadening coefficients for methane could be employed to realize highly accurate quantitative sensing of a mixture containing all seven alkanes [121]. A comparable measurement with laser based direct absorption spectroscopy has not been reported before.

The system was not designed for field use but for acquiring reference spectra and generating scientific knowledge about the behavior of the gases in complex mixtures. It therefore cannot be directly compared to real-time field applicable systems. But the approach of high resolution, high accuracy and broad coverage paves the way towards highly accurate analyzers that surpass the performance of the today available systems.

The results of the measurements of several gas mixtures and the developed method for the correction of methane line broadening in the spectra are presented and discussed in the following Section.

6.3.2   Multi-species gas spectra evaluation

For the quantitative evaluation of the measurement of gas mixtures with all 7 alkanes several custom-made gravimetrically manufactured gas mixtures from Linde Gas were employed. The mole fractions of the individual alkanes were set according to levels that occur in propane producing refinery process streams. Thus propane was the main component in the mixtures. In the following the results of an exemplary mixture are presented and the different evaluation methods are explained. Subsequently, limitations of the result accuracy for mixtures where the light hydrocarbons $(C_1 - C_2)$ compose the main mole fractions are demonstrated with the measurement results of further mixtures.

The results of the first mixture analysis and its discussion have been content of a publication, cf. Ref. [121].

Pure gas spectra fitting   The gas mixture was first analyzed with the acquired pure reference spectra. In the targeted wavenumber range from 1440 to 1480 cm^{-1} three regions

Table 6.2: Results of the transmission spectrum of a gravimetric manufactured gas mixture with the gravimetric mole fractions stated on top. The respective mole fractions and their errors were determined for different wavelength ranges (R1-R3) by a weighted sum of the measured pure reference spectra of the gas components, cf. Eq. 6.2. An error of < 0.05 % is indicated as $\pm$ 0.0 %. A penalty term in the evaluation guaranteed a value of 100 % for the sum of all mole fractions.

Gas species	Methane	Ethane	Propane	Butane	Isobutane	Pentane	Isopentane
Gravimetric mole fraction [mol/mol-%]	4.1 ± 0.1	4.2 ± 0.1	63.7 ± 0.2	10.1 ± 0.1	9.8 ± 0.1	4.1 ± 0.1	4.0 ± 0.1
Wavenumber range [cm^{-1}]	Determined mole fraction [mol/mol-%]						
1448 - 1479[*]	**4.1 ± 0.1**	**3.9 ± 0.0**	**63.9 ± 0.1**	**10.2 ± 0.1**	**9.8 ± 0.0**	**4.0 ± 0.1**	**4.1 ± 0.1**
R1: 1448 - 1450	3.7 ± 0.2	4.0 ± 0.1	63.6 ± 0.3	8.8 ± 1.2	7.6 ± 2.3	10.4 ± 3.5	1.8 ± 2.3
R2: 1462 - 1468	4.2 ± 0.3	3.8 ± 0.1	63.8 ± 0.1	9.6 ± 0.1	10.9 ± 0.2	3.5 ± 0.2	4.2 ± 0.2
R3: 1477 - 1479	2.0 ± 2.6	4.3 ± 0.1	64.0 ± 0.5	12.0 ± 1.3	9.5 ± 0.2	4.8 ± 1.9	3.4 ± 0.3

[*]simultaneously evaluating all three sections R1-R3, summed up to 10 cm^{-1} in total

with the most characteristic features of the gases were selected. This selection reduces the covered wavenumber range for the mixture analysis to approximately 10 cm^{-1} in total, cf. Table 6.2.

The results were obtained by minimizing the least square cost function χ^2 between the measured gas mixture spectrum $I_{mix}(\nu_k)$ and a weighted summation of the measured reference spectra $I_i(\nu_k)$ according to the Lambert-Beer law, cf. Eq. 6.2. The resulting weight with a 95 % confidence interval as uncertainty of the fitting procedure corresponds to the mole fraction c_i of each component. A penalty term was added to coerce the sum of the mole fractions to 100 %. This is valid for a first approach with a calibrated mixture where the mole fractions are known to be $\sum_i c_i = 100$ %.

In Table 6.2, the determined mole fractions for this evaluation method are given. In the first line, the mole fractions of the components in the gravimetrically manufactured mixture are stated with their respective uncertainties[1]. In the lines below, the results are given first for the entire measurement range covering the three selected parts and then for the individual sections R1-R3.

We achieve an absolute deviation of ≤ 0.3 % from the gravimetric mole fraction values when all three sections are covered. By just measuring the first section R1 in the range from 1448 to 1450 cm^{-1}, one can obtain good results for the $C_1 - C_3$ alkanes since they have characteristic absorption lines in this range, cf. Fig. 6.1a. On the contrary, the transmission spectra of $C_4 - C_5$ do not have characteristic features in this range but form a smooth background. As a consequence, the least square algorithm fails to determine these

---

[1] Gravimetric values and uncertainties for gas mixture with lowest manufacturing tolerance (PEH) according to the supplier Linde Gas.
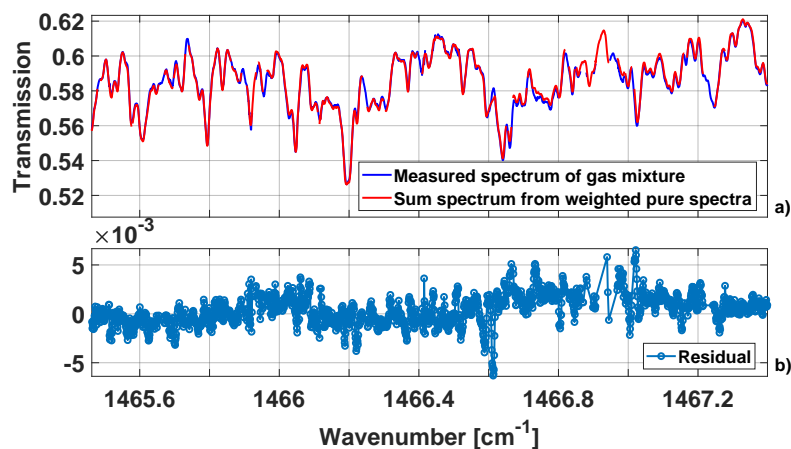
Figure 6.11: (a) Measured transmission of calibrated gas mixture and scaled transmission from pure gas reference spectra in exemplary range of the analyzed 10 cm^{-1}. (b) Residual of measured and weighted spectrum.

components by simply scaling their pure transmission spectra and yields strong deviations and large errors for the determined mole fractions. In a similar way, one can interpret the results for section R2 covering 1462-1468 cm^{-1}. First, three times more information for the spectra can be evaluated and second, all gases have characteristic features in this range. Consequently, the determined mole fractions are much closer to the calibrated values but still less exact than the results when all regions are evaluated. Wavenumbers 1477-79 cm^{-1} emphasize again that for C$_5$, the spectra are very similar and thereby difficult to discriminate. In addition, C$_1$ has no strong absorption lines in this range , which is why the relative error is pretty large. Last but not least, it becomes evident that ethane and propane are determined with the smallest deviations for all three sections, which is due to their strong spectral features over the entire wavenumber range from 1440 to 1480 cm^{-1}.

The comparison of these results emphasizes the necessity of covering characteristic spectral features of all gases for getting the smallest deviations. In order to illustrate the remaining residual between measured and weighted sum of the pure spectra, a close-up of the spectrum is depicted in Figure 6.11. In the upper graph a), the measured transmission of the gas mixture (blue) is plotted together with the scaled transmission from the pure spectra (red). The graph b) below shows that the residual of both spectra is predominantly $\leq 5 \times 10^{-3}$.

These findings demonstrate the high accuracy that can be obtained by the analysis of the spectra at low pressure and with high resolution reference spectra. But as outlined in Section 6.2.2, a broadening of the lighter hydrocarbons has to be expected, which should lead to faulty results for their determined mole fractions. This broadening was ignored in the evaluation, yet. The reason for no evident deviation, especially for methane, was the penalty term that forced the sum of all concentrations to be 100 %. Such a boundary condition might be reasonable for a calibrated mixture where other gases can be excluded.

But if unknown mixtures are evaluated, a penalty term can cause systematic errors in the evaluation. In addition, one obtains a distortion of the determined mole fractions as, for example, methane contributes with the smallest number of lines to the entire spectrum. Therefore, it induces the least error when its mole fraction slightly deviates.

Hence, in the following the results of the evaluation without a penalty term will be presented and a method for considering the line broadening of methane introduced.

Evaluation with simulated methane broadening The results for the evaluation without a penalty term are given in Table 6.3. The sum of the mole fractions equals to 98.5 %. Overall, the deviations for $C_2 - C_5$ are in the same range as before or slightly increased as for propane. The most obvious deviation can be ascertained for methane with a value of 0.5 % below the calibrated mole fraction. This result should be expected as a broadening of the methane lines in the mixture occurs. Consequently, a smaller peak absorbance has to lead to a smaller mole fraction value when the self-broadened reference spectrum is taken for the evaluation.

In the fundamental section the collisional Lorentz line width of a transition was introduced in Equation 2.25. For the analysis of the broadening coefficients γ_i of methane in Section 6.2.2.1 an average broadening coefficient for each perturber species was obtained. In order to estimate the broadening of the lines in the gas mixture a mole fraction weighted mean broadening coefficient γ_{mean} can be calculated by summation of the product of the known calibrated mole fractions χ_i and the determined broadening coefficient γ_i of each perturber species:

$$\gamma_{mean} = \sum_i \chi_i \gamma_i \ . \tag{6.9}$$

By taking the ratio of this mean broadening coefficient γ_{mean} of methane in the mixture to its self-broadened value γ_{C_1} one obtains an average broadening of 141 % of the methane lines:

$$\frac{\gamma_{mean}}{\gamma_{C_1}} \approx 1.41 \ . \tag{6.10}$$

The accuracy analysis in Section 6.1.1 revealed a good accordance of the measured reference spectrum and the simulated transmission with the HITRAN line parameters. Therefore, the tabulated line parameters can be used to simulate the transmission of methane in the mixture. The Lorentz width of each line is scaled by the gas pressure of 50 mbar and by the broadening coefficient ratio of 141 %, cf. Eq. 2.25. This simulated spectrum can than be taken together with the measured reference spectra of the other alkanes to repeat the determination of the mole fractions of each gas species.

The results are given in the second line, "Methane spectrum simulated", of Table 6.3. The obtained mole fractions stay unchanged but for methane. With the synthetic broadened spectrum, a methane mole fraction of 4.0 ± 0.2 % was determined, which is within the range of the calibrated mole fraction value of 4.1 ± 0.1 %. A weaker broadening of the simulated spectrum yields smaller values and a stronger broadening leads to higher results for the methane mole fraction.

Table 6.3: Results for the gas mixture without a penalty term in the evaluation. The results for a weighted sum with a self-broadened reference spectrum of methane and with a simulated methane spectrum, that considers the line broadening by the mole fractions of the perturber gases in the mixture, are stated. The methane mole fractions highlighted in bold emphasize that smaller deviations can be achieved when the line broadening is considered.

Gas species	Methane	Ethane	Propane	Butane	Isobutane	Pentane	Isopentane
Gravimetric mole fraction [mol/mol-%]	4.1 ± 0.1	4.2 ± 0.1	63.7 ± 0.2	10.1 ± 0.1	9.8 ± 0.1	4.1 ± 0.1	4.0 ± 0.1
Measurement evaluation method	Determined mole fraction [mol/mol-%]						
Methane spectrum measured	$\mathbf{3.6 \pm 0.2}$	3.9 ± 0.0	63.3 ± 0.1	10.1 ± 0.1	9.5 ± 0.0	3.9 ± 0.1	4.2 ± 0.1
Methane spectrum simulated	$\mathbf{4.0 \pm 0.2}$	3.9 ± 0.0	63.3 ± 0.1	10.1 ± 0.1	9.5 ± 0.0	3.9 ± 0.1	4.2 ± 0.1

The results reveal that the methane spectrum is broadened in the mixture and that the simulation of the methane spectrum with an average broadening coefficient γ_{mean} is suitable to correct the deviation in this case. This analysis still neglects that the other spectra, as for example ethane, are broadened as well. Also, for some gases the deviations between determined mole fractions and the calibrated values of the mixture are larger than the uncertainties and the confidence interval of the fitted value is smaller then these deviations. This emphasizes that systematic errors on the spectra, as a broadening of the spectral shape occur.

The preceding analysis showed that spectral deviations also for ethane have to be expected. Similarly, deviations for the $C_3 - C_5$ should be small but cannot be excluded. Further investigations of binary mixture over the whole analyzed wavelength range would be necessary to better quantify the broadening behavior. Also measurements at other pressures, temperatures and path length would contribute to a more detailed evaluation of the optimum conditions for complex mixture sensing of the alkanes. However, in this exemplary mixture as in further mixtures with propane as main component and small mole fractions of methane and ethane the correction of the methane broadening by simulation of a synthetic broadened spectrum could be verified. It emphasized that the main shape deviation due to collisional broadening occur on the methane spectrum and that the larger hydrocarbons are less affected, as already deduced from the binary mixture analysis.

Laser-based measurements of a seven component alkane gas mixture with a comparable accuracy as presented here has not been reported, yet. This demonstrates the potential of the measurement method and the high quality of the spectra.

The chosen approach of only considering the broadening of the methane spectrum can be tested to demonstrate the limits of the method. In the following, the synthetic simulation of the methane line broadening will be used to estimate the deviations of the mole fractions in a mixture analysis before the spectral measurement. The evaluation assumes that the other spectra are not broadened, thus can be removed as static background in the mixture

by simply scaling the respective reference spectra. Then, the estimated deviations will be compared to the measurements of three calibrated gas mixtures with high concentrations of methane and ethane.

Deviations in mixtures with high mole fractions of C_1 and C_2   In Section 6.2.2.1 the linear dependence of the Lorentz width of the methane lines on the mole fraction of a perturber species was used to determine mean broadening coefficients γ_i. The application of these broadening coefficients to simulate the average broadening of the methane spectrum in a gas mixture could be demonstrated. Assuming that only methane is broadened in the mixture allows to estimate the deviation for the determined methane mole fraction by comparing the self-broadened and the simulated methane spectrum.

When the shape of other gases in the mixture would be unchanged, the deviation of the methane mole fraction results only from the neglected methane line broadening. Analyzing the mixture spectrum with the self-broadened methane spectrum yields a systematic error. This assumption allows to estimate the deviation dependent on the mixture broadening coefficient γ_{mix} and the methane mole fraction c by simulating the broadened methane spectrum with the tabulated HITRAN line parameters and fitting the pure self-broadened reference spectrum to the simulated spectrum. The obtained weight c_{fit} is an estimate for the mole fraction that results when a broadened methane spectrum is analyzed with the self-broadened spectrum.

Thus the relative deviation Δ_{rel} and the absolute deviation Δ_{abs} for the determination of the methane mole fraction can be calculated:

$$\Delta_{rel} = \frac{c_{fit} - c}{c} \qquad , \qquad \Delta_{abs} = c_{fit} - c \ . \tag{6.11}$$

For example, by scaling the simulated methane spectrum of the former mixture evaluation to the calibrated 4.1 % mole fraction and fitting the curve with the self-broadened reference spectrum reveals a relative deviation of 11.7 % and an absolute deviation of 0.5 %. These values correspond exactly to the measured deviation of the evaluation with the self-broadened reference spectra, cf. Table 6.3.

The broadening coefficient γ_{mix} is dependent on the methane mole fraction c, the broadening coefficient of the perturber gas γ_{C_x} and the methane broadening coefficient γ_{C_1} as given in Equation 6.12:

$$\gamma_{mix} = (1 - c)\gamma_{C_x} + c\gamma_{C_1} \ . \tag{6.12}$$

In Figure 6.12 the estimated deviation for the fitting of the methane mole fraction is depicted for increasing methane concentration. The relative deviation Δ_{rel} decreases with increasing methane mole fraction. The broadening coefficient γ_{mix} reduces until for 100 % the simulated self-broadened spectrum from the HITRAN database is fitted with the measured self-broadened spectrum. But the absolute error increases first with increasing methane content in the mixture until it reaches a maximum and then decreases again. The non-zero deviation for $c = 100$ % illustrates the deviations that remain between the
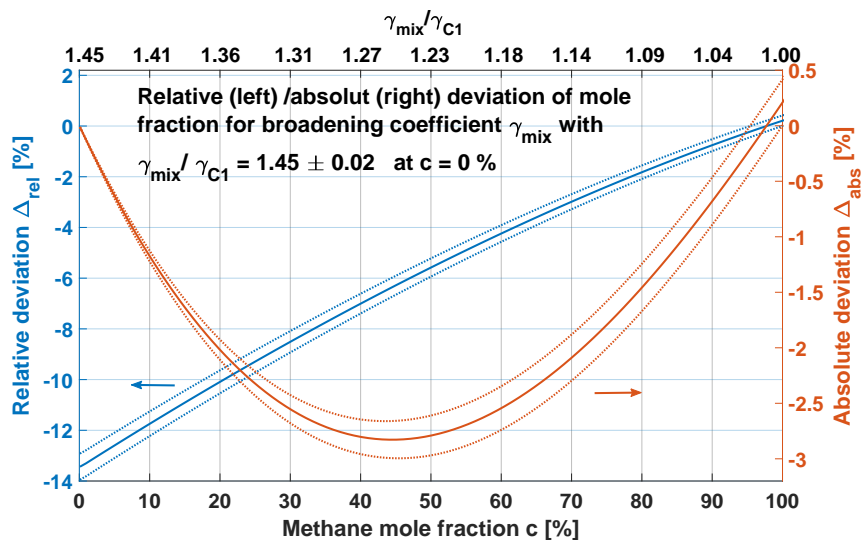
Figure 6.12: Estimation of relative and absolute deviation for fitting a simulated broadened methane spectrum with the self-broadened measured reference spectrum. The curves (solid lines) are given with the respective error bands (dotted lines). The value of the γ_{mix} coefficient and its uncertainty is the average of the other alkane broadening coefficients and their uncertainties, cf. Fig. 6.5.

measured pure methane spectrum and the simulated spectrum with the HITRAN line parameters, cf. Fig. 6.2 on database parameter accuracies.

These findings suggest that when the mole fractions of the other gases are known and therefore the broadening coefficient for methane can be calculated, that a correction curve could be estimated for the determination of the methane mole fraction. The result for the deviation of the first gas mixture supports this assumption. But the analysis neglects broadening of other gas species and therefore must reveal errors when the other gas species spectra are also broadened.

Figure 6.13 displays the results for gas mixtures with high methane and ethane concentrations in the range of 15-30 % each. For all components in the mixtures the gravimetric values (squares), the results for fitting the mixture spectrum with the pure reference spectra (cirlces) and the mole fractions for the fit with the simulated methane spectrum (diamonds) are depicted. The absolute deviations for methane are given for the pure fit Δ_{C1} and the fit with the simulated spectrum Δ_{sim}. The confidence intervals are small, (vertical bars) indicating that deviations are caused by systematic errors as spectral shape deviations.

First of all, the results approve the capability to determine mole fractions of the seven different alkanes in mixtures with low deviations. The absolute deviations for the methane mole fractions are larger compared to mixtures with small methane mole fraction. This confirms the general behavior of the estimation depicted in Figure 6.12. But also the ethane mole fractions show increased absolute deviations, which is depicted for higher clarity as
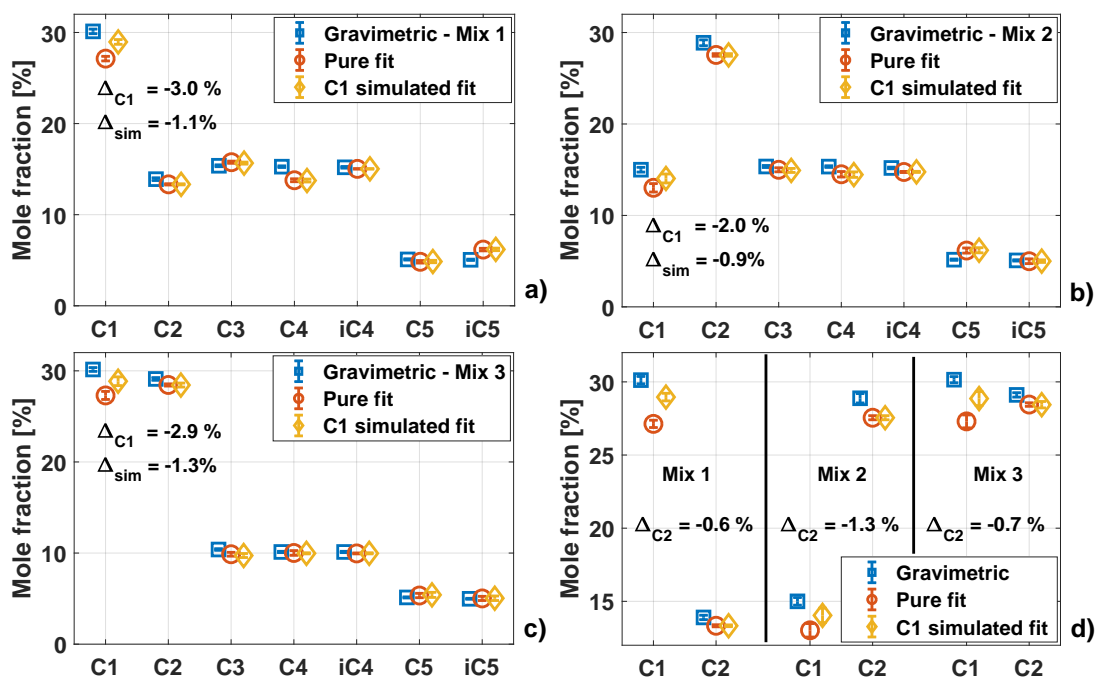
Figure 6.13: Results for the analysis of three gravimetric gas mixtures with high methane and ethane mole fractions, graphs a), b), c). Each gas is indicated by its carbons atom number C_x. The calibrated values are depicted as squares, the fitting values with the pure reference spectra as circles and the results with the simulated methane spectrum as diamonds. In graph d) the C1 and C2 results for the three mixtures are depicted to highlight the C2 deviations that are caused by broadening of the ethane spectrum.

close-up for the mixture results in graph d), and illustrates the broadening of ethane. The relative and absolute deviations are smaller than for methane and therefore confirm the qualitative results of the ethane broadening coefficients, cf. Fig. 6.9.

Regarding the other gas species of $C_3 - C_5$, the deviations are in general smaller, confirming less spectral shape broadening. In Mix 1 and Mix 2 the fitted butane mole fraction shows the highest difference from the calibrated value while one pentane value has an equivalent difference in the other direction, respectively. These results are analogous to the section-wise evaluation of the high propane mole fraction mixture before. Due to less spectral shape of the larger hydrocarbon spectra, the least square algorithm may lead to larger deviations for these gases. For all three mixtures the sum of the mole fractions is smaller than 100 %, which illustrates the expected systematic error due to the spectral shape broadening.

This can be further analyzed by the evaluation of the methane and ethane results. In Mix 1 the C1 deviation by fitting with the pure spectrum is -3 %. The estimated difference according to a correction curve, cf. Fig. 6.12, would be -2.55 ± 0.15 %. Thus the difference between calibrated and fitted value is already larger then the estimate. Fitting with the broadened spectrum decreases the non-conformance but less than suggested by the

estimate. The resulting mole fraction is still 1.1 % smaller than the calibrated value in the mixture. The same result pattern apply to Mix 2 and Mix 3. This shows, that despite the simulation of the methane spectrum, the deviations cannot be entirely corrected due to the broadening of the other gas species that is neglected in the evaluation.

Graph d) in Figure 6.13 illustrates the broadening for ethane. The deviation is smaller than for methane but systematic. Larger Lorentz widths of ethane lines in the mixture lead to smaller fit results of the mole fractions. The comparison of Mix 2 and Mix 3 emphasizes again the findings for the ethane broadening coefficients. The absolute deviation in Mix 2 is larger than in Mix 3 while the gravimetric mole fractions are the same ($\approx$ 29 %). But in Mix 3 the methane mole fraction has a higher percentage in the mixture. The broadening coefficient of methane as perturber is only slightly different from the self-broadening coefficient of ethane, cf. Fig. 6.9. Hence, a higher methane mole fraction reduces the ethane lines Lorentz widths and leads to a smaller deviation.

These results demonstrate that the broadening of the alkanes in mixtures behaves as expected. The estimate of the methane deviation showed good congruence to the fitted values in mixtures where the mole fractions of the higher hydrocarbons dominate. For these type of mixtures high accuracies for the seven components can be obtained, cf. Table 6.3. The limits of the method could be verified for mixtures with high mole fractions of the lighter hydrocarbons. The results confirm the previous analysis of broadening coefficients in binary mixtures. In order to achieve the same accuracies as for the first mixture analysis a more detailed evaluation of the broadening of the line spectra, especially for ethane, would be required. As the ethane lines are spread over the entire measured wavenumber range, it can be expected that a correction of the ethane spectra will affect all concentration values and potentially also correct deviations that remain for the other components.

A better quantitative knowledge of the broadening coefficients would lead to improved accuracies and also allow an incremental spectrum analysis. The evaluation method could be adapted that after a first fit of all mole fractions the broadening coefficient of methane and ethane are determined and the mixture fitted again with the simulated spectra. Repetition of the method should yield reduced deviations and therefore higher accuracies. The investigation of such a method is prospect of future research and requires measurements of further gas mixtures with varying mixing ratios. Finally, higher sensitivities of the measurements would also allow to determine potential variation of the higher hydrocarbons' spectral shape. Also the detection of trace levels would benefit from a higher sensitivity of the transmission signal. The accuracies of the mixture analysis with high propane mole fractions are suitable for field application but would require shorter measurements times. Potential approaches to realize a gas analyzer for process control operation will be highlighted in the Outlook Chapter 7.

6.4   Summary of spectral measurement results

The spectral measurements revealed the acquisition of high resolution and high accuracy pure gas spectra in the range of 1440-1480 cm^{-1}. Especially for the larger hydrocarbons ($C_3 - C_5$) spectra with much higher resolution than documented in the PNNL database and due to the reduced pressure with unprecedented details could be acquired.

The quality of the measurements allowed to determine average broadening coefficients for methane and ethane in binary mixtures by Voigt profile fitting to the transmission spectra. The results for methane are in good agreement with previous research. The ethane coefficients reveal larger uncertainties and display a qualitative behavior due to the pseudo line approach. Nonetheless, the ethane broadening coefficient allows to interpret the deviations due to line broadening in complex gas mixtures. No comparable studies of the broadening among alkanes in binary mixtures have been reported in this wavelength range before.

The high resolution reference spectra could be used for the quantitative analysis of seven component gas mixtures. For a gas mixture with propane as main component deviations from the calibrated values of < 0.5 vol.% could be obtained for all gases. In addition the broadening coefficients of methane could be used for a simplified approach to simulate the methane spectrum in the mixture based on HITRAN line parameters which effectively reduces deviations in the quantitative analysis. This was also confirmed for further gas mixtures.

The general behavior and estimated relative and absolute deviations for the quantitative evaluation of a broadened line spectrum in a gas mixture was deduced from the methane broadening coefficients. The expected broadening behavior could be verified for three gas mixtures with high portions of methane and ethane. Higher absolute deviations for the quantitative evaluation with self-broadened reference spectra are obtained. The results also reveal that the applicability of the simplified assumption that only the methane spectrum is broadened is dependent on the composition of the gas mixture. The correction of the deviation by simulation of the methane broadening is limited when large mole fractions of other gases with non-negligible broadening, as ethane, are present in the mixture. The deviations of ethane confirmed the behavior that was deduced from the determined qualitative ethane broadening coefficients.

This leads to the conclusion that resolved or partially resolved line spectra of smaller molecules in gas mixtures are more affected by collisional broadening. But as demonstrated, the broadening coefficients vary depending on the respective perturber species. The strongly overlapped and densly spaced line spectra of the larger HCs are less affected. Further research would have to be done to reveal potential impacts on their spectral shape.

Probably the energy surfaces of the larger molecules are less perturbed by other gas molecules. This would explain the negligible deviations of their spectral shapes. The development of a model that physically confirms this assumption would be prospect of further research. The transmission measurements that can be obtained from the developed measurement system or with a comparable system could then contribute to new findings in this field.

Chapter 7

Concluding remarks and outlook

In this chapter conclusive remarks will be given. First a summary will highlight the most relevant developments and results of the investigations in Section 7.1. A brief overview of prospects of improvements of the measurement system, cf. Section 7.2, is intended to indicate the most relevant aspects for realizing further advanced measurements and potentially develop multi-component gas analyzers for field applications. Finally, Section 7.3 outlines the scientific potential of the developed measurement system by its capabilities of acquiring high resolution spectra in the mid-infrared as the perspectives of further investigations in the field.

7.1 Summary

In the context of the work an unique laboratory system was developed and built up. It includes a gas sampling and mixing unit for the supply of the first seven alkanes to the optical measurements and the possibility to prepare arbitrary mixtures considering the real gas properties of the gases. The spectroscopic measurement system allows to measure gas transmission spectra in a wide spectral range form 6 to 11 μm and under broadly adjustable and highly precise pressure ($5-1000$ mbar) and temperature (ambient$-200°$ C) conditions.

In addition to the spectroscopic system a new laser operation procedure was developed to aim for the physical limits of the measurement system in order to obtain nearly gapless laser emission with a broadly tunable but mode-hopping EC-QCL system. A sophisticated signal post-processing was implemented for improving the spectral measurements by correcting and increasing the wavenumber accuracy of the measured spectra. The tuning accuracy of the MIRcat laser system of ≥ 0.5 cm^{-1}and the measurement accuracy of the wavelength meter of 200 MHz could be enhanced to ± 0.001 cm^{-1} or 30 MHz , respectively, in addition to achieving nearly gapless high spectral resolution of 0.001 cm^{-1} and broad spectral coverage. This allows to investigate the spectral shape of single absorption lines.

The spectral quality and sensitivity of the measurements could be verified and the limits of averaging demonstrated for the targeted spectral range by the Allan-Werle deviation analysis. The measurements revealed a minimum detectable absorption of 1.3×10^{-3} Hz$^{-1/2}$ which is equivalent to the per point noise level of the instrument for one second acquisition time in the spectral target range. Long time averaging analysis yielded a measurement stability of the system of 1-2 hours and an Allan-Werle deviation minimum value of the

spectral transmission of 1.94×10^{-4}.

The system enabled the acquisition of high quality reference spectra, that could be benchmarked against high quality database spectra in the case of methane. The residual between the measurements of methane and the simulation of the spectrum with database parameters showed peak intensity deviations of ≤ 2 % which is within the range of the uncertainties of the database values. Comparison of transmission line position and spectral shape revealed very high congruence of the measured spectra with the high quality database spectra. In the case of ethane missing lines in the database could be identified. The comparison of the measured to simulated ethane spectra revealed strong deviations of the line strengths and line widths of the tabulated values. This emphasized the necessity for acquiring high resolution and high accuracy reference spectra for the gas mixture analysis. The obtained spectra for the other alkanes (C_3-C_5) outperformed today available database spectra regarding accuracy and resolution. The advantage of the setup is the possibility to measure the transmission spectra at reduced pressure. The PNNL database tabulates cross-sections of the gases at ambient pressure with an resolution of 0.112 cm^{-1}. The reduced pressure broadening leads to less overlapped lines and therefore increased structure of the spectra that can be resolved and mainly contributes to the high accuracy of the quantitative spectra analysis. It should be emphasized that spectra of this high resolution and detail are not available in any public database.

In order to consider the collisional effects on the measured spectra in gas mixtures the systematic and detailed investigations of binary mixtures led to the determination of average broadening coefficients for the lighter hydrocarbons. Despite a simplified approach that determines average broadening coefficients, the obtained collisional line broadening coefficients for selected methane transitions compare well to previous investigations of the self-broadening of the lines and the line broadening in dry air or nitrogen. The broadening of the methane lines in other hydrocarbon gases has not been reported before and was investigated for the first time as part of this thesis.

Multi-component gas mixtures were measured and quantitatively analyzed with the measured reference spectra. The obtained mole fractions of the gas components reveal high accuracies. The work published the feasibility of a quantitative seven component alkane mixture analysis with tunable laser absorption spectroscopy for the first time. The remaining deviations of ≤ 0.5-mol/mol % could be either directly verified with the line broadening of the methane lines or ascribed to spectral shape deviations of the other alkanes, especially ethane, that was not corrected.

For methane a simplified method for correction of the broadening in multi-component mixtures was successfully tested. Concurrently, the limits of the method for gas mixtures with high proportions of light hydrocarbons were examined and therefore prospects for further improvements indicated. The current results show that for achieving higher quantitative accuracies the collisional broadening of the ethane lines must be considered in the evaluation of the spectra. An analysis of the behavior of all gases would therefore require further measurements and the consideration of spectral models. The objective of further improving sensitivity and accuracy of the system would potentially allow a more detailed analysis of the larger molecules $(C_3 - C_5)$.

The thesis illustrates and proves the potential of sensing multi-species gas mixtures by using broadly tunable laser sources in the mid-infrared that especially exhibit advantages for industrial applications compared to other spectroscopic technologies, cf. Chapter 1. It equally underlines the scientific challenges of understanding and achieving measurements of this high quality and resolution as well as the still remaining deficiencies of limited knowledge in the field like unknown spectral line parameters or collisional broadening behaviour of the ro-vibrational transitions of the selected set of alkanes. Desirable improvements on technical side concerning the measurement system and aspects of further research are outlined in the following.

7.2 Prospects for improvements of the measurement system

The main potentials for improvements of the measurement system are to increase the averaging sensitivities, to avoid spectral distortion and especially to reduce the long measurement times. The acquired spectra revealed high quality and either compare to state-of-the-art databases or could show so far not documented spectral details. Further improvement would allow to generate even more detailed spectra on shorter time scales and therefore allow to apply the measurements for the generation of new spectral models for various gas species or target new measurement applications regarding other gas mixtures or trace gas detection.

Spectral sensitivities of other spectroscopic techniques [87], especially in the near infrared [122], allow to focus on trace gas sensing and achieve much lower minimum detectable absorbances. An increased sensitivity in combination with the already achieved broad spectral coverage and high resolution of the setup would have several benefits for the investigation of spectral models as for the quantitative analysis of gas mixtures. Measurements in the mid-infrared mainly suffer from comparably large noise levels of the MCT detectors. Thus, in the developed setup either other detectors could be tested or the signal to noise ratio can be improved by changing the employed beam splitters and neutral density filter. In the current configuration the laser beam is attenuated to eliminate detector saturation, cf. Section 4.1.2. But the incident power levels were not tested for the linearity threshold of the detectors. Optimization of the measurement sensitivity would lead to improved reference spectra. Therefore, one could obtain higher accuracies for multi-species sensing of the targeted alkanes and further investigate spectral broadening behavior also for the larger hydrocarbons.

Spectral distortions in the current setup are mainly caused by back-reflections into the EC-QCL. An optical isolator can alleviate the effect but is generally limited to a small spectral range and would therefore remove the advantage of the broad range wavelength tunability of the system. Tests of an attenuator in the wavelength meter path, that is presumed to be the main source of back-reflections, should be executed. This would also require to employ different beam splitters in the setup to increase the proportion of the

laser power that is guided to the beam coupler of the wavelength meter.

However, despite its broad spectral coverage and its high spectral resolution, long measurement times are caused by the operation of the EC-QCLs. The slow temperature tuning of the MIRcat and the averaging of several spectra to obtain higher sensitivities lead to long measurement times in the range of hours or days (0.1 cm^{-1}/min for a single measurement). A faster measurement method would allow to acquire spectra on a short timescale which would lead to shorter measurements times and potentially also higher sensitivities. The faster acquisition of the spectra would have several benefits on the analysis as more information would be generated, e.g. by measuring the spectra over a wider range and therefore obtaining a better quantitative discrimination. Finally, a real-time capable laser technology would respond to the requirements of field deployable gas analyzer.

Alternative technologies for laser sources exist, where two approaches should be highlighted as promising options for gas analyzer applications. First, recent research revealed advances in the development of miniaturized EC-QCLs with micro-mechanically manufactured (MOEMS) diffraction gratings [123–125]. These devices enable fast scanning rates in the kHz range leading to fast spectra generation and averaging capabilities. Recent investigations also target to change parameters as laser current and EC length during the fast scans for obtaining a spectral resolution that is not limited by the EC mode spacing. The demonstration of a system for multi-species gas detection was not realized yet but can be expected as foreseeable application of the technology.

Second, DFB QCL arrays were already demonstrated more than a decade ago [126]. Up to 30 different DFB QCLs on a monolithic chip have been realized allowing for broad tunability and narrow bandwidth in the range of 100 cm^{-1}. Recent demonstrations for gas sensing applications of atmospheric concentration measurements of methane [127] and of carbon monoxide, carbon dioxide and acetylene [128] in a flame gas mixture have been reported. The combination of the beams to a single output remains challenging. Demonstrations with external diffraction grating are bulky and sensitive to shocks and vibrations [129]. Arrayed waveguide gratings (AWGs) [130] could be developed to achieve single facet output but the technology remains ambitious and suffers from attenuation of the laser power in the waveguide as back reflections that affect the emitted modes. A QCL array in the targeted wavelength range for the presented alkane sensing could not be realized, yet.

But employing DFB QCLs for quantitative gas analysis has general advantages as fast tunability, narrow linewidth and the applicability of wavelength modulation (WMS) techniques [131, 132]. These enable higher sensitivities due to high frequency sine modulation of the laser emission that allow for evaluation of the harmonics of the signal. Noise reduction and background removal lead to higher signal to noise ratios which are especially beneficial for trace gas detection.

Summarizing, multiple approaches exist that could improve the developed measurement system despite the high-quality results that were already achieved. The mentioned technologies are most likely to find a way into the field for multi-component gas analyzers. The results of the thesis also revealed potentials for further improvements with regard to

the evaluation of the gas spectra. The following and closing section should briefly highlight these prospects.

7.3 Outlook for further investigations

The spectral sensing of dense gas mixtures, thus gases in mixtures with high mole fractions of the respective components, implies the outlined difficulties of spectral broadening but is of great interest for various process gas applications. The developed measurement system and acquired spectra revealed an approach how to deal with this challenging measurement task.

Fast, narrow linewidth and broadly tunable laser sources would allow to gain much more measurement data and therefore improve ro-vibrational transition models of diverse molecules. But already with the existing setup investigations of the targeted hydrocarbons and of further molecules over a wide wavelength range and at various highly stable pressure and temperature conditions are feasible at a resolution that can compare to highest resolution FTIR systems [133].

In Figure 2.6 in the Fundamentals chapter an overview of multiple technically relevant gases was given. The depiction emphasizes that gas sensing is still mainly focused on trace gas detection, as the detection limits of a gas species are in most cases the figure of merit of a measurement system. Therefore, it should be underlined again that collisional effects and broadening coefficients, except for atmospheric conditions, have not been comprehensively investigated, yet, and remain a large field of research. The setup allows to investigate the spectra of various gases as of self-prepared gas mixtures. New reference spectra would complement spectral databases by identifying missing lines of already tabulated gases as shown for ethane, generate spectra with either higher resolution as demonstrated for the $C_3 - C_5$ alkanes or measure spectra at undocumented conditions of reduced pressure or elevated temperatures. This would allow to improve the databases and also to verify and refine spectral models of the molecules. The measurement of other gas mixtures can reveal broadening behavior which would be beneficial for spectral models and quantitative gas analysis.

Hence, the setup allows to gain knowledge for the spectroscopy of gas species in a broad range in the mid-infrared and for various highly stable pressure and temperature conditions. The availability of high quality reference spectra would be a valuable basis for many other fields as atmospheric research, planetary remote sensing, breath gas analysis, gas reaction chemistry, further industrial applications and fundamental laboratory spectroscopy [6].

Regarding the specific application of the investigated alkane mixture sensing, an evaluation of the optimum measurement conditions for achieving higher accuracies in the mixture evaluation would be of further interest. Thus, beside the improvement of the measurement system regarding measurement time, sensitivity and potentially also accuracy, investigations could focus on optimum pressure, temperature and path length of the transmissions measurements. Especially the pressure broadening strongly influences

the spectral shape.   The reduced pressure broadening and therefore less overlapped ro-vibrational lines improved the quantitative analysis of the gas mixtures. Concurrently, shape deviations, due to collisional broadening, affects the mixture analysis.   Further reduced pressures might lead to better sensing results. Generally, around 30 mbar the Doppler broadening starts to dominate the line profile while the peak absorption remains still strong. A reduced pressure would decrease the proportion of the Lorentzian component on the line profile which is affected by the collisional broadening. Reduced broadening effects should lead to improved quantitative discrimination of the gases. Even further reduced pressures would lead to low gas densities which would have to be compensated with much longer path lengths, making the setup either more bulky for single-path gas cells or potentially imply more delicate handling for multi-path cells.

   However, the mentioned aspects would all contribute to further improve the quantitative analysis of the measurements, gain further insights into the ro-vibrational transition behavior of the gases and potentially pave the way towards fast, robust and highly accurate process gas analyzers.

   This thesis proved a promising approach by measuring the gases at reduced pressure over a wide spectral range with a state-of-the-art laser source in the mid-infrared. The results revealed high accuracy gas mixture sensing capabilities and showed remaining challenges and starting points for further investigations. The unique setup and notable sensing results for single gases and multi-component gas mixtures are valuable contributions to the field and will hopefully encourage various further research and approaches.

Appendix A

Main properties of LabVIEW Graphical User Interfaces

The developed graphical user interfaces (GUIs) and their main functionalities have been introduced in Section 3.3. The in LabVIEW developed software serves for control and automation of the measurements as for the acquisition of spectral measurement data and monitored parameters in the setup as gas pressure and temperature. One GUI was developed to manipulate the gas supply and mixing and one for operating the optical measurement setup. A comprehensive description of all functions and the programming approach should not be given here, as it does not enrich the discussion of the measurement results. But their development took notable effort and was the precondition to realize automated longtime measurements that were especially necessary to acquire the multitude of high resolution and high accuracy reference spectra.

In order to give a brief impression of the GUIs and their visual appearance their main tasks will be listed in the following and some key elements highlighted in the respective figures.

Gas Setup Graphical User Interface

The LabVIEW "virtual instrument" was designed with the intention that the GUI resembles in its visual structure to the panel of the gas mixing unit, cf. sketch in Figure 3.2. It controls all elements of the gas setup including the mass flow controllers, pressure controller, pumps and valves. Also the acquisition of pressure and temperature data is implemented in the software. The automation allows measurements campaigns with different gases to be fed subsequently to the optical setup and the automated preparation of arbitrary gas mixtures. The key control elements are highlighted in Figure A.1.

A list of the main tasks that can be executed with the GUI is given in the following:

- Control individual mass flow controllers (MFCs) for gas supply.

- Control valves and pumps of the setup for gas flow direction, gas mixing and evacuation.

- Set values of pressure controller operation.
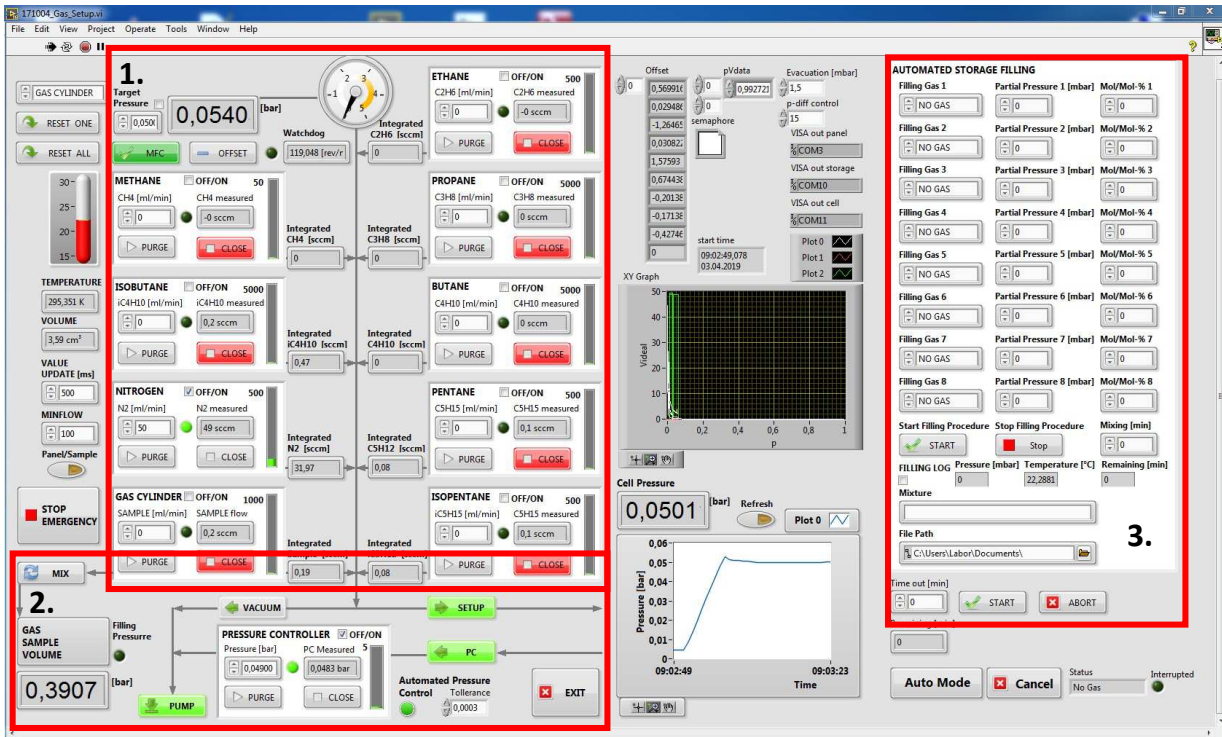
Figure A.1: Screenshot of in LabVIEW developed GUI for operation of the gas setup. The figure shows the GUI during setup operation. Three main parts of the control elements are marked in red rectangles and indicated with respective numbers:
1. Control the individual mass flow controllers to set flow and pressure of gases,
2. Control of valves and pumps to either set gas flow to optical setup or evacuate system and stabilize pressure in gas cell with settings of the pressure controller,
3. Setting of gases and partial pressures for an automated gas mixture preparation as described in Section 3.2.3.

- Select settings and start automated gas mixture preparation.

- Start automated measurement campaign that enables gas flow of different gas species and evacuation of the system according to the measurement protocol.

Optical Setup Graphical User Interface

The GUI of the optical setup includes much more functions and is more complex than the graphical user interface of the gas setup. Here only the first tab is displayed in Figure A.2 which mainly shows the laser settings and the acquired signals. In the underlying tabs settings for the sampling rates of the data acquisition, buffer sizes, file names, etc. and settings for the automated measurements and the protocol of measurement campaigns can be taken. The GUI serves for operating the EC-QCLs and the wavelength meter and

Figure A.2: Screenshot of in LabVIEW developed GUI for operation of the optical setup. The figure shows the GUI during a spectroscopic measurement. Four main parts of the control elements are marked in red rectangles and indicated with respective numbers:
1. Settings and selection of the individual laser as grid position, thus wavenumber, laser mode (cw or pulsed), QCL current, TEC temperature, etc.
2. Diagrams to display signals of the three detectors over time,
3. Diagrams to display MIRcat parameters over time as TEC-current, QCL-temperature and QCL-current,
4. Diagram that displays wavelength meter measurement over time.

recording all signals from the spectroscopic measurements.

A list of the main tasks that can be executed is given in the following:

- Display of recorded signals from the detectors, the laser operation parameters and the wavelength meter measurement.

- Setting and selecting modes of MIRcat operation.

- Setting file path and measurements file names.

- Acquiring and pre-processing of detector signals with Fast Fourier Transform, cf. Section 5.3.1.

- Setting parameters for automated spectral longtime measurements.

- Setting and starting measurement campaigns that include automated operation of the optical and the gas setup.

Appendix B

Remarks on the data fitting procedures

The acquired spectral data of the measurement setup was used in several ways to obtain results for different model parameters by nonlinear least squares fitting routines. The fitting routines were applied for the following three use cases:

- Airy function fit for determination of outliers in the processing of the detector signals, cf. Section 5.3.2,

- line widths and line strengths fits to determine the broadening coefficients of methane or the pseudo line parameters in the case of ethane, cf. Section 6.2.2, and

- the fitting of reference spectra to measured transmission spectra of gas mixtures to obtain the mole fraction of each component, cf. Section 6.3.2.

For each fitting procedure the spectral data had the same quality or noise level as determined in the sensitivity estimation in Section 5.5. In general the number of measurement values was much larger than the number of parameters in the respective model function, e.g. for 7 gas mole fractions analyzing a wavenumber range of 10 cm^{-1} included $n = 10000$ spectral measurement points.

The parameter fit was solved with standard routines that minimize a χ^2 cost function:

$$\chi^2(\boldsymbol{\beta}) = \sum_{i=1}^{n} \left[y_i - f(x_i, \boldsymbol{\beta}) \right]^2 \tag{B.1}$$

where y_i are the measured dependent values, f the respective model function with x_i the independent variable and $\boldsymbol{\beta}$ the model parameter vector that is varied to minimize the cost function. This is also called the residual $r_i = y_i - f(x_i, \boldsymbol{\beta})$ of the measured data and the model function dependent on the model parameter vector $\boldsymbol{\beta}$. A minimum of χ^2 requires gradient zero. Depending on the number of parameters multiple gradients have to be calculated:

$$\frac{\partial \chi^2}{\partial \beta_j} = 2 \sum_i r_i^2 \frac{\partial r_i}{\partial \beta_j} = 0 \ . \tag{B.2}$$

For a nonlinear model function the minimization is often realized by repeated approximation of the function with a linear model, e.g. by a Taylor series, cf. Eq. B.3, as the

derivatives $\frac{\partial r_i}{\partial \beta_j}$ are functions of both the independent variable and the parameter which generally does not allow a closed solution.

$$f(x_i, \boldsymbol{\beta}) \approx f(x_i, \boldsymbol{\beta}^k) + \sum_j J_{ij}(\beta_j - \beta_j^k). \tag{B.3}$$

In Equation B.3 $J_{ij} = \frac{\partial f(x_i, \boldsymbol{\beta}^k)}{\partial \beta_j}$ is the Jacobian of the model function which are the partial derivatives of the model function by the components j of model parameter vector $\boldsymbol{\beta}$ at each function value i and where k is an iteration number. It represents therefore all gradients of the model for a chosen set of parameters. In order to minimize the difference between measurements and the model function iterative procedures are applied as the Gaus-Newton method or Levenberg-Marquardt algorithm which can be consulted in the respective literature [134, 135]. The procedure always starts with a set of initial values for the parameters $\boldsymbol{\beta}^0$, e.g. the tabulated line parameters for the methane line fitting or a mole fraction between 0 and 1 for the quantitative gas mixture analysis. It varies the parameters step by step until a convergence criterion is met, thus a minimum was found, or the steps size falls below a set minimum.

These numerical solving routines may not succeed in finding the global minimum but identify a local minimum of the model function or can fail in finding a minimum by exceeding the number of preset iterations, thus simply not finding a minimum at all. In the processed data solutions could be found due to good congruence of the model functions and the fitted measurement data. Nonetheless, deviations can be high and fitting results strongly different from expected results as demonstrated for the quantitative mixture analysis, cf. Table 6.2. Especially, the quantitative analysis illustrated that broad spectral coverage and thus data with sufficient content of information is required to obtain good fit estimates.

Essential in any fitting routine is the goodness of the fit and the estimation of a confidence interval of the fit results. For the numerical solution of nonlinear least squares fitting the confidence of the estimates can be obtained by approximating the covariance matrix C of the parameters at the found minimum. For this calculation the Jacobian with the minimum model parameter vector $\boldsymbol{\beta}$ can be employed as given in Equation B.4:

$$C = \frac{(\boldsymbol{J}^T \boldsymbol{J})^{-1} \|\boldsymbol{r}\|^2}{n - m} \tag{B.4}$$

The diagonal elements of the matrix C contain the variances σ_j^2 of the fitting parameters. The numerator $n - m$ is the statistical degrees of freedom as difference of the number of measured values n minus the length of the model parameter vector m. In the results of the thesis a 95 % confidence interval was specified which corresponds to a $\pm 2\sigma$ deviation range. A clear quantitative interpretation of these values as measurement errors can be drawn when the errors of the measurement data are normally distributed. Due to the filter procedures of the measurement data, remaining unidentified outliers or systematic errors due to spectral broadening this assumption can be argued.

But the results show that either for the gas mole fraction evaluations confidence intervals are small due to the broad spectral range and therefore large number of measured values or deviations are bigger in cases when the simplified model cannot generate a complete estimation of the measured data as seen for the ethane pseudo line list evaluation. In both cases are larger deviations of the results dominantly due to deficiencies in the model function that are either incomplete, applied to too little measurement data or neglect physical effects as the collisional broadening in gas mixtures.

These considerations emphasize that high potential is given by improving spectral models to better evaluate the high quality measurement data. But also measuring of gas spectra over broader ranges simply supplies more information to the fitting procedure and improves the parameter estimates as demonstrated for the pentane mole fractions in the gas mixture analysis.

Appendix C

Selected lines for the ethane spectrum analysis

For the pseudo line list analysis of a small range of the ethane spectrum in Section 6.2.2.2 the strongest tabulated lines of the HITRAN database were selected. The approach assumes to simplify the fitting procedure by reducing the number of lines from 125 to the 28 strongest lines in the wavenumber range from 1462.8cm^{-1} to 1463.4cm^{-1}. All 125 tabulated lines in HITRAN can be looked up in the database at the HITRAN indices 3634604 to 3634728 for ethane.

In the following selected line parameters of the 28 strong lines are given, comprising line position, HITRAN index, line strength and the self-broadened Lorentzian line width at atmospheric pressure. These HITRAN values are compared to the fitted pseudo line parameters comprising the fitted line strengths and Lorentzian line widths at atmospheric pressure by fitting of the pure ethane spectrum at 50 mbar.

Table C.1: The table shows the HITRAN parameters of the selected 28 strongest lines of ethane in the range from 1462.8cm⁻¹ to 1463.4cm⁻¹ and the fitted Lorentzian line widths and line strengths. First the line position in wavenumbers and the HITRAN index are given. Then the third and fourth column comprise the tabulated Lorentzian width ν_L of the self-broadenend ethane lines and the line strengths S. The last two columns display the fitted Lorentzian widths ν_L-Fit and the fitted line strength S-Fit that were obtained when the measured transmission spectrum at 50 mbar was fitted with the selected 28 lines.

Line position [cm⁻¹]	Index	ν_L [cm⁻¹atm⁻¹]	S [cm²/mol]	ν_L-Fit [cm⁻¹atm⁻¹]	S-Fit [cm²/mol]
1462.857	3634613	0.113	$4.264 \cdot 10^{-23}$	2.363	$1.324 \cdot 10^{-21}$
1462.895	3634625	0.114	$4.542 \cdot 10^{-23}$	0.399	$1.31 \cdot 10^{-22}$
1462.907	3634632	0.117	$7.380 \cdot 10^{-23}$	$5.000 \cdot 10^{-5}$	$1.62 \cdot 10^{-24}$
1462.916	3634635	0.115	$1.652 \cdot 10^{-22}$	0.079	$1.30 \cdot 10^{-22}$
1462.929	3634642	0.116	$5.122 \cdot 10^{-23}$	1.703	$1.21 \cdot 10^{-24}$
1462.937	3634644	0.114	$4.960 \cdot 10^{-23}$	0.120	$1.29 \cdot 10^{-22}$
1462.944	3634646	0.115	$5.084 \cdot 10^{-23}$	0.059	$4.03 \cdot 10^{-23}$
1462.992	3634652	0.138	$3.403 \cdot 10^{-22}$	0.104	$2.83 \cdot 10^{-22}$
1462.995	3634653	0.123	$1.461 \cdot 10^{-22}$	1.280	$6.24 \cdot 10^{-22}$
1463.008	3634655	0.136	$5.844 \cdot 10^{-22}$	0.125	$8.49 \cdot 10^{-22}$
1463.024	3634657	0.130	$4.880 \cdot 10^{-22}$	0.119	$4.38 \cdot 10^{-22}$
1463.030	3634658	0.135	$7.914 \cdot 10^{-22}$	0.150	$1.15 \cdot 10^{-21}$
1463.056	3634662	0.133	$9.721 \cdot 10^{-22}$	0.123	$1.14 \cdot 10^{-21}$
1463.077	3634666	0.116	$1.429 \cdot 10^{-22}$	0.204	$5.01 \cdot 10^{-22}$
1463.087	3634670	0.132	$1.129 \cdot 10^{-21}$	0.108	$1.14 \cdot 10^{-21}$
1463.117	3634673	0.132	$2.831 \cdot 10^{-22}$	0.141	$4.05 \cdot 10^{-22}$
1463.123	3634676	0.130	$1.262 \cdot 10^{-21}$	0.114	$1.39 \cdot 10^{-21}$
1463.154	3634678	0.130	$3.166 \cdot 10^{-22}$	0.176	$6.70 \cdot 10^{-22}$
1463.164	3634683	0.129	$1.371 \cdot 10^{-21}$	0.109	$1.28 \cdot 10^{-21}$
1463.195	3634686	0.129	$3.441 \cdot 10^{-22}$	0.057	$1.57 \cdot 10^{-22}$
1463.209	3634691	0.128	$1.456 \cdot 10^{-21}$	0.166	$2.55 \cdot 10^{-21}$
1463.240	3634696	0.128	$3.655 \cdot 10^{-22}$	0.123	$4.49 \cdot 10^{-22}$
1463.257	3634700	0.126	$1.516 \cdot 10^{-21}$	0.118	$1.87 \cdot 10^{-21}$
1463.289	3634706	0.126	$3.808 \cdot 10^{-22}$	0.184	$7.14 \cdot 10^{-22}$
1463.309	3634708	0.125	$1.553 \cdot 10^{-21}$	0.110	$1.82 \cdot 10^{-21}$
1463.342	3634715	0.125	$3.903 \cdot 10^{-22}$	0.104	$4.17 \cdot 10^{-22}$
1463.365	3634720	0.124	$1.567 \cdot 10^{-21}$	0.120	$1.60 \cdot 10^{-21}$
1463.398	3634728	0.124	$3.942 \cdot 10^{-22}$	0.964	$3.55 \cdot 10^{-21}$

Bibliography

[1] Jane Hodgkinson and Ralph P Tatam. "Optical gas sensing: a review". In: *Measurement Science and Technology* 24.1 (2012), p. 012004.

[2] Peter Werle et al. "Near-and mid-infrared laser-optical sensors for gas analysis". In: *Optics and lasers in engineering* 37.2-3 (2002), pp. 101–114.

[3] Ulrike Willer et al. "Near-and mid-infrared laser monitoring of industrial processes, environment and security applications". In: *Optics and lasers in engineering* 44.7 (2006), pp. 699–710.

[4] GA Eiceman, HH Jr Hill, and J Gardea-Torresdey. "Gas chromatography." In: *Anal Chem.* 70.12 (1998), 321R–339R.

[5] Claudia Maria Simonescu. "Application of FTIR spectroscopy in environmental studies". In: *Advanced Aspects of Spectroscopy*. IntechOpen, 2012.

[6] Kevin C. Cossel et al. "Gas-phase broadband spectroscopy using active sources: progress, status, and applications". In: *J. Opt. Soc. Am. B* 34.1 (2017), pp. 104–129.

[7] Mark G Allen. "Diode laser absorption sensors for gas-dynamic and combustion flows". In: *Measurement Science and technology* 9.4 (1998), p. 545.

[8] Maximilian Lackner. "Tunable diode laser absorption spectroscopy (TDLAS) in the process industries–a review". In: *Reviews in Chemical Engineering* 23.2 (2007), pp. 65–147.

[9] P Werle. "Laser excess noise and interferometric effects in frequency-modulated diode-laser spectrometers". In: *Applied Physics B* 60.6 (1995), pp. 499–506.

[10] P Werle et al. "Spectroscopic gas analyzers based on indium-phosphide, antimonide and lead-salt diode-lasers". In: *Spectrochimica Acta Part A: Molecular and Biomolecular Spectroscopy* 58.11 (2002), pp. 2361–2372.

[11] Rui Q Yang. "Infrared laser based on intersubband transitions in quantum wells". In: *Superlattices and Microstructures* 17.1 (1995), pp. 77–83.

[12] I Vurgaftman et al. "Interband cascade lasers". In: *Journal of Physics D: Applied Physics* 48.12 (2015), p. 123001.

[13] Yu Yao, Anthony J Hoffman, and Claire F Gmachl. "Mid-infrared quantum cascade lasers". In: *Nature Photonics* 6.7 (2012), p. 432.

[14] Bo Meng and Qi Jie Wang. "Broadly tunable single-mode mid-infrared quantum cascade lasers". In: *Journal of Optics* 17.2 (2015), p. 023001.

[15] Manijeh Razeghi et al. "Recent progress of quantum cascade laser research from 3 to 12 μm at the Center for Quantum Devices". In: *Applied optics* 56.31 (2017), H30–H44.

[16] Jean-Michel Hartmann, Christian Boulet, and Daniel Robert, eds. *Collisional Effects on Molecular Spectra*. Amsterdam: Elsevier, 2008, pp. v –.

[17] Jia Chen. "Compact laser-spectroscopic gas sensors using vertical-cavity surface-emitting lasers". PhD thesis. Technische Universität München, 2011.

[18] Max Born and Robert Oppenheimer. "Zur quantentheorie der molekeln". In: *Annalen der physik* 389.20 (1927), pp. 457–484.

[19] Hermann Haken and Hans C Wolf. *Molekülphysik und Quantenchemie: Einführung in die experimentellen und theoretischen Grundlagen*. Springer-Verlag, 2013.

[20] Yehuda B Band. "Light and Matter". In: (2006).

[21] Darko Dubravica. "Verbesserung der spektroskopischen Parameter von Methan im mittleren Infrarotbereich für die atmosphärische Fernerkundung". PhD thesis. Karlsruher Institut für Technologie, 2017.

[22] L.S. Rothman et al. "The HITRAN2012 molecular spectroscopic database". In: *Journal of Quantitative Spectroscopy and Radiative Transfer* 130 (2013). HITRAN2012 special issue, pp. 4 –50.

[23] Ronald K Hanson, R Mitchell Spearrin, and Christopher S Goldenstein. *Spectroscopy and optical diagnostics for gases*. Springer, 2016.

[24] Wolfgang Demtröder. *Laserspektroskopie: Grundlagen und Techniken*. Springer-Verlag, 2007.

[25] Linda R Brown et al. "Methane line parameters in HITRAN". In: *Journal of Quantitative Spectroscopy and Radiative Transfer* 82.1-4 (2003), pp. 219–238.

[26] HO Di Rocco and A Cruzado. "The Voigt Profile as a Sum of a Gaussian and a Lorentzian Functions, when the Weight Coefficient Depends Only on the Widths Ratio." In: *Acta Physica Polonica, A*. 122.4 (2012).

[27] Milton Abramowitz, Irene A Stegun, and Robert H Romer. *Handbook of mathematical functions with formulas, graphs, and mathematical tables*. 1988.

[28] John J Olivero and RL Longbothum. "Empirical fits to the Voigt line width: A brief review". In: *Journal of Quantitative Spectroscopy and Radiative Transfer* 17.2 (1977), pp. 233–236.

[29] L.S. Rothman et al. "The HITRAN2012 molecular spectroscopic database". In: *Journal of Quantitative Spectroscopy and Radiative Transfer* 130 (2013). HITRAN2012 special issue, pp. 4 –50.

[30] L. J. Radziemski. *Laser spectroscpopy and its applications*. Ed. by B. J. Thompson. Optical Engineering, 1987.

[31] Christopher S Goldenstein et al. "Infrared laser-absorption sensing for combustion gases". In: *Progress in Energy and Combustion Science* 60 (2017), pp. 132–176.

[32] Andreas Hangauer. "Detection schemes, algorithms and device modeling for tunable diode laser absorption spectroscopy". PhD thesis. Technische Universität München, 2012.

[33] Robert F Curl et al. "Quantum cascade lasers in chemical physics". In: *Chemical Physics Letters* 487.1-3 (2010), pp. 1–18.

[34] Kevin Knabe et al. "Frequency characterization of a swept-and fixed-wavelength external-cavity quantum cascade laser by use of a frequency comb". In: *Optics express* 20.11 (2012), pp. 12432–12442.

[35] D Mazzotti et al. "Frequency-comb-based absolute frequency measurements in the mid-infrared with a difference-frequency spectrometer". In: *Optics letters* 30.9 (2005), pp. 997–999.

[36] RK Hanson, PA Kuntz, and CH Kruger. "High-resolution spectroscopy of combustion gases using a tunable IR diode laser". In: *Applied Optics* 16.8 (1977), pp. 2045–2048.

[37] Maurus Tacke. "New developments and applications of tunable IR lead salt lasers". In: *Infrared Physics & Technology* 36.1 (1995), pp. 447–463.

[38] RF Kazarinov and RA Suris. "Possibility of amplification of electromagnetic waves in a semiconductor with superlattice". In: *Sov. Phys. Semicond.* 5.4 (1971), pp. 707–709.

[39] R. Q. Yang. "Infrared laser based on intersubband transitions in quantum wells". In: *Superlattices and Microstructures* 17 (Jan. 1995), pp. 77–77.

[40] James A Gupta et al. "Low-threshold InAs-based interband cascade lasers with room-temperature emission at 6.3 um (Conference Presentation)". In: *Novel In-Plane Semiconductor Lasers XVIII*. Vol. 10939. International Society for Optics and Photonics. 2019, 109390Y.

[41] Lu Li et al. "MBE-grown long-wavelength interband cascade lasers on InAs substrates". In: *Journal of Crystal Growth* 425 (2015), pp. 369–372.

[42] Jerome Faist et al. "Quantum Cascade Laser". In: *Science* 264.5158 (1994), pp. 553–556.

[43] Miriam Serena Vitiello et al. "Quantum cascade lasers: 20 years of challenges". In: *Optics express* 23.4 (2015), pp. 5167–5182.

[44] Christian Mann. "Entwurf und Charakterisierung von Quantenkaskadenlasern". PhD thesis. Albert-Ludwigs-Univeristät Freiburg, 2004.

[45] Jérôme Faist. *Quantum cascade lasers*. OUP Oxford, 2013.

[46] Jerome Faist et al. "Distributed feedback quantum cascade lasers". In: *Applied Physics Letters* 70.20 (1997), pp. 2670–2672.

[47]   Claire Gmachl et al. "Complex-coupled quantum cascade distributed-feedback laser". In: *IEEE Photonics Technology Letters* 9.8 (1997), pp. 1090–1092.

[48]   Peter Fuchs et al. "Widely tunable quantum cascade lasers with coupled cavities for gas detection". In: *Applied Physics Letters* 97.18 (2010), p. 181111.

[49]   Christian Pflügl et al. "High-temperature performance of GaAs-based bound-to-continuum quantum-cascade lasers". In: *Applied physics letters* 83.23 (2003), pp. 4698–4700.

[50]   Andreas Hugi et al. "External cavity quantum cascade laser tunable from 7.6 to 11.4 μ m". In: *Applied Physics Letters* 95.6 (2009), p. 061103.

[51]   Andreas Hugi, Richard Maulini, and Jérôme Faist. "External cavity quantum cascade laser". In: *Semiconductor Science and Technology* 25.8 (2010), p. 083001.

[52]   N Bandyopadhyay et al. "Ultra-broadband quantum cascade laser, tunable over 760 cm- 1, with balanced gain". In: *Optics express* 23.16 (2015), pp. 21159–21164.

[53]   Andreas Wittmann et al. "High-performance bound-to-continuum quantum-cascade lasers for broad-gain applications". In: *IEEE Journal of quantum electronics* 44.1 (2008), pp. 36–40.

[54]   Yu Yao et al. "Broadband quantum cascade laser gain medium based on a "continuum-to-bound" active region design". In: *Applied Physics Letters* 96.21 (2010), p. 211106.

[55]   Wenjia Zhou et al. "Monolithically, widely tunable quantum cascade lasers based on a heterogeneous active region design". In: *Scientific reports* 6 (2016), p. 25213.

[56]   GP Luo et al. "Grating-tuned external-cavity quantum-cascade semiconductor lasers". In: *Applied Physics Letters* 78.19 (2001), pp. 2834–2836.

[57]   Guipeng Luo et al. "Broadly wavelength-tunable external cavity, mid-infrared quantum cascade lasers". In: *IEEE journal of quantum electronics* 38.5 (2002), pp. 486–494.

[58]   Gottipaty N Rao and Andreas Karpf. "External cavity tunable quantum cascade lasers and their applications to trace gas monitoring". In: *Applied optics* 50.4 (2011), A100–A115.

[59]   Jan Kischkat. "External Cavity Quantum Cascade Lasers". PhD thesis. Humboldt-Universität Berlin, 2015.

[60]   R Centeno et al. "High power, widely tunable, mode-hop free, continuous wave external cavity quantum cascade laser for multi-species trace gas detection". In: *Applied Physics Letters* 105.26 (2014), p. 261907.

[61]   Gerard Wysocki et al. "Widely tunable mode-hop free external cavity quantum cascade laser for high resolution spectroscopic applications". In: *Applied Physics B* 81.6 (2005), pp. 769–777.

[62]   G. Wysocki et al. "Widely tunable mode-hop free external cavity quantum cascade lasers for high resolution spectroscopy and chemical sensing". In: *Applied Physics B* 92.3 (2008), pp. 305–311.

[63]   Chuan Peng, Guipeng Luo, and Han Q Le. "Broadband, continuous, and fine-tune properties of external-cavity thermoelectric-stabilized mid-infrared quantum-cascade lasers". In: *Applied optics* 42.24 (2003), pp. 4877–4882.

[64]   Henri A Favre and Warren H Powell. *Nomenclature of organic chemistry: IUPAC recommendations and preferred names 2013*. Royal Society of Chemistry, 2013.

[65]   Carl L Yaws and William Braker. *Matheson gas data book*. Matheson Tri-Gas Parsippany, NJ, 2001.

[66]   MA Mason and B Eakin. "Compressibility factor of natural gases at 60/sup 0/F and one atmosphere". In: *Am. Chem. Soc., Div. Gas Fuel Chem., Prepr.;(United States)* 2 (1960).

[67]   Bruce E Poling, John M Prausnitz, John P O'connell, et al. *The properties of gases and liquids*. Vol. 5. Mcgraw-hill New York, 2001.

[68]   Kenneth E Starling and Jeffrey L Savidge. *Compressibility factors of natural gas and other related hydrocarbon gases*. AGA, American Gas Association, 1994.

[69]   Ding-Yu Peng and Donald B Robinson. "A new two-constant equation of state". In: *Industrial & Engineering Chemistry Fundamentals* 15.1 (1976), pp. 59–64.

[70]   Florian Dauber and Roland Span. "Achieving higher accuracies for process simulations by implementing the new reference equation for natural gases". In: *Computers & Chemical Engineering* 37 (2012), pp. 15–21.

[71]   Kamal IM Al-Malah. *Aspen plus: chemical engineering applications*. John Wiley & Sons, 2016.

[72]   Thomas E Daubert. "Physical and thermodynamic properties of pure chemicals: data compilation". In: *Design Institute for Physical Property Data (DIPPR)* (1989).

[73]   Bahaa EA Saleh and Malvin Carl Teich. *Grundlagen der Photonik*. John Wiley & Sons, 2008.

[74]   *MIRcat Tunable Mid-IR External Cavity Laser System*. D11-00028-01 Revision H. User Manual. Daylight Solutions, Inc. 2014.

[75]   F Cappelli et al. "Subkilohertz linewidth room-temperature mid-infrared quantum cascade laser using a molecular sub-Doppler reference". In: *Optics letters* 37.23 (2012), pp. 4811–4813.

[76]   Eugenio Fasci et al. "Narrow-linewidth quantum cascade laser at 8.6 μm". In: *Optics letters* 39.16 (2014), pp. 4946–4949.

[77]   Lionel Tombez et al. "Linewidth of a quantum-cascade laser assessed from its frequency noise spectrum and impact of the current driver". In: *Applied Physics B* 109.3 (2012), pp. 407–414.

[78]   DF Gray, KA Smith, and FB Dunning. "Simple compact Fizeau wavemeter". In: *Applied optics* 25.8 (1986), pp. 1339–1343.

[79]   Peter Buerki and Miles Weida. *CW Tuning Behavior of CW-PLS Lasers*. Tech. rep. Daylight Solutions, Inc., 2010.

[80]   Gary Douberly. *Application Note: Continuous tuning of a Daylight Solutions 6.05 μm cw EC-QCL without loss of coverage due to mode hops via sequential scans at different laser head temperatures*. Tech. rep. Department of Chemistry, University of Georgia, 2010.

[81]   Tracy Tsai and Gerard Wysocki. "Active wavelength control of an external cavity quantum cascade laser". In: *Applied Physics B* 109.3 (2012), pp. 415–421.

[82]   Alan V Oppenheim and Ronald W Schafer. *Discrete-time signal processing*. Pearson Education, 2014.

[83]   Lawrence Marple. "Computing the discrete-time" analytic" signal via FFT". In: *IEEE Transactions on signal processing* 47.9 (1999), pp. 2600–2603.

[84]   T Hasan. "Complex demodulation: Some theory and applications". In: *Handbook of Statistics* 3 (1983), pp. 125–156.

[85]   LR Brown et al. "Methane line parameters in the HITRAN2012 database". In: *Journal of Quantitative Spectroscopy and Radiative Transfer* 130 (2013), pp. 201–219.

[86]   Jens-Rainer Ohm and Hans Dieter Lüke. *Signalübertragung: Grundlagen der digitalen und analogen Nachrichtenübertragungssysteme*. Springer-verlag, 2015.

[87]   E.J. Moyer et al. "Design considerations in high-sensitivity off-axis integrated cavity output spectroscopy". In: *Applied Physics B* 92.3 (2008), p. 467.

[88]   PO Werle, R Mücke, and F Slemr. "The limits of signal averaging in atmospheric trace-gas monitoring by tunable diode-laser absorption spectroscopy (TDLAS)". In: *Applied Physics B: Lasers and Optics* 57.2 (1993), pp. 131–139.

[89]   David W Allan. "Statistics of atomic frequency standards". In: *Proceedings of the IEEE* 54.2 (1966), pp. 221–230.

[90]   Timothy J Johnson, Robert L Sams, and Steven W Sharpe. "The PNNL quantitative infrared database for gas-phase sensing: a spectral library for environmental, hazmat, and public safety standoff detection". In: *Chemical and Biological Point Sensors for Homeland Defense*. Vol. 5269. International Society for Optics and Photonics. 2004, pp. 159–168.

[91]   P. Hausmann, R. Sussmann, and D. Smale. "Contribution of oil and natural gas production to renewed increase in atmospheric methane (2007–2014): top–down estimate from ethane and methane column observations". In: *Atmospheric Chemistry and Physics* 16.5 (2016), pp. 3227–3244.

[92]   Giovanna Tinetti et al. "Probing the terminator region atmosphere of the hot-Jupiter XO-1b with transmission spectroscopy". In: *The Astrophysical Journal Letters* 712.2 (2010), p. L139.

[93] RH Dicke. "The effect of collisions upon the Doppler width of spectral lines". In: *Physical Review* 89.2 (1953), p. 472.

[94] NH Ngo et al. "An isolated line-shape model to go beyond the Voigt profile in spectroscopic databases and radiative transfer codes". In: *Journal of Quantitative Spectroscopy and Radiative Transfer* 129 (2013), pp. 89–100.

[95] NH Ngo et al. "Spectral shapes of rovibrational lines of CO broadened by He, Ar, Kr and SF6: A test case of the Hartmann-Tran profile". In: *Journal of Quantitative Spectroscopy and Radiative Transfer* 203 (2017), pp. 325–333.

[96] Nicole Jacquinet-Husson et al. "The 2009 edition of the GEISA spectroscopic database". In: *Journal of Quantitative Spectroscopy and Radiative Transfer* 112.15 (2011), pp. 2395–2445.

[97] LS Rothman et al. "HITEMP, the high-temperature molecular spectroscopic database". In: *Journal of Quantitative Spectroscopy and Radiative Transfer* 111.15 (2010), pp. 2139–2150.

[98] Carlo Di Lauro et al. "High resolution investigation of the 7 μm region of the ethane spectrum". In: *Planetary and space science* 60.1 (2012), pp. 93–101.

[99] Andreas Hangauer. "List lines". Private communication.

[100] Andreas Hangauer et al. "High frequency modulation capabilities and quasi single-sideband emission from a quantum cascade laser". In: *Optics express* 22.19 (2014), pp. 23439–23455.

[101] V Zeninari et al. "Measurements of air and noble-gas broadening and shift coefficients of the methane R3 triplet of the $2\nu3$ band". In: *Applied Physics B: Lasers and Optics* 72.8 (2001), pp. 953–959.

[102] Gaëlle Dufour et al. "Line profile study from diode laser spectroscopy in the 12 CH 4 2ν 3 band perturbed by N 2, O 2, Ar, and He". In: *Journal of Molecular Spectroscopy* 221.1 (2003), pp. 80–92.

[103] VA Kapitanov et al. "Collisional parameters of N 2 broadened methane lines in the R9 multiplet of the 2ν 3 band. Multispectrum fittings of the overlapping spectral lines". In: *Journal of Quantitative Spectroscopy and Radiative Transfer* 113.16 (2012), pp. 1985–1992.

[104] MAH Smith et al. "Air-and self-broadened half widths, pressure-induced shifts, and line mixing in the $\nu2$ band of 12CH4". In: *Journal of Quantitative Spectroscopy and Radiative Transfer* 133 (2014), pp. 217–234.

[105] Zhenhui Du et al. "Mid-Infrared Tunable Laser-Based Broadband Fingerprint Absorption Spectroscopy for Trace Gas Sensing: A Review". In: *Applied Sciences* 9.2 (2019), p. 338.

[106] Mark C Phillips et al. "Real-time trace gas sensing of fluorocarbons using a swept-wavelength external cavity quantum cascade laser". In: *Analyst* 139.9 (2014), pp. 2047–2056.

[107] BE Brumfield and MC Phillips. "Quantitative isotopic measurements of gas-phase alcohol mixtures using a broadly tunable swept external cavity quantum cascade laser". In: *Analyst* 142.13 (2017), pp. 2354–2362.

[108] P Morten Hundt et al. "Multi-species trace gas sensing with dual-wavelength QCLs". In: *Applied Physics B* 124.6 (2018), p. 108.

[109] Filippos Kapsalidis et al. "Dual-wavelength DFB quantum cascade lasers: sources for multi-species trace gas spectroscopy". In: *Applied Physics B* 124.6 (2018), p. 107.

[110] Lukas Emmenegger et al. "Multi-species trace-gas spectroscopy using dual-wavelength QCLs". In: (2019).

[111] Jana Jágerská et al. "Highly sensitive and fast detection of propane–butane using a 3 μm quantum cascade laser". In: *Applied optics* 52.19 (2013), pp. 4613–4619.

[112] Julien M Rey et al. "Broadly tunable mid-infrared VECSEL for multiple components hydrocarbon gas sensing". In: *Applied Physics B* 117.3 (2014), pp. 935–939.

[113] JH Northern et al. "Mid-infrared multi-mode absorption spectroscopy using interband cascade lasers for multi-species sensing". In: *Optics letters* 40.17 (2015), pp. 4186–4189.

[114] S O'Hagan et al. "Multi-species sensing using multi-mode absorption spectroscopy with mid-infrared interband cascade lasers". In: *Applied Physics B* 122.6 (2016), pp. 1–11.

[115] Angelo Sampaolo et al. "Interband cascade laser based quartz-enhanced photoacoustic sensor for multiple hydrocarbons detection". In: *Quantum Sensing and Nano Electronics and Photonics XV*. Vol. 10540. International Society for Optics and Photonics. 2018, p. 105400C.

[116] Angelo Sampaolo et al. "Methane, ethane and propane detection using a compact quartz enhanced photoacoustic sensor and a single interband cascade laser". In: *Sensors and Actuators B: Chemical* 282 (2019), pp. 952–960.

[117] Adam E Klingbeil, Jay B Jeffries, and Ronald K Hanson. "Temperature-and composition-dependent mid-infrared absorption spectrum of gas-phase gasoline: Model and measurements". In: *Fuel* 87.17-18 (2008), pp. 3600–3609.

[118] Xiaojun Tang et al. "On-line multi-component alkane mixture quantitative analysis using Fourier transform infrared spectrometer". In: *Chemometrics and Intelligent Laboratory Systems* 146 (2015), pp. 371–377.

[119] Dwain E Diller and Ren Fang Chang. "Composition of mixtures of natural gas components determined by Raman spectrometry". In: *Applied Spectroscopy* 34.4 (1980), pp. 411–414.

[120] Xi Han et al. "On-line multi-component analysis of gases for mud logging industry using data driven Raman spectroscopy". In: *Fuel* 207 (2017), pp. 146–153.

[121] Robert Heinrich et al. "High resolution quantitative multi-species hydrocarbon gas sensing with a cw external cavity quantum cascade laser based spectrometer in the 6–11 μ m range". In: *Journal of Applied Physics* 125.13 (2019), p. 134501.

[122] Jinbao Xia et al. "A ppb level sensitive sensor for atmospheric methane detection". In: *Infrared Physics & Technology* 86 (2017), pp. 194–201.

[123] Jan Grahmann et al. "Tunable External Cavity Quantum Cascade Lasers (EC-QCL): an application field for MOEMS based scanning gratings". In: *MOEMS and Miniaturized Systems XIII*. Vol. 8977. International Society for Optics and Photonics. 2014, p. 897708.

[124] Ralf Ostendorf et al. "Real-time spectroscopic sensing using a widely tunable external cavity-QCL with MOEMS diffraction grating". In: *Quantum Sensing and Nano Electronics and Photonics XIII*. Vol. 9755. International Society for Optics and Photonics. 2016, p. 975507.

[125] Ralf Ostendorf et al. "Recent advances and applications of external cavity-QCLs towards hyperspectral imaging for standoff detection and real-time spectroscopic sensing of chemicals". In: *Photonics*. Vol. 3. 2. Multidisciplinary Digital Publishing Institute. 2016, p. 28.

[126] Benjamin G Lee et al. "Widely tunable single-mode quantum cascade laser source for mid-infrared spectroscopy". In: *Applied Physics Letters* 91.23 (2007), p. 231101.

[127] Anna PM Michel et al. "Open-path spectroscopic methane detection using a broadband monolithic distributed feedback-quantum cascade laser array". In: *Applied Optics* 56.11 (2017), E23–E29.

[128] Laurent Bizet et al. "Multi-gas sensing with quantum cascade laser array in the mid-infrared region". In: *Applied Physics B* 123.5 (2017), p. 145.

[129] Benjamin G Lee et al. "Beam combining of quantum cascade laser arrays". In: *Optics Express* 17.18 (2009), pp. 16216–16224.

[130] Aditya Malik et al. "Germanium-on-silicon mid-infrared arrayed waveguide grating multiplexers". In: *IEEE Photonics Technology Letters* 25.18 (2013), pp. 1805–1808.

[131] Gary C Bjorklund. "Frequency-modulation spectroscopy: a new method for measuring weak absorptions and dispersions". In: *Optics letters* 5.1 (1980), pp. 15–17.

[132] Joel A Silver. "Frequency-modulation spectroscopy for trace species detection: theory and comparison among experimental methods". In: *Applied optics* 31.6 (1992), pp. 707–717.

[133] Johannes MG Niederer. *The infrared spectrum of methane*. ETH Zurich, 2012.

[134] Saul A Teukolsky et al. "Numerical recipes in C". In: *SMR* 693.1 (1992), pp. 59–70.

[135] Philip R Bevington et al. *Data reduction and error analysis for the physical sciences*. Vol. 7. 4. AIP, 1993, pp. 415–416.

List of Publications

Journal publications

- R. Heinrich, A. Popescu, R. Strzoda, A. Hangauer, and S. Höfling, "High resolution quantitative multi-species hydrocarbon gas sensing with a cw external cavity quantum cascade laser based spectrometer in the $6-11$ μm range". In: *Journal of Applied Physics*, 125, p. 134501, 2019, DOI: 10.1063/1.5082168

- R. Heinrich, A. Popescu, R. Strzoda, A. Hangauer, and S. Höfling, "High performance direct absorption spectroscopy of pure and binary hydrocarbon gases in the $6-11$ μm range". In: *Applied Physics B: Lasers and Optics*, 123, p. 223, 2017, DOI: 10.1007/s00340-017-6796-6

Conference publications

- R. Heinrich, A. Popescu, R. Strzoda, A. Hangauer, and S. Höfling, "High resolution quantitative multi-species hydrocarbon gas sensing with a cw EC-QCL". In: *Field Laser Applications in Industry and Research (FLAIR)*, Book of Abstracts, p. 58, Assisi, Italy, 2018

- R. Heinrich, A. Popescu, R. Strzoda, A. Hangauer, and S. Höfling, "High Perfomance Spectroscopy of Hydrocarbon Gas Mixtures in the $6-11$ μm Range". In: *internatiol workshop on opportunities and challenges in mid-infrared laser-based gas sensing (mirsens)*, Book of abstracts, p. 55, Wroclav, Poland, 2017,

- R. Heinrich, A. Popescu, R. Strzoda, A. Hangauer, and S. Höfling, "Experimental setup for wide range tunable laser spectrometers measuring complex hydrocarbon gas mixtures ". In: *Field Laser Applications in Industry and Research (FLAIR)*, Book of Abstracts, p. 88, Aix-les-Bains, France, 2016